108

C.E. SACLAY
DSM

# SERVICE TECHNIQUE DE CRYOGÉNIE ET DE MAGNÉTISME

DAPNIA-STCM-98-07

FERMILAB
SEP 29 1998
LIBRARY

Fermilab Library
0 1160 0067669 4

DAPNIA/STCM 98-07 August 1998

## REVIEW OF SUPERCONDUCTING DIPOLE AND QUADRUPOLE MAGNETS FOR PARTICLE ACCELERATORS

**Arnaud Devred**

DAPNIA

*Prepared for the Wiley Encyclopedia of Electrical and Electronic Engineering.*
*Revised for the Proceedings of the CERN Accelerator School on*
*Measurement and Alignment of Accelerator and Detector Magnets.*

Couverture : Sylvie Cabrit et Marc Sauvage

Le DAPNIA (**D**épartement d'**A**strophysique, de physique des **P**articules, de physique **N**ucléaire et de l'**I**nstrumentation **A**ssociée) regroupe les activités du Service d'Astrophysique (SAp), du Département de Physique des Particules Elémentaires (DPhPE) et du Département de Physique Nucléaire (DPhN).

Adresse : DAPNIA, Bâtiment 141
CEA Saclay
F - 91191 Gif-sur-Yvette Cedex

# REVIEW OF SUPERCONDUCTING DIPOLE AND QUADRUPOLE MAGNETS FOR PARTICLE ACCELERATORS

Arnaud Devred

Service des Techniques de Cryogénie et de Magnétisme
Commissariat à l'Energie Atomique/Saclay
F–91191 GIF-SUR-YVETTE CEDEX
FRANCE

*(Prepared for the Wiley Encyclopedia of Electrical and Electronics Engineering, J.G. Webster, ed.; revised for the Proceedings of the CERN Accelerator School on Measurement and Alignment of Accelerator and Detector Magnets; revised for internal publication at CEA/Saclay)*

## ABSTRACT

The quest for elementary particles has promoted the development of particle accelerators producing beams of increasingly higher energies. In a synchrotron, the particle energy is directly proportional to the product of the machine's radius times the bending magnets' field strength. Present proton experiments at the TeV scale require facilities with circumferences ranging from a few to tens of kilometers and relying on a large number (several hundred to several thousand) high field dipole magnets and high field gradient quadrupole magnets. These electro-magnets use high-current-density, low-critical-temperature superconducting cables and are cooled down at liquid helium temperature. They are among the most costly and the most challenging components of the machine.

After explaining what are the various types of accelerator magnets and why they are needed (section 1), we briefly review the parameters of existing superconducting particle accelerators (section 2). Then, we review the superconducting materials that are available at industrial scale (chiefly, NbTi and $Nb_3Sn$) and we describe the manufacturing of NbTi wires and cables (section 3). We also present the difficulties of processing and insulating $Nb_3Sn$

conductors, which so far have limited the use of this material in spite of its superior performances. We continue by discussing the two-dimensional current distributions which are the most appropriate for generating pure dipole and quadrupole fields and we explain how these ideal distributions can be approximated by so-called $\cos\theta$ and $\cos 2\theta$ coils (section 4). We also describe the difficulties of realizing coil ends. Some of the toughest requirements on the performance of accelerator magnets are related to field quality, and we summarize the different sources of field errors (section 5). Next, we present the mechanical design concepts that are used in existing accelerator magnets (section 6) and we explain the various cooling schemes which have been implemented (section 7). Finally, we discuss the issues related to quench performance (section 8) and quench protection (section 9).

## CONTENTS


**1 TYPES OF ACCELERATOR MAGNETS** 1
1.1 ACCELERATOR SYSTEMS 1
1.2 MAIN RING DESIGN 1
1.3 BENDING AND FOCUSING MAGNETS 2
1.3.1 COORDINATE SYSTEM DEFINITIONS 2
1.3.2 NORMAL DIPOLE MAGNET 3
1.3.3 NORMAL QUADRUPOLE MAGNET 3
**2 PARTICLE ACCELERATOR AND SUPERCONDUCTIVITY** 5
2.1 WHY SUPERCONDUCTIVITY? 5
2.2 REVIEW OF SUPERCONDUCTING PARTICLE ACCELERATORS 6
2.2.1 TEVATRON 6
2.2.2 HERA 6
2.2.3 UNK 6
2.2.4 SSC 6
2.2.5 RHIC 7
2.2.6 LHC 7
2.3 PROMINENT FEATURES OF SUPERCONDUCTING ACCELERATOR MAGNETS 7
2.4 SUPERCONDUCTING ACCELERATOR MAGNET R&D 8
**3 CONDUCTOR AND CONDUCTOR INSULATION** 9
3.1 PRACTICAL SUPERCONDUCTORS 9
3.1.1 SUPERCONDUCTING MATERIALS 9
3.1.2 SUPERCONDUCTING MULTIFILAMENTARY COMPOSITES 10
3.1.3 TRANSITION OF MULTIFILAMENTARY WIRES 11
3.2 NBTI WIRES 13
3.2.1 PROCESSING 13
3.2.1 DESIGN AND MANUFACTURING ISSUES 14
3.2.3 CRITICAL SURFACE PARAMETRIZATION 15
3.3 $NB_3SN$ WIRES 16
3.3.1 PROCESSING 16
3.3.2 CRITICAL SURFACE PARAMETRIZATION 16
3.4 RUTHERFORD-TYPE CABLES 17
3.5 CABLE INSULATION 19
3.5.1 INSULATION REQUIREMENTS 19
3.5.2 INSULATION OF NBTI CABLES 19

3.5.3 INSULATION OF $Nb_3Sn$ CABLES 20
**4 MAGNETIC DESIGN** 21
4.1 FIELD PRODUCED BY SIMPLE CURRENT LINE DISTRIBUTIONS 21
4.1.1 SINGLE CURRENT LINE IN FREE SPACE 21
4.1.2 SINGLE CURRENT LINE WITHIN A CIRCULAR IRON YOKE 21
4.1.3 QUADRUPLET OF CURRENT LINES WITH DIPOLE SYMMETRY 22
4.1.4 OCTUPLET OF CURRENT LINES WITH QUADRUPOLE SYMMETRY 22
4.1.5 $\cos p\theta$ AND $\sin p\theta$ CURRENT SHEETS 23
4.1.6 CYLINDRICAL CURRENT SHELLS 23
4.1.7 CYLINDRICAL CURRENT SHELLS WITHIN A CIRCULAR IRON YOKE 24
4.1.8 CYLINDRICAL CURRENT SHELLS WITH ANGULAR WEDGES 25
4.2 TWO-DIMENSIONAL GEOMETRY 27
4.2.1 SYMMETRY CONSIDERATIONS 27
4.2.2 CURRENT SHELL APPROXIMATIONS 27
4.2.3 IRON YOKE CONTRIBUTION 27
4.2.4 OPERATING MARGIN 28
4.2.5 CONDUCTOR GRADING 29
4.2.6 LIMITS OF $\cos\theta$ COIL DESIGN 30
4.3 COIL END DESIGN 30
4.4 SAGITTA 31
**5 FIELD QUALITY** 32
5.1 MULTIPOLE EXPANSION 32
5.2 FIELD QUALITY REQUIREMENTS 32
5.3 GEOMETRIC ERRORS 33
5.3.1 TYPES OF GEOMETRIC ERRORS 33
5.3.2 EFFECTS OF AZIMUTHAL COIL SIZE MISMATCH 33
5.4 IRON SATURATION 34
5.5 SUPERCONDUCTOR MAGNETIZATION 34
5.5.1 CRITICAL STATE MODEL 34
5.5.2 EFFECTS OF SUPERCONDUCTOR MAGNETIZATION 35
5.5.3 TIME DECAY 35
5.6 COUPLING CURRENTS 36
5.7 LONGITUDINAL PERIODICITY 37
**6 MECHANICAL DESIGN** 38
6.1 SUPPORT AGAINST THE LORENTZ FORCE 38
6.1.1 COMPONENTS OF THE LORENTZ FORCE 38
6.1.2 STABILITY AGAINST MECHANICAL DISTURBANCES 38
6.1.3 CONCEPTUAL DESIGN 38

6.2 AZIMUTHAL PRE-COMPRESSION 39
6.2.1 PREVENTING COLLAR POLE UNLOADING 39
6.2.2 PRE-COMPRESSION REQUIREMENT 39
6.2.3 CHOICE OF COLLAR MATERIAL 40
6.3 RADIAL SUPPORT 40
6.3.1 LIMITING RADIAL DEFLECTIONS 40
6.3.2 SEEKING YOKE SUPPORT 41
6.3.3 MECHANICAL DESIGN WITH FULLY MATED YOKE ASSEMBLY 41
6.3.4 MECHANICAL DESIGN WITH YOKE MIDPLANE GAP AT ROOM TEMPERATURE 42
6.3.5 RHIC MAGNETS 43
6.4 END SUPPORT 43
**7 MAGNET COOLING** 44
7.1 SUPERCONDUCTOR CRITICAL TEMPERATURE 44
7.2 MAGNET CRITICAL TEMPERATURE AT A GIVEN CURRENT 44
7.3 TEMPERATURE MARGIN AND ENTHALPY MARGIN 45
7.4 BOILING AND SUPERCRITICAL HELIUM COOLING 46
7.5 SUPERFLUID HELIUM COOLING 47
7.6 MAGNET CRYOSTAT 47
**8 QUENCH PERFORMANCE** 48
8.1 WHAT IS A QUENCH? 48
8.2 MAGNET TRAINING AND QUENCH PLATEAU 48
8.3 ACCURACY OF SHORT SAMPLE CURRENT LIMIT ESTIMATIONS 49
8.4 QUENCH ORIGINS 50
8.5 DISCRIMINATING BETWEEN CONDUCTOR-LIMITED AND MECHANICALLY-INDUCED QUENCHES 51
8.6 MECHANICAL TRAINING 51
8.7 QUENCH PERFORMANCE AS A FUNCTION OF RAMP RATE 52
8.8 SPECIFICATION ON QUENCH PERFORMANCE 53
**9 QUENCH PROTECTION** 55
9.1 THE EFFECTS OF A QUENCH 55
9.1.1 CONDUCTOR HEATING 55
9.1.2 MAXIMUM TEMPERATURE REQUIREMENT 55
9.1.3 PROTECTING A QUENCHING MAGNET 56
9.2 HOT SPOT TEMPERATURE 56
9.2.1 ESTIMATING HOT SPOT TEMPERATURE 56
9.2.2 LIMITING HOT SPOT TEMPERATURE 57
9.3 QUENCH DETECTION 57

9.4 PROTECTION OF A SINGLE MAGNET 58
9.4.1 CURRENT DISCHARGE 58
9.4.2 MAXIMUM VOLTAGE TO GROUND 58
9.4.3 QUENCH PROTECTION HEATERS 59
9.5 PROTECTION OF A MAGNET STRING 59
**10 BRIEF SUMMARY** 61
**ACKNOWLEDGMENTS** 61
**BIBLIOGRAPHY** 62
**TABLES** 77
**FIGURES** 81

# 1 TYPES OF ACCELERATOR MAGNETS

## 1.1 ACCELERATOR SYSTEMS

One of the main activities in nuclear and high energy physics is the study of the internal structures of charged particles. The research is carried out by smashing particles into pieces and by analyzing the nature and characteristics of the pieces. The particles are broken by accelerating them to high momenta and either by blasting them against a fixed target or by colliding them among themselves. To increase the event rate, the particles are bunched into a high intensity beam. The more elementary the particles, the higher the energy needed to smash them. Experiments at the proton scale require beam energies of the order of 1 TeV or more.

The beams of charged particles are produced by accelerator systems made up of several stages which progressively raise the energy. In the largest machines, the last stage of the accelerator chain, usually referred to as *main ring*, can have a circumference of several tens of kilometers and is installed in an underground tunnel. Such a ring is operated in three phases: (1) *injection*, during which the beam, which has been prepared in various pre-accelerators, is injected at low energy, (2) *acceleration*, during which the beam is accelerated to nominal energy and (3) *storage*, during which the beam is circulated at nominal energy for as long as possible (typically: up to 24 hours) and is made available for physics experiments. As mentioned above, there are two types of experiments: (1) *fixed-target* experiments, for which the beam is extracted from the main ring to be blasted against a fixed target, and (2) *colliding-beam* experiments, for which two counter-rotating beams are blasted at each other. The breakage products are analyzed in large detector arrays surrounding the targets or collision points.

## 1.2 MAIN RING DESIGN

A main ring of a large accelerator system is designed as a synchrotron-type accelerator [1]. In a synchrotron, the beam is circulated on an ideally circular orbit which remains the same throughout injection, acceleration and storage.

The charged particles are accelerated by means of electrical fields. The force, $\vec{F}_C$, exerted by an electrical field, $\vec{E}$, on a charge, $q$, is given by Coulomb's law

$$\vec{F}_C = q\,\vec{E} \tag{1}$$

Such a force provides an acceleration parallel to $\vec{E}$.

The particle beam is guided and focused by means of magnetic fields. The force, $\vec{F}_L$, exerted by a magnetic flux density, $\vec{B}$, on a charge, $q$, traveling at a velocity, $\vec{v}$, is given by Lorentz' law

$$\vec{F}_L = q\,\vec{v} \times \vec{B} \tag{2}$$

Such a force is perpendicular to the direction of $\vec{v}$ and $\vec{B}$ and its only action is to bend the particle trajectory. If $\vec{v}$ and $\vec{B}$ are perpendicular, the particle is deviated on an arc of a circle tangent to $\vec{v}$ and of radius, $\chi$, which can be estimated as

$$\chi \approx \frac{E}{0.3\,q\,B} \tag{3}$$

Here, $\chi$ is in meters, $B$ is the amplitude of $\vec{B}$ in teslas, $q$ is the particle charge in units of electron charge and $E$ is the particle energy in giga electron volts (GeV). Eq. (3) shows that, to maintain a constant radius of curvature as the particle is accelerated, $B$ must be ramped linearly with $E$.

The electrical fields are provided by Radio Frequencies (RF) cavities which can be superconducting [2,3]. In large machines, the bending and focusing functions are separated: the former is provided by dipole magnets whereas the latter is provided by pairs of focusing/defocusing quadrupole magnets (see the discussion that follows). The magnets are arranged around the ring in a regular lattice of cells, each made up of a focusing quadrupole, a set of bending dipoles, a defocusing quadrupole and another set of bending dipoles [4]. During acceleration, the field and field gradient of the dipole and quadrupole magnets are raised in proportion to particle momentum to maintain the beam on the design orbit and to preserve its size and intensity.

## 1.3 BENDING AND FOCUSING MAGNETS

### 1.3.1 COORDINATE SYSTEM DEFINITIONS

Let $(O,\vec{u},\vec{v},\vec{w})$ designate a rectangular coordinate system and let (C) be a circle of center O, located in the $(\vec{u},\vec{v})$ plane and representing the design orbit of an accelerator ring. Furthermore, let P be a given point of (C) and let $(P,\vec{x},\vec{y},\vec{z})$ designate a rectangular coordinate system associated with P, such that $\vec{x}$ is a unit vector parallel to (OP), $\vec{y}$ and $\vec{w}$ are one and the same and $\vec{z}$ is tangent to (C) at P. The $x$-axis defines the horizontal direction, the $y$-axis defines the vertical direction and the $z$-axis corresponds to the main direction of particle motion.

### 1.3.2 NORMAL DIPOLE MAGNET

A normal dipole magnet is a magnet, which, when positioned at P, produces within its aperture a two-dimensional magnetic flux density parallel to the $(\vec{x}, \vec{y})$ plane and such that

$$B_x = 0 \qquad \text{and} \qquad B_y = B_1 \tag{4}$$

where $B_x$ and $B_y$ are the $x$- and $y$-components of the magnetic flux density and $B_1$ is a constant referred to as the *dipole field strength* (in teslas).

A charged particle traveling along the direction of the $z$-axis through the aperture of such a magnet describes an arc of circle parallel to the horizontal $(\vec{x}, \vec{z})$ plane. The angular deflection, $\phi$, of the particle trajectory can be estimated as

$$\phi \approx \frac{0.3\, q\, B_1\, l_d}{E} = \frac{l_d}{\chi} \tag{5}$$

Here, $\phi$ is in radians, $q$ is in units of electron charge, $B_1$ is in teslas, $E$ is in GeV and $l_d$ is the dipole magnetic length in meters. Note that the effect of a dipole magnet on a beam of charged particles is similar in some respects to that of a prism on a light ray.

### 1.3.3 NORMAL QUADRUPOLE MAGNET

A normal quadrupole magnet is a magnet, which, when positioned at P, produces within its aperture a two-dimensional magnetic flux density parallel to the $(\vec{x}, \vec{y})$ plane and such that

$$B_x = g\, y \qquad \text{and} \qquad B_y = g\, x \tag{6}$$

where $g$ is a constant referred to as the *quadrupole field gradient* (in teslas per meter).

A beam of positively charged particles traveling along the direction of the $z$-axis through the aperture of such a magnet is horizontally focused and vertically defocused when $g$ is positive, and vertically focused and horizontally defocused when $g$ is negative. In reference to its action along the $x$-axis (on a beam of positively charged particles traveling in the positive $z$-direction), a magnet with a positive gradient is called a *focusing* quadrupole magnet, while a magnet with a negative gradient is called a *defocusing* quadrupole magnet. To obtain a net focusing effect along both $x$- and $y$-axes, focusing and defocusing quadrupole magnets must be alternated in the magnet lattice.

The effect of focusing/defocusing quadrupole magnets on a beam of charged particles is similar to that of convex/concave lenses on a light ray. For both types of quadrupole magnets, the focal length, $f$, which can be estimated as

$$f \approx \frac{E}{0.3\, q\, g\, l_q} \tag{7}$$

Here, $f$ is in meters, $E$ is in GeV, $q$ is in units of electron charge, $g$ is in teslas per meter and $l_q$ is the quadrupole magnetic length in meters.

# 2 PARTICLE ACCELERATORS AND SUPERCONDUCTIVITY

## 2.1 WHY SUPERCONDUCTIVITY?

Throughout the years, the quest for elementary particles has promoted the development of accelerator complexes producing beams of increasingly higher energies. Eq. (3) shows that, for a synchrotron, the particle energy is directly related to the product ($\chi B$). Hence, to reach higher energies, one must increase either the accelerator radius or the dipole field (or both). Increasing the accelerator radius means a longer tunnel. Increasing the dipole field above 2 T implies the use of superconducting magnets. The trade-off between tunneling costs, magnet development costs and accelerator operating costs is, since the late 1970's, in favor of using superconducting magnets generating the highest possible fields and field gradients [4].

Superconductivity is a unique property exhibited by some materials at low temperatures where the resistivity drops to zero. As a result, materials in the superconducting state can transport current without power dissipation by the Joule effect. This offers at least two advantages for large magnet systems such as those needed in accelerator main rings: (1) significant reduction in electrical power consumption and (2) possibility of relying on much higher overall current densities in the magnets coils. There are, however, at least three drawbacks in using superconducting magnets: (1) superconductors generate magnetization effects which result in field distortions that have to be corrected (see section on field quality), (2) to reach the superconducting state, the magnets must be cooled down and maintained at low temperatures, which requires large cryogenic systems (see section on magnet cooling) and (3) it may happen that an energized magnet, initially in the superconducting state, abruptly and irreversibly switches back to the normal resistive state in a phenomenon referred to as a *quench* (see section on quench performance).

The occurrence of a quench causes an instantaneous beam loss and requires that all or part of the magnet ring be rapidly ramped down to limit conductor heating and possible damage in the quenching magnet (see section on quench protection). Once the quenching magnet is discharged, it can be cooled down again and restored into the superconducting state, and the machine operations can resume. Hence, a quench is seldom fatal but it is always a serious disturbance. All must be done to prevent it from happening and all cautions must be taken to ensure the safety of the installation when it does happen.

## 2.2 REVIEW OF SUPERCONDUCTING PARTICLE ACCELERATORS

### 2.2.1 TEVATRON

The first large scale application of superconductivity was the Tevatron, a proton synchrotron with a circumference of 6.3 km built at Fermi National Accelerator Laboratory (FNAL) near Chicago, Illinois and commisioned in 1983 [5]. The Tevatron now operates as a proton/antiproton collider with a maximum energy of 900 GeV per beam. It relies on about 1000 superconducting dipole and quadrupole magnets, with a maximum operating dipole field of 4 T [6–10].

### 2.2.2 HERA

The next large particle accelerator to rely massively on superconducting magnet technology was HERA (Hadron Elektron Ring Anlage) built at DESY (Deutsches Elektronen–SYnchrotron) near Hamburg, Germany and commissioned in 1990 [11]. HERA is an electron/proton collider with a circumference of 6.3 km. It includes two large rings: (1) an electron ring, relying on conventional magnets (maximum energy: 30 GeV) and (2) a proton ring, relying on superconducting magnets (maximum energy: 820 GeV). The superconducting dipole magnets of the proton ring were developed at DESY and have a maximum operating field of 4.7 T [12–14]. The superconducting quadrupole magnets were developed at CEA/Saclay (Commissariat à l'Energie Atomique at Saclay near Paris, France) [15,16].

### 2.2.3 UNK

Since the early 1980's, the Institute for High Energy Physics (IHEP) located in Protvino, near Moscow, Russia is working on a project of proton accelerator named UNK (Uskoritelno-Nakopitelniy Komplex). The circumference of the main ring is 21 km for a maximum energy of 3 TeV in a fixed target mode [17]. The maximum operating dipole field is 5 T [18]. A number of superconducting dipole and quadrupole magnet prototypes have been built and cold-tested and the tunnel is almost completed, but, given the present economical situation in Russia (1998), the future of the machine is undecided.

### 2.2.4 SSC

In the mid 1980's, the USA started the Superconducting Super Collider (SSC) project, a giant proton/proton collider with a maximum energy of 20 TeV per beam [19]. The last stage of the SSC complex would have been made up of two identical rings of superconducting

magnets installed on top of each other in a tunnel with a circumference of 87 km. The maximum operating dipole field was 6.8 T. The project was eventually cancelled in October 1993 by decision of the United States Congress, after 12 miles of tunnel had been dug near Dallas, Texas, and a successful superconducting magnet R&D program had been carried out [20–27].

### 2.2.5 RHIC

Brookhaven National Laboratory (BNL), located on Long Island, New York, will complete in 1999 the construction on its site of the Relativistic Heavy Ion Collider (RHIC). RHIC is designed to collide beams of nuclei as heavy as gold, accelerated in two identical rings to energies between 7 and 100 GeV per beam and per unit of atomic mass [28]. Each ring has a circumference of 3.8 km; the maximum operating dipole field is 3.4 T [29–31].

### 2.2.6 LHC

In December 1994, the European Laboratory for Particle Physics (CERN) approved the construction of the Large Hadron Collider (LHC) in its existing 27-km-circumference tunnel located at the Swiss/French border, near Geneva, Switzerland [32]. LHC will be a proton/proton collider with a maximum energy of 7 TeV per beam. It will have a single ring of so-called *twin-aperture* superconducting magnets, housing within the same mechanical structure, the pipes for two counter-rotating proton beams. The dipole magnets are developed at CERN and have a maximum operating dipole field of 8.36 T [33-35]. The quadrupole magnets are developed at CEA/Saclay [36–38]. Commissioning is planned for 2005.

## 2.3 PROMINENT FEATURES OF SUPERCONDUCTING ACCELERATOR MAGNETS

Selected parameters of the major superconducting particle accelerators are summarized in Table 1, while Figs. 1(a) through 1(e) present cross-sectional views of the Tevatron, HERA, SSC, RHIC and LHC dipole magnets in their cryostats [39].

The magnets rely on similar design principles which are detailed in the oncoming sections. The field is produced by saddle shape coils that, in their long straight sections, approximate $\cos\theta$ conductor distributions for dipole magnets and $\cos 2\theta$ conductor distributions for quadrupole magnets. The coils are wound from Rutherford-type cables made of NbTi multifilamentary strands and are mechanically restrained by means of laminated collars. The collared-coil assembly is placed within an iron yoke providing a return path for the magnetic

flux. In the case of the Tevatron, the collared-coil assembly is cold while the iron yoke is warm. Starting with HERA, the iron yoke is included in the magnet cryostat and the cold mass is completed by an outer shell delimiting the region of helium circulation. In the case of LHC, the cold mass includes two collared-coil assemblies within a common iron yoke. Tevatron, HERA, UNK, SSC and RHIC magnets are cooled by boiling helium at 1 atmosphere (4.2 K) or supercritical helium at 3 to 5 atmosphere (between 4.5 and 5 K) while LHC magnets are cooled by superfluid helium at 1.9 K.

## 2.4 SUPERCONDUCTING ACCELERATOR MAGNET R&D

A number of laboratories are presently involved in R&D work on high field or high field gradient accelerator magnets. Among them is Twente University, located near Enschede in the Netherlands, which, in 1995, cold-tested at CERN a short dipole magnet model (made with $Nb_3Sn$ cable) which reached 11 T on its first quench at 4.4 K [40,41]. Soon after, in early 1997, Lawrence Berkeley National Laboratory (LBNL), located in Berkeley, California cold-tested a short dipole magnet model (also made with $Nb_3Sn$ cable), referred to as D20, which, after a number of training quenches, reached a record dipole field of 13.5 T at 1.8 K [42,43].

# 3 CONDUCTOR AND CONDUCTOR INSULATION

## 3.1 PRACTICAL SUPERCONDUCTORS

### 3.1.1 SUPERCONDUCTING MATERIALS

#### *3.1.1.1 NbTi*

The most widely used superconductor is a ductile alloy of niobium and titanium (NbTi) [44–46]. Niobium and titanium, which have very similar atomic sizes, are mutually soluble over a wide composition range [47,48]. At high temperatures, they combine into a body-centered cubic phase, referred to as *β–phase*. When cooled down to temperatures below about 9 K, the β–phase becomes a type-II superconductor. Furthermore, when the alloy is severely cold-worked and presents a large number of lattice dislocations, heat treatments at moderate temperatures lead to precipitations of other phases at grain boundaries. Among them is an hexagonal close packed phase, rich in titanium (of the order of 95% in weight), referred to as *α–phase*. The α–phase remains normal resistive at low temperatures and has been shown to be a significant source of fluxon pinning sites [49,50]. The α–Ti precipitates can be engineered to achieve high critical current densities in the desired ranges of operating field and temperature.

The critical temperature, $T_C$, and the upper critical magnetic flux density, $B_{C2}$, of niobium-titanium are mainly determined by the alloy composition and are little affected by subsequent processing. The Ti content of practical conductors is in the range 45 to 50% in weight and corresponds to an optimum in $B_{C2}$. For such alloy compositions, the critical temperature at zero magnetic flux density, $T_{C0}$, is between 9 and 9.2 K and the upper critical magnetic flux density at zero temperature, $B_{C20}$, is about 14.5 T. The upper critical magnetic flux density can be raised slightly by addition of a high-atomic-number ternary component such as tantalum [51]. The increase in $B_{C2}$ is small at 4.2 K (0.1 to 0.2 T) but can reach 1 T at 1.8 K.

The critical current density, $J_C$, is mainly determined by the microstructure of the alloy. It can be optimized by submitting the alloy to a succession of cold-work cycles and heat treatments. The heat treatments are carried out as to favor the development of α–Ti precipitates, while preventing the formation of other phases which may be deleterious [52,53]. The optimization parameters have been well studied for binary NbTi, but much less work has been carried out on ternary alloys [54]. At present, only binary niobium-titanium is used for large scale applications.

The best performing dipole magnet relying on binary NbTi conductor is a short LHC dipole magnet model, referred to as MFISC, which was built at CERN and which reached 10.53 T at 1.77 K [55,56]. Magnet designers consider that this is about the limit for NbTi and that, to produce higher fields, it is necessary to change material.

#### *3.1.1.2 $Nb_3Sn$*

The only other superconducting material that is readily available at (small) industrial scale is an intermetallic compound of niobium and tin ($Nb_3Sn$) belonging to the A15 crystallographic family [44–46]. $Nb_3Sn$ is also a type-II superconductor, with a critical temperature at zero magnetic flux density and zero strain, $T_{C0m}$, of the order of 16 K and an upper critical magnetic flux density at zero temperature and zero strain, $B_{C20m}$, of the order of 24 T. The superconducting properties can be significantly enhanced by a small addition of titanium or tantalum, bringing $T_{C0m}$ to about 18 K and $B_{C20m}$ to about 28 T. However, the formation of binary or ternary compounds requires a heat treatment at temperatures up to 700 °C for times up to 300 hours in a vacuum or in inert atmosphere such as argon. Furthermore, once reacted, the compounds become brittle and their superconducting properties are strain sensitive [57,58]. The processing difficulties and the higher cost of $Nb_3Sn$ have so far limited its use. As already mentioned, the highest dipole field reached on a $Nb_3Sn$ magnet is 13.5 T at 1.8 K [42,43].

#### *3.1.1.3 HTS*

Although great progresses have been made in the development of so-called *High Temperature Superconductors* (HTS), such as bismuth copper oxydes, $Bi_2Sr_2CaCu_2O_x$ and $(Bi,Pb)_2Sr_2Ca_2Cu_3O_x$, and yttrium copper oxides, $YBa_2Cu_3O_7$, these materials are not ready yet for applications requiring low costs, mass-production and high critical current densities [59].

### 3.1.2 SUPERCONDUCTING MULTIFILAMENTARY COMPOSITES

For practical applications, the superconductor is subdivided into fine filaments, which are twisted together and embedded in a low resistivity matrix of normal metal. The subdivision into fine filaments is required to eliminate instabilities in the superconductor known as *flux jumping* [chapter 7 of Reference 60]. The filament twisting is introduced to reduce inter-filament coupling under time-varying fields [chapter 8 of Reference 60]. The low resistivity matrix is used as current shunt in the case of transition of the filaments to the normal resistive state, thereby limiting power dissipation and conductor heating (the resistivity of

superconductors in the normal state is usually much larger than the low-temperature resistivity of normal metals such as high purity copper or aluminum).

Accelerator magnets rely on cables made from round wires of superconducting multifilamentary composites. Except for a few R&D magnet models, the filaments are made of binary niobium-titanium alloy and the matrix is high purity copper. Wire diameter ranges from 0.5 to 1.3 mm. For accelerator magnets, there is an additional requirement on filament diameter in order to limit field distortions resulting from superconductor magnetization (see section on field quality). The superconductor magnetization per unit volume can be shown to be directly proportional to filament diameter [p. 166 of Reference 60] and to minimize its effects it is desirable to use fine filaments. The filament diameter of HERA wires is of the order of 15 μm while that of SSC, RHIC and LHC wires is of the order of 5 μm. The copper-to-superconductor ratio, $\lambda$ (defined as the ratio of the area of copper to the area of niobium-titanium in the wire cross-section), varies from 1.3 to 1.8, except for RHIC wire where it is 2.25. There are several thousand filaments per wire.

### 3.1.3 TRANSITION OF MULTIFILAMENTARY WIRES

#### *3.1.3.1 Voltage-Current Curve*

The maximum current-carrying capacity of a superconducting multifilamentary composite wire at a given temperature and field can be determined by measuring the voltage-current curve of a wire short sample. As illustrated in Fig. 2(a), the transition from the superconducting state to the normal resistive state is not abrupt but takes place over a certain current range. At low transport currents, the voltage, $V$, across the wire short sample is nil. Then, as the current, $I$, is increased, there appears a domain where $V$ becomes non-zero and starts to rise. At the beginning, the voltage rise is reversible, *i.e.*, if the current is lowered, the voltage decreases following the same curve as during the up-ramp. However, above a certain current, the phenomenon becomes irreversible, and the voltage takes off rapidly and uncontrollably. Such irreversible voltage run-away is the signature of a quench. The current at which the run-away occurs is referred to as *quench current*, $I_q$.

#### *3.1.3.2 Critical Current*

For the particular environment of the wire short sample in its test set-up, a quench only occurs when the current reaches $I_q$. However, for a different environment with different cooling conditions (*e.g.*, when the wire is part of a cable that is wound in a magnet coil), the quench current may be different. The question then arises of what engineering value to use to

characterize the maximum current capability of a wire in a magnet environment. This engineering value is referred to as *critical current*, $I_C$, and is defined by relying on empirical criterions.

To explain these criterions, let us consider a sample of multifilamentary composite wire of length, $L$, cross-sectional area, $S$, and overall copper-to-superconductor ratio, $\lambda$, and let $V$ designate the voltage across the wire sample. An apparent electrical field, $E_s$, and an apparent resistivity of the superconductor, $\rho_s$, can be defined as

$$E_s = \frac{V}{L} \qquad \text{and} \qquad \rho_s = \frac{1}{1+\lambda}\frac{V}{L}\frac{S}{I} \tag{8}$$

For NbTi and $Nb_3Sn$ wires, the two criterions the most commonly used to define the critical current are: (1) the current value corresponding to an apparent electrical field, $E_C$, of 0.1 μV/cm or (2) the current value corresponding to an apparent resistivity of the superconductor, $\rho_C$, of $10^{-14}$ Ωm. (Note that the latter definition is preferred in the accelerator magnet community.)

The critical current determined by either of the aforementioned criterions is usually lower than the quench current. It can be translated into an average critical current density in the superconductor, $J_C$, by writing

$$I_C = J_C \frac{S}{1+\lambda} \tag{9}$$

It is verified in the section on quench performance that the critical current values can be used to make accurate estimations of the maximum quench currents of accelerator magnets.

*3.1.3.3 N–Value*

To fully characterize the wire, it is also interesting to quantify the sharpness of the transition from the superconducting to the normal resistive state. This can be done by plotting $\ln(V)$ (or $\ln(\rho_s)$), as a function of $\ln(I)$.

As illustrated in Fig. 2(b) for the data of Fig. 2(a), it appears that $\ln(V)$ (and similarly, $\ln(\rho_s)$) increases quasi-linearly as a function $\ln(I)$ over a broad range (typically from $E_C$ to $10E_C$ or $\rho_C$ to $10\rho_C$). Hence, the onset of the resistive transition can be fitted by simple power laws of the form

$$\frac{V}{V_C} = \left(\frac{I}{I_C}\right)^N \qquad \text{or} \qquad \frac{\rho_s}{\rho_C} = \left(\frac{I}{I_C}\right)^N \tag{10}$$

where $V_C$ is the voltage across the wire sample corresponding to $E_C$. The index $N$ is referred to as *resistivity transition index*, or more simply, *N-value*. It is representative of the curvature of the voltage-current curve: the larger $N$, the sharper the transition.

The $N$-value, like $I_C$, depends on temperature and field [61]. Its field dependence can be used as a criterion to determine if the critical current is limited by intrinsic factors, related to fluxon-microstructure interactions within the superconducting material, or by extrinsic parameters, related to macroscopic irregularities, such as local reductions in filament cross-sectional areas [62]. In the case of NbTi wires, there is a clear correlation between filament distortions, often referred to as *sausaging*, and $N$-value: the wider the distribution of filament diameters in the wire cross-section, the lower the $N$-value [63]. A typical $N$-value for SSC wire is 30 at 4.2 K and 5 T.

## 3.2 NBTI WIRES

### 3.2.1 PROCESSING

NbTi alloys are very ductile and have very low work-hardening coefficients making them easy to co-process with copper. A multifilamentary wire is fabricated by extrusion and drawing of a so-called *multi-filament billet.* The multi-filament billet is constituted of hexagonal, mono-filament rods stacked into a thick-walled copper can. There are as many rods in the multi-filament billet as filaments in the final wire. The rods themselves are produced by extrusion and drawing of a so-called *mono-filament billet.* The mono-filament billet is constituted of a cylindrical ingot of high homogeneity niobium-titanium alloy inserted into a copper can.

The drawing-down of the billets is realized in multiple passes and heat treatments are applied at well defined strain intervals (corresponding to integer numbers of standard die passes). The cold-work and heat treatment schedule is established as to produce the desired amount of $\alpha$–Ti precipitates and to reduce the dimensions and spacing of these precipitates to optimum sizes for fluxon pinning. As the characteristics of the fluxon lattice depends on temperature and field, the schedule may be different for different applications with different operating conditions. The wire twist is applied prior to the final drawing pass, with a typical twist pitch of 25 mm. Figure 3(a) presents a cross-sectional view of a LHC wire at final size [64].

For the production of fine filament wires, such as those used for SSC, RHIC and LHC, the niobium-titanium ingot of the mono-filament billet is wrapped with a niobium foil. The niobium barrier prevents the formation, during the multiple heat treatments, of hard and brittle intermetallic compounds such as $TiCu_4$. The $TiCu_4$ compounds do not deform well, resulting in filament sausaging and, ultimately, wire breakages upon subsequent drawing operations [65].

When the number of filaments is very large, rods made from a drawn-down multi-filament billet can be re-stacked into a new multi-filament billet, which, in turn is extruded and drawn. Such process is referred-to as *double-stacking* as opposed to *single-stacking*.

### 3.2.2 DESIGN AND MANUFACTURING ISSUES

The main issues for NbTi wire design are: (1) copper-to-superconductor ratio, which should not be too small to limit conductor heating in case of a quench and should not be too large to achieve a high overall critical current, (2) filament size, which should be optimized to limit field distortions resulting from superconductor magnetization while keeping wire processing cost down and (3) inter-filament spacing, which should not be too large to allow mutual support of the filaments during wire processing (see the discussion that follows) and should not be too small to avoid proximity effect coupling [66]. The inter-filament spacing is determined by the local copper-to-superconductor ratio of the mono-filament rod assembly in the stacking of the multi-filament billet. For sub-micrometer inter-filament spacing, the proximity effect coupling can be limited by doping the copper of the mono-filament billet with manganese [67]. In addition, it is desirable to leave a copper core at the wire center and a copper sheath at the wire periphery to protect the multifilamentary area from cabling degradation. For SSC and LHC wires, the interfilament spacing is of the order of 1 μm (which does not require Mn doping), the cross-sectional area of the copper core is less than 10% of the total wire cross-sectional area and the thickness of the copper outer sheath is in the range 50 to 100 μm.

The main issues regarding wire manufacturing are: (1) piece length and (2) critical current optimization. Breakages during wire drawing are unavoidable, resulting in multiple piece lengths. As most magnet builders prefer to wind coils with weld-free cables made from single-piece wires, the average wire piece length must be at least equal to the cable length needed for a coil. Also, a low breakage rate in wire production is an assurance of quality and uniformity. For LHC, wires are accepted on a billet basis, and it is required that, for each billet, at least 90% of the final-size pieces be longer than 1 km. The factors influencing piece length are: (1) cleanliness of billet assembly, to avoid inclusions of foreign particles,

(2) precipitation of unwanted, hard-to-draw phases in NbTi alloy, which must be prevented and (3) formation of $TiCu_4$ compounds at the matrix/filament interface, which must be limited. As already mentioned, the formation of $TiCu_4$ compounds can be restricted by surrounding the filaments with niobium barriers, but it has been shown that the barriers were not totally impermeable to Cu and Ti diffusion when subjected to multiple heat treatments [68].

The factors influencing critical current density can be classified into two categories: (1) intrinsic factors, related to NbTi alloy microstructure and affecting fluxon pinning and (2) extrinsic factors, related to macroscopic irregularities and causing local reductions in filament cross-sectional areas. Among the intrinsic factors are: (1) homogeneity of the NbTi ingots used for the mono-filament billets, which must be tightly controlled (typically +/- 1% in weight of Ti) and (2) parameters and schedule of cold-work and heat treatment cycles during wire production. The extrinsic factors are basically the same as the factors influencing piece length. In addition, it is preferable to maintain a small inter-filament spacing, so that the NbTi filaments, which are much harder than the high purity copper matrix, can support each other during the multiple drawing operations. As we have seen, a way of determining if the critical current of a wire is limited by intrinsic or extrinsic parameters, is to study the evolution of its $N$-value as a function of field.

### 3.2.3 CRITICAL SURFACE PARAMETRIZATION

The upper critical magnetic flux density, $B_{C2}$, of binary NbTi can be estimated as a function of temperature, $T$, using [69]

$$B_{C2}(T) = B_{C20}\left[1 - \left(\frac{T}{T_{C0}}\right)^{1.7}\right] \tag{11}$$

where $B_{C20}$ is the upper critical magnetic flux density at zero temperature (about 14.5 T) and $T_{C0}$ is the critical temperature at zero magnetic flux density (about 9.2 K).

The critical current density, $J_C$, can be parametrized as a function of temperature, magnetic flux density, $B$, and critical current density at 4.2 K and 5 T, $J_{Cref}$, using [70]

$$\frac{J_C(B,T)}{J_{Cref}} = \frac{C_0}{B}\left[\frac{B}{B_{C2}(T)}\right]^{\alpha}\left[1 - \frac{B}{B_{C2}(T)}\right]^{\beta}\left[1 - \left(\frac{T}{T_{C0}}\right)^{1.7}\right]^{\gamma} \tag{12}$$

where $C_0$, $\alpha$, $\beta$ and $\gamma$ are fitting parameters.

Since the time of Tevatron, a factor of about 2 has been gained on the critical current density at 4.2 K and 5 T, thanks to the understanding of the role played by α–Ti precipitates in pinning mechanisms. Values of $J_{Cref}$ in excess of 3000 A/mm$^2$ are now obtained in industrial production [71]. Typical fitting parameters values for LHC strands are: $C_0$ = 30 T, $\alpha$ = 0.6, $\beta$ = 1.0 and $\gamma$ = 2.0. Note that the "$J_C$ versus $B$" curve shifts by about +3 T when lowering the temperature from 4.2 K to 1.9 K.

## 3.3 $NB_3SN$ WIRES

### 3.3.1 PROCESSING

There are at least four ways of industrially processing $Nb_3Sn$ multifilamentary wires, which are well described in the literature [44–46]: (1) bronze process, (2) internal-tin process, (3) Modified Jelly Roll (MJR) process and (4) Powder-In-Tube (PIT) process. Each process has its advantages and its disadvantages and none of them is fully satisfactory. Figure 3(b) presents a cross-sectional view of an un-reacted, internal-tin wire at final size [64].

Given that reacted $Nb_3Sn$ conductors are very fragile and cannot be bent on small radii, the manufacturing of $Nb_3Sn$ coils calls for special fabrication processes which are risky and onerous. In the case of accelerator magnet coils, the cable is manufactured and wound un-reacted, and the whole coil is subjected to heat-treatment, according to the so-called *wind-and-react* technique.

### 3.3.2 CRITICAL SURFACE PARAMETRIZATION

The upper critical magnetic flux density, $B_{C2}$, of binary or ternary $Nb_3Sn$, can be estimated as a function of temperature, $T$, and strain, $\varepsilon$, using [72]

$$\frac{B_{C2}(T,\varepsilon)}{B_{C20}(\varepsilon)} = \left[1 - \left(\frac{T}{T_{C0}(\varepsilon)}\right)^2\right]\left\{1 - 0.31\left(\frac{T}{T_{C0}(\varepsilon)}\right)^2\left[1 - 1.77\ \ln\left(\frac{T}{T_{C0}(\varepsilon)}\right)\right]\right\} \quad (13)$$

where $B_{C20}$ is the upper critical magnetic flux density at zero temperature

$$B_{C20}(\varepsilon) = B_{C20m}\,(1 - a|\varepsilon|^{1.7}) \quad (14)$$

and $T_{C0}$ is the critical temperature at zero magnetic flux density

$$T_{C0}(\varepsilon) = T_{C0m}\,(1 - a|\varepsilon|^{1.7})^{1/3} \quad (15)$$

Here, $a$ is a parameter equal to 900 for compressive strain ($\varepsilon \leq 0$) and to 1250 for tensile strain ($0 \leq \varepsilon$), $B_{C20m}$ is the upper critical magnetic flux density at zero temperature and zero strain and $T_{C0m}$ is the critical temperature at zero magnetic flux density and zero strain. For binary compounds, $T_{C0m}$ and $B_{C20m}$ can be taken equal to 16 K and 24 T, while for ternary compounds, they can be taken equal to 18 K and 28 T.

The critical current density can be parametrized as a function of temperature, magnetic flux density, $B$, and strain, using [72]

$$J_C(B,T,\varepsilon) = \frac{C(\varepsilon)}{\sqrt{B}} \left[1 - \frac{B}{B_{C2}(T,\varepsilon)}\right]^2 \left[1 - \left(\frac{T}{T_{C0}(\varepsilon)}\right)^2\right]^2 \tag{16}$$

where

$$C(\varepsilon) = C_0 \left(1 - a|\varepsilon|^{1.7}\right)^{1/2} \tag{17}$$

Here $C_0$ is a fitting parameter.

In recent years, a significant R&D work has been carried out to improve the performance of $Nb_3Sn$ multifilamentary wires, thanks to the International Thermonuclear Experimental Reactor (ITER) program [73]. Critical current density values of 750 A/mm$^2$ at 4.2 K and 12 T with effective filament diameters of 15 to 20 μm are now reached in industrial production [74]. Such values correspond to a $C_0$ of the order 12000 AT$^{1/2}$mm$^{-2}$. Note that the strain in a freestanding $Nb_3Sn$ multifilamentary wire is estimated at about –0.25%.

## 3.4 RUTHERFORD-TYPE CABLE

Superconducting particle accelerator magnet coils are wound from so-called *Rutherford-type* cables. As illustrated in Figs. 4(a) and 4(b), a Rutherford-type cable consists of a few tens of strands, twisted together, and shaped into a flat, two-layer, slightly keystoned cable [46,75]. As explained in the section on magnetic design, the slight keystone is introduced to allow stacking of the conductors into an arch and forming coils of the desired shape.

The small radii of curvature of the coil ends preclude the use of a monolithic conductor because it would be too hard to bend. A multi-strand cable is preferred to a single wire for at least four reasons: (1) it limits the piece length requirement for wire manufacturing (a coil wound with a $N$-strand cable requires piece lengths which are $1/N$ shorter than for a similar coil wound with a single wire), (2) it allows strand-to-strand current redistribution in the case of a

localized defect or when a quench originates in one strand [76, 77], (3) it limits the number of turns and facilitates coil winding, and (4) it limits coil inductance (the inductance of a coil wound with a $N$-strand cable is $1/N^2$ smaller than that of a similar coil wound with a single wire). A smaller inductance reduces the voltage requirement on the power supply to ramp-up the magnets to their operating current in a given time and limits the maximum voltage to ground in the case of a quench (see quench protection section). The main disadvantage of using a cable is the high operating current (over a few thousand ampères) which requires large current supplies and large current leads.

The main issues for cable design and fabrication are: (1) compaction, which should be large enough to ensure good mechanical stability and high overall current density while leaving enough void (typically a few percent in volume) for liquid helium cooling, (2) control of outer dimensions to achieve suitable coil geometry and mechanical properties, (3) limitation of critical current degradation due to strand and filament degradations at the cable edges [78,79] and (4) control of interstrand resistance, which should not be too small to limit field distortions induced by interstrand coupling currents while ramping (see section on field quality) and should not be too large to allow current redistribution among cable strands.

The interstrand resistance can be modified by oxidizing or by coating strand surface [80,81]. Also, a thin, insulating foil (such as stainless steel) can be inserted between the two layers of cable strands in order to increase the resistances at the strand crossovers [82]. The strands used of the HERA and LHC cables are coated with a silver-tin solder, called *stabrite*. Half of the strands of the Tevatron cable are coated with stabrite, while the other half are insulated with a black copper oxide, called *ebanol*. The strands of the UNK, SSC and RHIC cables are bare. Up to now, no foiled cable has been used in a magnet.

At the end of cabling, the high purity copper of the strand matrix is heavily cold-worked and can require a low temperature annealing. This annealing should not be too aggressive to prevent alterations of the niobium-titanium alloy microstructure. The LHC cables are subjected to a heat treatment at 200 °C for 8 to 12 hours on special reels allowing air circulation. This heat treatment is also performed to oxidize the stabrite coating on the cable strands and achieve a suitable level of crossover resistance ($20\pm10\ \mu\Omega$).

Similarly to wires, the maximum current-carrying capacity of cables can be determined from measurements on short samples. The voltage-current curves of cable short samples are similar to that of wire short samples and the cable performances can be characterized using the same definitions of critical current and $N$-value. BNL has developed a cable short sample test facility that is widely used as a bench mark for NbTi Rutherford-type cables [83]. The critical

current of $Nb_3Sn$ Rutherford-type cables has been shown to be sensitive to transverse pressure and requires elaborate test setups to be measured in conditions relevant to accelerator magnet operations [84,85].

## 3.5 CABLE INSULATION

### 3.5.1 INSULATION REQUIREMENTS

The main requirements for cable insulation are: (1) good dielectric strength in helium environment and under high transverse pressure (up to 100 MPa), (2) small thickness (to maximize overall current density in the magnet coil) and good physical uniformity (to ensure proper conductor positioning for field quality), (3) retention of mechanical properties over a wide temperature range, and (4) ability to withstand radiations in an accelerator environment. In addition, the insulation system is required to provide a mean of bonding the coil turns together to give the coil a semi rigid shape and facilitate its manipulation during the subsequent steps of magnet assembly. It is also desirable that the insulation be somewhat porous to helium for conductor cooling. Note that the dielectric strength of helium gas at 4.2 K is far worse than that of liquid helium and that it degrades significantly with increasing temperature [86].

### 3.5.2 INSULATION OF NBTI CABLES

The insulation of Tevatron, HERA and UNK magnets, of most SSC magnets and of the early LHC magnet models is made up of one or two inner layers of polyimide film, wrapped helically with a 50-to-60% overlap, completed by an outer layer of resin-impregnated glass fiber tape, wrapped helically with a small gap. The inner layer is wrapped with an overlap for at least two reasons: (1) the polyimide film may contain pin holes which have to be covered (the probability of having two superimposed pin holes in the overlapping layer is very low) and (2) the Tevatron experience has shown that it was preferable to prevent the resin impregnating the glass wrap from entering in contact with the NbTi cable (the energy released by cracks in the resin is believed to be sufficient to initiate a quench) [p. 784 of Reference 6]. The outer layer is wrapped with a gap to set up helium cooling channels between coil turns. The resin is of thermosetting-type and requires heat to increase cross link density and cure into a rigid bonding agent. The curing is realized after winding completion in a mold of very accurate dimensions to control coil geometry and Young's modulus [87].

RHIC magnets and the most recent LHC magnet models use a so-called *all-polyimide* insulation where the outer glass fiber wrap is replaced by another layer of polyimide film with a polyimide adhesive on its surface [88]. The all-polyimide insulation has a better resistance to

puncture but the softening temperature of the adhesive can be higher than the temperature needed to cure a conventional resin (225 °C for RHIC-type all-polyimide insulation compared to 135 °C for SSC-type polyimide/glass insulation).

### 3.5.3 INSULATION OF $NB_3SN$ CABLES

The insulation of $Nb_3Sn$ cables is usually based on a glass fiber tape or a glass fiber sleeve put on the un-reacted conductor prior to winding. Upon winding completion, the coil is heat-treated to form $Nb_3Sn$. It is then transferred to a precision molding fixture to be vacuum impregnated with resin. The glass fibers used for the tape or the sleeve must be able to sustain the heat treatment without degradation. Also, all organic materials, such as sizing or finish, must be removed from the fibers to prevent the formation of carbon compounds that may lower the dielectric strength. The sizing removal is performed by carbonization in air prior to conductor insulation.

The implementation of such an insulation system adds to the difficulty of manufacturing $Nb_3Sn$ coils for at least two reasons: 1) de-sized glass fiber tapes or sleeves are fragile and easy to tear off by friction [89] and 2) vacuum impregnation is a delicate operation. Furthermore, a full impregnation prevents any helium penetration in the coil, thereby reducing greatly cooling capabilities.

# 4 MAGNETIC DESIGN

## 4.1 FIELD PRODUCED BY SIMPLE CURRENT DISTRIBUTIONS

### 4.1.1 SINGLE CURRENT LINE IN FREE SPACE

Let $(O,\vec{x},\vec{y},\vec{z})$ designate a rectangular coordinate system and let $(-I,R,\theta)$ designate a current line of intensity $(-I)$, parallel to the $z$-axis, and located at a position $\mathbf{s} = R\ \exp(i\theta)$ in the complex $(O,\vec{x},\vec{y})$ plane, as represented in Fig. 5(a). (The current line intensity is chosen to be negative to end up with positive a positive factor in the right member of Eq. (20).) The magnetic flux density, $\vec{B}$, produced by this current-line in free space can be computed using Biot and Savart's law. It is independent of $z$ and parallel to the $(\vec{x},\vec{y})$ plane. Its $x$- and $y$-components, $B_x$ and $B_y$, are given by

$$B_y + i\,B_x = -\frac{\mu_0 I}{2\pi}\frac{1}{(\mathbf{z}-\mathbf{s})} \tag{18}$$

where $\mu_0$ is the magnetic permeability of vacuum ($4\pi 10^{-7}$ H/m) and $\mathbf{z} = x + iy$.

The above expression can be expanded into a power series of the form [90]

$$B_y + i\,B_x = \sum_{n=1}^{+\infty} (B_n + i\,A_n)\ \mathbf{z}^{n-1} \qquad \text{for } \mathbf{z} = x + iy,\ |\mathbf{z}| < R \tag{19}$$

where $A_n$ and $B_n$ are constant coefficients, referred to as *skew* and *normal* $2n$-pole field coefficients, given by

$$B_n + i\,A_n = \frac{\mu_0 I}{2\pi R^n}\left[\cos(n\theta) - i\ \sin(n\theta)\right] \tag{20}$$

### 4.1.2 SINGLE CURRENT LINE WITHIN A CIRCULAR IRON YOKE

Let us now assume that the current line of Fig. 5(a) is located inside a circular iron yoke of inner radius, $R_y$, as represented in Fig. 5(b). The contribution of the iron yoke to the magnetic flux density can be shown to be the same as that of a mirror current line, of intensity, $(-I_m)$, and position, $\mathbf{s}_m$, in the complex plane, where

$$I_m = \frac{\mu-1}{\mu+1} I \qquad \text{and} \qquad \mathbf{s}_m = \frac{R_y^2}{\mathbf{s}^*} \tag{21}$$

Here $\mu$ designates the relative magnetic permeability of the iron yoke and $\mathbf{s}^*$ designates the complex conjugate of $\mathbf{s}$. Note that the mirror image method is only applicable if the iron yoke is not saturated and as long as its permeability is uniform.

### 4.1.3 QUADRUPLET OF CURRENT LINES WITH DIPOLE SYMMETRY

Let us now consider the quadruplet of current lines $(-I,R,\theta)$, $(+I,R,\pi-\theta)$, $(+I,R,\pi+\theta)$ and $(-I,R,-\theta)$, represented in Fig. 6(a). The magnetic flux density produced by this quadruplet can be estimated by summing the contributions from each current line. We get

$$B_y + iB_x = \sum_{k=0}^{+\infty} B_{2k+1}\, \mathbf{z}^{2k} \qquad \text{for } \mathbf{z} = x + iy,\ |\mathbf{z}| < R \tag{22}$$

where

$$B_{2k+1} = \frac{2\mu_0 I}{\pi R^{2k+1}} \cos\left[(2k+1)\theta\right] \tag{23}$$

The first term ($k = 0$) of the series corresponds to a pure normal dipole field parallel to the $y$-axis. The $B_{2k+1}$ coefficients are called the *allowed* multipole field coefficients of this current distribution.

### 4.1.4 OCTUPLET OF CURRENT LINES WITH QUADRUPOLE SYMMETRY

Similarly, the magnetic flux density produced by the octuplet of current lines represented in Fig. 6(b) is given by

$$B_y + iB_x = \sum_{k=0}^{+\infty} B_{4k+2}\, \mathbf{z}^{4k+1} \qquad \text{for } \mathbf{z} = x + iy,\ |\mathbf{z}| < R \tag{24}$$

where

$$B_{4k+2} = \frac{4\mu_0 I}{\pi R^{4k+2}} \cos\left[(4k+2)\theta\right] \tag{25}$$

The first term ($k = 0$) of the series corresponds to a pure normal quadrupole field whose axes are parallel to the first and second bisectors. For this current distribution, the allowed multipole field coefficients are the normal $2(4k+2)$-pole field coefficients.

### 4.1.5 COS$P\Theta$ AND SIN$P\Theta$ CURRENT SHEETS

Let us now consider a cylindrical current sheet of radius, $R$, carrying a linear current density of the form $[-j\cos(p\theta)]$ where $j$ is a constant (in A/m). The magnetic flux density produced within the cylinder can be computed by dividing the sheet into elementary current lines of intensity $[-jR\cos(p\theta)\mathrm{d}\theta]$ and by integrating their contributions over $(2\pi)$. We get

$$B_y + iB_x = B_p = \frac{\mu_0 j}{2R^{p-1}} \qquad \text{for } \mathbf{z} = x + iy,\ |\mathbf{z}| < R \tag{26}$$

Hence, a $\cos(p\theta)$-type current sheet produces a pure normal $2p$-pole field.

Similarly, it can be shown that a cylindrical current sheet of radius, $R$, carrying a linear current density $[+j\sin(p\theta)]$ produces a pure skew $2p$-pole field

$$B_y + iB_x = A_p = \frac{\mu_0 j}{2R^{p-1}} \qquad \text{for } \mathbf{z} = x + iy,\ |\mathbf{z}| < R \tag{27}$$

### 4.1.6 CYLINDRICAL CURRENT SHELLS

Let us now consider a cylindrical current shell of inner radius, $R_i$, outer radius, $R_o$, extending between the angles $(-\theta_0)$ and $(+\theta_0)$ in the half-space $x$, $x \geq 0$ and between the angles $(\pi-\theta_0)$ and $(\pi+\theta_0)$ in the half-space $x$, $x \leq 0$, and carrying an uniform current density $(-J)$ for $x$, $x > 0$ and $(+J)$ for $x$, $x < 0$, as represented in Fig. 7(a). The magnetic flux density produced within the cylinder can be computed by dividing the shell into quadruplets of current lines having the symmetry of Fig. 6(a) and carrying intensities $[\pm JR\mathrm{d}\theta\mathrm{d}R]$, and by integrating the quadruplet contributions over a shell quadrant. It follows that the magnetic flux density is given by Eq. (22), but the expressions of the multipole field coefficients become

$$B_1 = \frac{2\mu_0 J}{\pi}(R_o - R_i)\ \sin\theta_0 \tag{28a}$$

and

$$B_{2k+1} = \frac{2\mu_0 J}{\pi(2k+1)(2k-1)}\left(\frac{1}{R_i^{2k-1}} - \frac{1}{R_o^{2k-1}}\right)\ \sin\left[(2k+1)\theta_0\right] \qquad \text{for } k,\ k \geq 1 \tag{28b}$$

Note that $B_3$ (first allowed multipole field coefficient after $B_1$ in a current distribution with a dipole symmetry) is nil for $\theta_0 = \pi/3$.

In this configuration, the regions around $\theta = \pi/2$ and $\theta = 3\pi/2$, which are free of current, are referred to as *pole areas*, and the $y$-axis is referred to as *pole axis*. By extension, $\theta_0$ is the *pole angle*.

Similarly, it can be shown that the magnetic flux density produced by the current shell of Fig. 7(b) is given by Eq. (24), where

$$B_2 = \frac{2\mu_0 J}{\pi} \ln\left(\frac{R_o}{R_i}\right) \sin 2\theta_0 \tag{29a}$$

and

$$B_{4k+2} = \frac{\mu_0 J}{\pi k(4k+2)} \left(\frac{1}{R_i^{4k}} - \frac{1}{R_o^{4k}}\right) \sin\left[(4k+2)\theta_0\right] \qquad \text{for } k,\ k \geq 1 \tag{29b}$$

Note that $B_2$ corresponds to the quadrupole field gradient, $g$, and that $B_6$ (first allowed multipole field coefficient after $B_2$ in a current distribution with a quadrupole symmetry) is nil for $\theta_0 = \pi/6$.

In this configuration, the pole areas are the regions around $\theta = \pi/4$, $3\pi/4$, $5\pi/4$ and $7\pi/4$ and the pole axes are the first and second bisectors.

### 4.1.7 Cylindrical Current Shells Within a Circular Iron Yoke

Let us now place the cylindrical current shell of Fig. 7(a) within a circular iron yoke of inner radius, $R_y$. As represented in Fig. 8, the contribution of the iron yoke to the magnetic flux density can be shown to be the same as that of a mirror current shell, of inner radius, $R_{im}$, and outer radius, $R_{om}$, where

$$R_{im} = \frac{R_y^2}{R_o} \qquad \text{and} \qquad R_{om} = \frac{R_y^2}{R_i} \tag{30}$$

and carrying an uniform current density, $J_m$, such that

$$J_m = \frac{\mu-1}{\mu+1} \frac{R_o^2 - R_i^2}{R_{om}^2 - R_{im}^2} J = \frac{\mu-1}{\mu+1} \frac{R_o^2 R_i^2}{R_y^4} J \tag{31}$$

Here $\mu$ designates the relative magnetic permeability of the iron yoke. Eq. (31) expresses that the total intensity of the current circulating in the mirror shell is the same as that circulating in the original shell times the ratio ($\mu$–1/$\mu$+1) [p. 54 of Reference 4].

Introducing the expressions of the radii and of the current density of the mirror shell into Eqs. (28a) and (28b), it is easy to show that the contribution of the iron yoke to the $2n$-pole field coefficient, $B_n^{yoke}$, is

$$B_n^{yoke} = \frac{\mu-1}{\mu+1}\left(\frac{R_i R_o}{R_y^2}\right)^n B_n^{shell} \tag{32}$$

where $B_n^{shell}$ is the $2n$-pole field coefficient produced by the current shell alone.

Eq. (32) remains the same for a cylindrical current shell with a quadrupole symmetry placed within a circular iron yoke.

### 4.1.8 CYLINDRICAL CURRENT SHELLS WITH ANGULAR WEDGES

Let us finally consider a cylindrical current shell similar to that of Fig. 7(a), but let us assume that it includes four angular wedges dividing each shell quadrant into two current blocks as represented in Fig. 9. The four wedges are assumed to extend between the angles $\theta_2$ and $\theta_1$, where $\theta_2 \leq \theta_1 \leq \theta_0$, in the top right quadrant, ($\pi-\theta_1$) and ($\pi-\theta_2$) in the top left quadrant, ($\pi+\theta_2$) and ($\pi+\theta_1$) in the bottom left quadrant and ($-\theta_1$) and ($-\theta_2$) in the bottom right quadrant. It is straightforward to show that the magnetic flux density produced by this current distribution is again given by Eq. (22) with

$$B_1 = \frac{2\mu_0 J}{\pi}(R_o - R_i)\left[\sin\theta_0 - \sin\theta_1 + \sin\theta_2\right] \tag{33a}$$

and

$$B_{2k+1} = \frac{2\mu_0 J}{\pi(2k+1)(2k-1)}\left(\frac{1}{R_i^{2k-1}} - \frac{1}{R_o^{2k-1}}\right)\left\{\sin\left[(2k+1)\theta_0\right]-\sin\left[(2k+1)\theta_1\right]+\sin\left[(2k+1)\theta_2\right]\right\}$$

$$\text{for } k,\ k \geq 1 \tag{33b}$$

We have seen that in the case of a cylindrical shell with a dipole symmetry and no angular wedge, the sextupole field coefficient, $B_3$, could be set to zero by choosing a pole angle, $\theta_0$, such that: $\sin(3\theta_0) = 0$. This gave: $\theta_0 = 60°$. The main interest of angular wedges is that they provide additional free parameters to set to zero other high order, allowed multipole

field coefficients. For instance, in the case of a cylindrical shell with a dipole symmetry and one angular wedge per quadrant, the angles $\theta_0, \theta_1$ and $\theta_2$ can be chosen to have simultaneously: $B_3 = B_5 = B_7 = 0$. This yields the following system of three equations and three unknowns

$$\sin(3\theta_0) - \sin(3\theta_1) + \sin(3\theta_2) = 0 \tag{34a}$$

$$\sin(5\theta_0) - \sin(5\theta_1) + \sin(5\theta_2) = 0 \tag{34b}$$

and

$$\sin(7\theta_0) - \sin(7\theta_1) + \sin(7\theta_2) = 0 \tag{34c}$$

The solutions of the above system are: $\theta_0 \approx 67.2753°$, $\theta_1 \approx 52.1526°$ and $\theta_2 \approx 43.1791°$. Implementing a second wedge per quadrant (which divides each quadrant into three current blocks) provides two additional parameters which can be determine to obtain: $B_3 = B_5 = B_7 = B_9 = B_{11} = 0$. And so on. In theory, $N$ wedges allow to set to zero up to $(N+1)$ allowed multipole field coefficients. Note that the wedges introduce a spacing in the current distribution which, on a circle of radius, $R$, where $R$, $R_i \leq R \leq R_o$, tends towards the ideal $\cos\theta$ current sheet distribution that was shown to produce a pure dipole field.

In a similar fashion, angular wedges can be implemented into cylindrical current shells having a quadrupole symmetry. In the case of one angular wedge per octant, dividing each octant into two current blocks, the angles $\theta_0$, $\theta_1$ and $\theta_2$ can be chosen to get simultaneously: $B_6 = B_{10} = B_{14} = 0$. This yields the system of three equations and three unknowns

$$\sin(6\theta_0) - \sin(6\theta_1) + \sin(6\theta_2) = 0 \tag{35a}$$

$$\sin(10\theta_0) - \sin(10\theta_1) + \sin(10\theta_2) = 0 \tag{35b}$$

and

$$\sin(14\theta_0) - \sin(14\theta_1) + \sin(14\theta_2) = 0 \tag{35c}$$

The solutions of the system of Eqs. (35) are one half of the solutions of the system of Eqs. (34).

## 4.2 TWO-DIMENSIONAL GEOMETRY

### 4.2.1 SYMMETRY CONSIDERATIONS

The field computations presented in the previous section have shown that current distributions with the symmetries of Fig. 6(a) (*i.e.*, even with respect to the $x$-axis and odd with respect to the $y$-axis) were suitable for generating dipole fields, whereas current distributions with the symmetries of Fig. 6(b) (*i.e.*, even with respect to the $x$- and $y$-axes and odd with respect to the first and second bisectors) were suitable for generating quadrupole fields. Starting from these premises, the coil geometry can be optimized to obtain the required dipole or quadrupole field strength within the desired aperture. In addition, in most accelerator designs, it is required that the high order multipole fields be as small as possible. Hence, the coil geometry optimization is also carried out to minimize the contributions from non-dipole or non-quadrupole terms.

### 4.2.2 CURRENT SHELL APPROXIMATIONS

The coil geometries most commonly used for dipole and quadrupole magnets are approximations of the cylindrical current shells shown in Figs. 7(a) and 7(b). The approximation is obtained by stacking into an arch the slightly keystoned cables described in the section on conductor. The low-field dipole and low-field-gradient quadrupole magnets for RHIC rely on a single coil layer, while Tevatron, HERA, UNK, SSC and LHC magnets rely on two coil layers whose field contributions add up. The high-field LBNL dipole magnet model D20 counts four layers. All magnet coil designs, but that for the Tevatron, include copper wedges which are introduced between some of the coil turns to separate the conductors into blocks. As explained in the previous section, the blocks (or wedges) angles are tuned to eliminate high order multipole field coefficients and approach the ideal $\cos\theta$ and $\cos 2\theta$ current distributions [90]. By analogy, such coil geometries are referred to as $cos\theta$ and $cos2\theta$ designs. They are very compact and make the most effective use of conductors by bringing them close to the useful aperture.

In the case of Tevatron, HERA and UNK magnets, the cable keystone angle is large enough to allow the formation of an arch with the desired aperture. Furthermore, each coil turn lies along a radius vector pointing toward the aperture's center. In the case of SSC and LHC magnets, the coil aperture is reduced to minimize the required volume of superconductor. This results in a keystone angle requirement deemed unacceptable from the point of view of cabling degradation. Hence, in these magnets, the cables are not sufficiently keystoned to assume an arch shape and the wedges between conductor blocks must be made asymmetrical to

compensate for this lack [91]. Also, the coil turns end up being non-radial, as illustrated in Fig. 10, which shows the conductor distribution in a quadrant of a 50-mm-aperture SSC dipole magnet coil (the vectors represent the components of the Lorentz force discussed in the section on mechanical design).

Note that the magnetic flux density produced by the coil of Fig. 10 can be accurately computed by dividing each turn into two rows of elementary current lines parallel to the $z$-axis and approximately equal in number to the number of cable strands [p. 226 of Reference 92].

### 4.2.3 Iron Yoke Contribution

The coils of particle accelerator magnets are usually surrounded by a circular iron yoke, which provides a return path for the magnetic flux while enhancing the central field or field gradient. Eq. (32) shows that the smaller $R_y$, the larger the field enhancement. However, there are two limitations on how close the iron can be brought to the coils: (1) room must be left for the support structure, and (2) iron saturates for fields above 2 T, resulting in undesirable distortions (see section on field quality).

As already mentioned, the Tevatron magnets use a warm iron yoke (*i.e.*, placed outside the helium containment and vacuum vessel), but starting with HERA, the iron yoke is included within the magnet cold mass. For SSC dipole magnets, the field enhancement due to the yoke is of the order of 20%. In LHC magnets, two coil assemblies (powered with opposite polarity) are placed within a common iron yoke. This twin-aperture design results in left/right asymmetries in the yoke around each coil assembly taken individually. These asymmetries must be taken into account when calculating field quality.

### 4.2.4 Operating Current Margin

Eqs. 28(a) and 29(a) show that to achieve high fields and high field gradients, it is desirable to maximize the overall current density in the magnet coil. This can be done by three means: (1) maximizing the superconductor performance, (2) minimizing the copper-to-superconductor ratio in the cable strands and (3) minimizing the turn-to-turn insulation thickness. As explained in other sections, there are lower bounds on the values of copper-to-superconductor ratio and insulation thickness in order to limit conductor heating in case of a quench and to ensure proper electrical insulation. As for the superconductor, the upper limit is the critical current density at the operating temperature and magnetic flux density.

The magnetic flux density to which the conductor is exposed is non-uniform over the magnet coil, but the maximum current-carrying capability of the conductor is determined by the section where the magnetic flux density is the highest. In most cases, this corresponds to the pole turn of the innermost coil layer. Let $B_p = f(I)$ designate the peak magnetic flux density on the coil as a function of supplied current, $I$, and let $I_C = f(B,T_0)$ designate the supposedly known cable critical current as a function of applied magnetic flux density, $B$, at the operating temperature, $T_0$. The intersection between these two curves determines the maximum quench current of the magnet at $T_0$, $I_{qm}(T_0)$.

In practice, magnets must be operated below $I_{qm}$ so as to ensure that the entire coil is in the superconducting state and as to limit the risks of quenching. Let $I_{op}$ designate the operating current. Then, the operating current margin of the magnet, $m_I$, is defined as

$$m_I(T_0) = 1 - \frac{I_{op}}{I_{qm}(T_0)} \tag{36}$$

The excellent quench performance of the HERA magnets [14] suggests that the current margin can be set to as little as 10%, but it is safer to aim for 20%. In comparison to other superconducting magnets, such as solenoids for magnetic resonance imaging, a current margin of 10 to 20% is quite small. This implies that accelerator magnets are operated very close to the superconductor critical surface and are very sensitive to any kind of disturbances that may cause the magnet to cross the critical surface and lead to a quench.

### 4.2.5 CONDUCTOR GRADING

A particularity of two-layer, $\cos\theta$ dipole magnet coil designs is that the peak magnetic flux density in the outermost layer is quite a bit lower than in the innermost layer. Hence, when using the same cable and current for both layers, the outer layer is operated with a much higher current margin than the inner layer, which can be considered as a waste of costly superconductor. The conductor used for the outer layers of SSC and LHC dipole magnet coils is smaller than the conductor used for the inner layers. This results in a higher overall current density in the outer layer and reduces the difference in current margins. Such action is referred to as conductor *grading*. The main disadvantage of grading is that it requires splices between the cables of the two layers, which, of course, are connected electrically in series (and require only one power supply).

It should be noted that for two-layer, $\cos 2\theta$ quadrupole magnet coil designs, the peak magnetic flux density is almost the same for the two layers and that there is no point in conductor grading.

### 4.2.6 LIMITS OF COS$\Theta$ COIL DESIGN

The cos$\theta$ coil design has been very successful until now, with a record dipole field of 13.5 T reached by the LBNL short dipole magnet model D20 (using $Nb_3Sn$ cables at 1.8 K). However, it has two main drawbacks: (1) the coil ends are difficult to make (see the section on coil ends), and (2) due to the Lorentz force distribution, there is a stress accumulation in the azimuthal direction which results in high transverse pressures on the midplane conductors of the coil assemblies (see Fig. 10). For very high field magnets, requiring the use of A15 (or even possibly HTS) superconductors, which are strain sensitive, these high transverse pressures can result in significant critical current degradation [84,85].

Alternative coil designs are being investigated which may allow a better management of the Lorentz stress within the magnet coil. As an illustration, Fig. (11) presents a conceptual *block* or *window-frame* design developed at BNL for a twin-aperture dipole magnet relying only on simple, *racetrack* coils [93]. Note, however, that such designs make less effective use of superconductor.

## 4.3 COIL END DESIGN

As mentioned above, one of the main difficulties of cos$\theta$ and cos2$\theta$ designs is the realization of coil ends. In the coil straight section, the conductors run parallel to the magnet axis, but, in the ends, the conductors must be bent sharply to make U-turns over the beam tube inserted within the magnet coil assembly. This confers to the coil a *saddle shape* as illustrated in Fig. 12.

Sophisticated algorithms have been developed to determine the conductor trajectories minimizing strain energy [94]. These algorithms, which often require winding tests to determine correction factors, are coupled with three-dimensional electromagnetic computations evaluating end field distortions. SSC and LHC magnets use precisely machined end spacers, designed by the optimization programs, which are positioned between conductor blocks [95]. In addition, the iron yoke does not extend over the coil ends to reduce the magnetic flux density on the conductors and ensure that the peak magnetic flux density is located in the coil straight section where the conductors can be better supported.

## 4.4 SAGITTA

To limit the number of coil ends and of magnet interconnects around the accelerator ring, the arc dipole and quadrupole magnets are made as long as possible. As we have seen, the circulation of a charged beam in a dipole magnet, of magnetic length, $l_d$, results in an angular deflection, $\phi$, given by Eq. (5). Consequently, the long dipole magnets used in large accelerator rings must be bent slightly to accompany the particle trajectory. This bending, which is implemented in the $(\vec{x}, \vec{z})$ plane, is referred to as *sagitta.*

# 5 FIELD QUALITY

## 5.1 MULTIPOLE EXPANSION

Except near the short coil ends, the magnetic flux density produced in the bore of a particle accelerator magnet can be considered as two-dimensional. In practice, the power series expansion of Eq. (19) is usually rewritten under the more convenient form

$$B_y + iB_x = B_{ref}\, 10^{-4} \sum_{n=1}^{+\infty} (b_n + i\, a_n) \left(\frac{\mathbf{z}}{R_{ref}}\right)^{n-1} \quad \text{for } \mathbf{z} = x + iy,\ |\mathbf{z}| < R_i \tag{37}$$

where $B_x$ and $B_y$ are the $x$- and $y$-components of the magnetic flux density, $R_{ref}$ is a reference radius representative of maximum beam size ($R_{ref}$ was 10 mm for SSC and is now 17 mm for LHC), $B_{ref}$ is the absolute value of the dipole or quadrupole component at $R_{ref}$, $a_n$ and $b_n$ are the dimensionless skew and normal $2n$-pole coefficients expressed in so-called *units* and $R_i$ is the coil inner radius. Note the presence of the $10^{-4}$ scale factor.

Given the symmetries of current distributions in magnet coil assemblies, and as explained in the previous section, only selected normal multipole coefficients are expected to be non-zero. These allowed multipole coefficients can be tuned up by iterating on the electromagnetic design. In practice, however, non-uniformities in material properties and manufacturing errors result in symmetry violations which produce *un-allowed* multipole coefficients. For instance, a top/bottom asymmetry in a dipole magnet produces a non-zero skew quadrupole coefficient ($a_2$), while a left/right asymmetry produces a non-zero normal quadrupole coefficient ($b_2$). These unwanted coefficients can only be eliminated by improving material selection, tooling and assembly procedures.

## 5.2 FIELD QUALITY REQUIREMENTS

From the accelerator point of view, the beam optics is primarily governed by integrated field effects over the magnet ring. The main field quality requirements are: (1) suitable dipole field integral and small dipole field angle variations (the former to ensure that the integrated bending angle over the magnet ring is ($2\pi$) and the latter to ensure that the particle trajectory is planar), (2) accurate quadrupole alignment and suitable quadrupole field integral (the former to avoid coupling of particle motions along the $x$- and $y$-axes and the latter to ensure proper focusing), and (3) small high order multipole coefficients (to ensure large beam dynamic aperture). In the case of high order multipole coefficients, it is customary to specify tables of mean values and standard deviations over the entire magnet population [96]. The tables of

mean values are referred to as *systematic* multipole specifications whereas those of standard deviations are referred to as *random* multipole specifications. The specified values are all expressed at the reference radius, $R_{ref}$.

In large machines such as SSC or LHC, the dipole and quadrupole field integrals must be controlled with a relative precision of the order of $10^{-3}$. The variations in dipole field angles must be kept within a few milli-radians and the tolerance on quadrupole alignment is of the order of 0.1 mm. Systematic and random multipole specifications are given up to the 18th or 20th pole and get tighter with increasing pole order. For SSC magnets at 10 mm, the specifications went from a few tenths of a unit for low order coefficients to a few thousandths of a unit for higher order coefficients.

## 5.3 GEOMETRIC ERRORS

### 5.3.1 TYPES OF GEOMETRIC ERRORS

The specifications on multipole coefficients require that the individual conductors and the yoke surrounding the coil assembly be positioned with a very good accuracy (typically: a few hundredths of a millimeter in the two-dimensional cross-section). Improper positioning results in geometric errors that distort the central field and produce unwanted coefficients.

The geometric errors can be classified in at least five categories: (1) errors in coil inner and outer radii and in yoke inner radius, (2) errors in coil pole angle, wedge angle and conductor angular distribution, (3) symmetry violations in coil assembly, (4) centering errors with respect to the iron yoke and (5) residual twist of magnet assembly.

### 5.3.2 EFFECTS OF AZIMUTHAL COIL SIZE MISMATCH

A common cause of geometric error is a mismatch between the azimuthal sizes of the various coils constituting a coil assembly. Such mismatch results in displacements of the coil assembly symmetry planes which produce non-zero, low order un-allowed multipole coefficients [97]. For instance, a mismatch between the azimuthal sizes of the top and bottom coils used in a dipole magnet coil assembly causes an upward or downward displacement of the coil parting planes which produces a non-zero skew quadrupole coefficient ($a_2$). Similarly, a systematic mismatch between the left and right sides of the coils used in a dipole magnet coil assembly causes a rotation of the coil parting planes which produces a non-zero skew sextupole coefficient ($a_3$). A systematic $a_2$ can be limited by randomly mixing coil production, whereas the occurrence of a systematic $a_3$ can only be avoided by correcting tooling.

## 5.4 IRON SATURATION

When the field in the iron yoke is less than 2 T, the relative magnetic permeability of the yoke can be considered as very large and uniform, and the iron contribution to the central field increases linearly as a function of transport current in the magnet coil. For fields above 2 T, parts of the iron start to saturate and their relative magnetic permeability drops. As a result, the iron contribution becomes a less-than-linear function of transport current. This relative decrease in iron contribution appears as a sag in the magnet transfer function [91]. (The transfer function is defined as the ratio of $B_{ref}$ to the transport current). The transfer function sag can exceed a few percent in dipole magnets but is usually negligible in quadrupole magnets.

In the case of a single aperture magnet with a symmetrical iron yoke, the saturation first occurs in the pole areas producing a positive shift in normal sextupole coefficient ($b_3$). At higher currents, the saturation reaches the midplane areas, producing a negative shift in $b_3$ which partially compensates for the effects of pole saturation. The midplane saturation can be forced to occur sooner by punching notches (*i.e.*, removing matter) at appropriate locations in the yoke. As an illustration, Fig. 13 presents measurements of $b_3$ as a function of current in the central part of a SSC dipole magnet prototype. The measurements above 3 kA clearly show the effect of pole saturation at high currents (the origin of the hysteresis is explained in the next section).

In the case of a twin-aperture dipole, the central part of the yoke saturates before the outer parts, resulting in left/right asymmetries in the yoke contributions to each aperture which affect the normal quadrupole coefficient ($b_2$). The saturation effects in $b_2$ are of opposite sign in the two apertures.

In any case, the iron contribution depends on the packing factor of the yoke laminations which must be tightly controlled over the magnet length. Also, the iron yoke must be carefully aligned to limit magnet assembly twist.

## 5.5 SUPERCONDUCTOR MAGNETIZATION

### 5.5.1 CRITICAL STATE MODEL

According to the so-called *critical state model*, bipolar magnetization currents are induced at the periphery of the superconducting filaments in the cable strands each time the field to which the filaments are exposed is varied [98]. The magnetization currents distribute themselves with a density equal to the superconductor critical current density at the given

temperature and field, $J_C$, in order to screen the filament cores from the applied field change. Unlike regular eddy currents, the magnetization currents do not depend on the rate of field variations. Also, because they can flow with zero resistance, they do not decay as soon as the field ramp is stopped. They are called *persistent magnetization currents.*

### 5.5.2 EFFECTS OF SUPERCONDUCTOR MAGNETIZATION

When an accelerator magnet is cycled in current, the bipolar shells of magnetization currents induced in the filaments behave as small magnetic moments which contribute to –and distort– the central field. The magnetic moments depend on $J_C$ and are proportional to filament diameter. Their distribution follows the symmetries of the transport-current field (*i.e.*, the field produced by the transport current in the magnet coil) and, if the superconductor properties are uniform, only the allowed multipole coefficients are affected. Computer models have been developed which can accurately predict the field distortions resulting from superconductor magnetization [99].

The field distortions are the most significant at low transport current, where the transport-current field is low and $J_C$ is large. They are progressively overcome as the transport-current field increases and $J_C$ diminishes and become negligible at high transport current. They change sign and regain influence as the transport current is ramped down. As a result, the allowed multipole coefficients exhibit sizable hystereses as a function of transport current, which depend on magnet excitation history. This is illustrated in Fig. 13 which shows measurements of $b_3$ as a function of current in the central part of a SSC dipole magnet. In Fig. 13, the magnetization effects can clearly be seen at currents below 3 kA (as explained in the previous section, the distortions at high field result from iron yoke saturation).

The field distortions resulting from superconductor magnetization are one of the major drawbacks of using superconducting magnets in a particle accelerator. They can be reduced by reducing filament size (typically, to 5 μm for SSC and LHC strands), but they cannot be eliminated. The powering cycle of the magnets must be adapted to avoid brutal jumps between the two branches of the multipole coefficient hystereses while the beam circulates. Also, elaborate beam optics correction schemes must be developed, which can include superconducting, high-order multipole magnets [chapter 9 of Reference 4].

### 5.5.3 TIME DECAY

In addition, the effects of superconductor magnetization are not indefinitely persistent, but exhibit a slow time decay, which, at low transport current, can result in significant drifts of

the allowed multipole coefficients [100,101]. These drifts are particularly disturbing during the injection phase of machine operation, where the magnet current is maintained at a constant and low level for some period of time [102,103]. Also, they complicate the early stages of acceleration, for, as the current is increased at the end of injection, the drifting multipoles snap-back rapidly to values on the hysteresis curves [104]. Part of the observed time decay can be attributed to flux creep in the superconductor [105], but flux creep cannot account for the large drifts observed after a high current cycle [101]. The nature of the other mechanisms that may be involved is not well understood.

## 5.6 COUPLING CURRENTS

As described in the conductor section, accelerator magnet coils are wound from Rutherford-type cables, which consist of a few tens of strands twisted together and shaped into a flat, two-layer, slightly keystoned cable. The cable mid-thickness is smaller than twice the strand diameter, which results in strand deformation and large contact surfaces at the crossovers between the strands of the two layers. Furthermore, and as explained in the mechanical design section, the coils are pre-compressed azimuthally during magnet assembly. Large pressures that keep the strands firmly in contact are thus applied perpendicularly to the cable. The large contact surfaces and the high pressures can result in low contact resistances at the strand crossovers.

In the steady state, the transport current flows in the superconducting filaments which offer no resistance. When the cable is subjected to a transverse varying field, the network of low interstrand resistances allows the formation of current loops which are superimposed on the transport current. The loop currents, referred to as *interstrand coupling currents*, circulate along the superconducting filaments and cross-over from strand to strand through the interstrand resistances. Unlike persistent magnetization currents, the interstrand coupling currents are directly proportional to the rate of field variations and they start to decay as soon as the field ramp is stopped.

Interstrand coupling currents have three main effects on magnet performance [92]: 1) heat dissipation (when crossing the interstrand resistances), 2) field distortions, and 3) quench current degradation (for they are superimposed on the transport current). The field distortions issue is the most critical for accelerator magnet applications [106].

The coupling current contribution to the central field does not depend on transport current and increases linearly as a function of current ramp rate. If the interstrand resistance is uniform throughout the coil assembly, the coupling current distribution follows the symmetries

of the transport-current field and only the allowed multipole field coefficients are affected. In practice, however, there can be large coil-to-coil differences as well as large non-uniformities within the coils themselves which result in sizable effects in the un-allowed multipole coefficients. This is illustrated in Figs. 14(a) and 14(b) which present plots of the skew and normal sextupole field coefficients ($A_3$ and $B_3$) as functions of current, measured at various ramp rates in the central part of a SSC dipole magnet prototype. (Note that the transport-current contribution has been subtracted from the data.) No particular treatment (such as stabrite) was applied to the strands of the cable used in this prototype.

The effects of interstrand coupling currents can be limited by ensuring that the interstrand resistances are not too low. However, and as mentioned in the conductor section, the interstrand resistances should not be too large either to allow some possibility of current redistribution among cable strands.

## 5.7 LONGITUDINAL PERIODICITY

When measuring the field with fine spatial resolution along the axis of an accelerator magnet, all multipole coefficients appear to exhibit periodic oscillations [107,108]. The amplitude of the oscillations varies as a function of space, transport current, excitation history and time, but the wavelength is always approximately equal to the twist pitch length of the cable used in the innermost coil layer.

The longitudinal periodic oscillations are believed to result from imbalances in the current distribution among cable strands. The current imbalances may have at least three origins: (1) non-uniformities in the properties of cable strands, (2) non-uniformities in the solder joints connecting the coils in series to the current leads and (3) large and long-lasting interstrand coupling current loops superimposed on the transport current [109]. Such current loops could be induced by spatial variations in the time-derivative of the field to which the cable is exposed as it turns around the coil ends or exits towards the current leads [110–112].

The oscillation wavelength is too short to affect beam optics but may be an issue for magnetic measurements. It is recommended that the measurements be averaged over an integer number of cable pitch lengths. Also, the slow decay of the large interstrand coupling current loops associated with these periodic oscillations may contribute to the drifts of the allowed multipole coefficients observed at low and constant transport current (see section on superconductor magnetization) [113].

# 6 MECHANICAL DESIGN

## 6.1 SUPPORT AGAINST THE LORENTZ FORCE

### 6.1.1 COMPONENTS OF THE LORENTZ FORCE

The high currents and fields in an accelerator magnet coil produce a large Lorentz force on the conductors. In a dipole coil, the Lorentz force has three main components which are represented in Fig. 10 [91,114]: (1) an azimuthal component which tends to squeeze the coil towards the coil assembly midplane (which, in the coordinate system defined previously, corresponds to the horizontal $(\vec{x}, \vec{z})$ plane), (2) a radial component which tends to bend the coil outwardly, with a maximum displacement at the coil assembly midplane (along the horizontal $x$-axis), and (3) an axial component, arising from the solenoidal field produced by the conductor turnaround at the coil ends and which tends to stretch the coil outwardly (along the $z$-axis).

### 6.1.2 STABILITY AGAINST MECHANICAL DISTURBANCES

Because accelerator magnets are operated close to the critical current limit of their cables, their minimum quench energy, referred to as MQE, and defined as the minimum energy deposition needed to trigger a quench, is very small. As a matter of fact, the MQE of accelerator magnets is of the same order of magnitude as the electromagnetic work produced by minute wire motions in the coil [115]. If the motions are purely elastic, no heat is dissipated and the coil remains superconducting, but if the motions are frictional, the associated heat dissipation may be sufficient to initiate a quench. This leaves two possibilities: either to prevent wire or coil motion by providing a rigid support against the various components of the Lorentz force or to reduce to a minimum the friction coefficients between potentially moving parts of magnet assembly.

### 6.1.3 CONCEPTUAL DESIGN

The mechanical design concepts used in present accelerator magnets are more or less the same and were developed at the time of the Tevatron [6,7]. In the radial direction: the coils are confined within a rigid cavity defined by laminated collars which are locked around the coils by means of keys or tie rods. In the azimuthal direction: the collars are assembled so as to pre-compress the coils. In the axial direction: the coils either are free to expand or are restrained by means of stiff end-plates.

The use of laminated collars, pioneered at the Tevatron, was a real breakthrough in achieving a rigid mechanical support while keeping tight tolerances over magnet assemblies which are a few meters in length and which must be mass-produced. The laminations are usually stamped by a fine blanking process allowing a dimensional accuracy of the order of one hundredth of a millimeter to be achieved.

## 6.2 AZIMUTHAL PRE-COMPRESSION

### 6.2.1 PREVENTING COLLAR POLE UNLOADING

As described above, the azimuthal component of the Lorentz force tends to squeeze the coil towards the midplane. At high fields, it may happen that the coil pole turns move away from the collar poles, resulting in variations of coil pole angle, which distort the central field, and creating a risk of mechanical disturbances. (The collar poles designate the collar extensions which fill up the empty spaces left by the conductor distribution in the pole areas and the coil pole turns designate the coil turns directly in contact with these extensions.) To prevent conductor displacements, the collars are assembled and locked around the coils so as to apply an azimuthal pre-compression. The pre-compression is applied at room temperature and must be sufficient to ensure that, after cooldown and energization, there is still contact between coil pole turns and collar poles.

### 6.2.2 PRE-COMPRESSION REQUIREMENT

To determine the proper level of room temperature azimuthal pre-compression, at least three effects must be taken into account: (1) stress relaxation and insulation creep following the collaring operation, (2) thermal shrinkage differentials between coil and collars during cooldown (if any) and (3) stress redistribution due to the azimuthal component of the Lorentz force. In addition, the collaring procedure must be optimized to ensure that the peak pressure seen by the coils during the operation (which may be significantly higher than the residual pre-compression) does not overstress the insulation [p. 1326 of Reference 114].

The pre-compression loss during cooldown, $\Delta\sigma$, can be estimated from

$$\Delta\sigma \approx E_{coil}\,(\alpha_{coil} - \alpha_{collar}) \tag{38}$$

where $E_{coil}$ is the coil Young's modulus in the azimuthal direction, and $\alpha_{coil}$ and $\alpha_{collar}$ are the thermal expansion coefficients of the coil (in the azimuthal direction) and of the collars,

integrated between room and operating temperatures. Note that Eq. (38) is derived with the assumptions that $E_{coil}$ does not depend on temperature and that the collars are infinitely rigid.

### 6.2.3 CHOICE OF COLLAR MATERIAL

To limit cooldown loss, it is preferable to use for the collars a material whose integrated thermal expansion coefficient matches more or less that of the coil. For NbTi coils with polyimide/glass or all-polyimide insulation, this suggests aluminum alloy (see Table 2). However, and as will be described in the next section, it is also desirable that the collars be as rigid as possible or have an integrated thermal expansion coefficient approaching that of the low carbon steel used for the yoke. This favors austenitic stainless steel, which has a lower integrated thermal expansion coefficient and whose Young's modulus is 195 GPa at room temperature and 203 GPa at 4.2 K, compared to 72 GPa at room temperature and 80 GPa at 4.2 K for aluminum alloy.

When assessing the respective merits of austenitic stainless steel and aluminum alloy, it should be noted that austenitic stainless steel presents a better resistance to stress cycling at low temperature [116], but that it has a higher density (7800 kg/m$^3$ compared to 2800 kg/m$^3$ for aluminum alloy) and is more expensive.

There is no ideal choice between stainless steel and aluminum alloy and magnets with both types of collar materials have been built: HERA dipole magnets and most LHC dipole magnet prototypes use aluminum alloy collars whereas Tevatron dipole magnets and most SSC dipole magnet prototypes rely on stainless steel collars. In any case, and whichever collar material is chosen, a thorough mechanical analysis of the structure under the various loading conditions is required.

## 6.3 RADIAL SUPPORT

### 6.3.1 LIMITING RADIAL DEFLECTIONS

As described above, the radial component of the Lorentz force tends to bend the coil outwardly, with a maximum displacement at the coil assembly midplane. At high fields, this bending results in shear stresses between coil turns and in an ovalization of the coil assembly (along the horizontal $x$-axis for a dipole magnet), which generates field distortions. To prevent displacements or deformations, the radial deflections of the coil assembly must be limited to, typically, less than 0.05 mm.

### 6.3.2 SEEKING YOKE SUPPORT

The main support against the radial component of the Lorentz force is provided by the collars, whose stiffness and radial width must be optimized to limit collared-coil assembly deflections. However, in the magnetic design of high field magnets, the field enhancement provided by the iron yoke is maximized by bringing it as close as possible to the coil. This reduces the space left for the collars, whose rigidity then becomes insufficient to hold the Lorentz force, and the yoke and helium containment shell must also be used as part of the coil support system.

The mechanical design of magnets where the yoke is needed to support the collared-coil assembly is complicated by the fact that the collar material (stainless steel or aluminum) shrinks more during cooldown than the low carbon steel used for the yoke (see Table 2). This thermal shrinkage differential must be compensated to ensure that, when the magnet is cold and energized, there is a proper contact between the collared-coil assembly and the yoke along the axis of maximum potential displacements. Such contact limits the deformations of the collared-coil assembly and allows a partial transfer (up to 50% in some LHC dipole magnet prototypes) of the radial component of the Lorentz force to the yoke and the shell.

The aforementioned thermal shrinkage differential, $\Delta r$, can be estimated as

$$\Delta r = R_{\text{collar}} (\alpha_{\text{collar}} - \alpha_{\text{yoke}}) \tag{39}$$

where $R_{\text{collar}}$ is the collar outer radius and $\alpha_{\text{yoke}}$ is the thermal expansion coefficient of the yoke, integrated between room and operating temperatures.

To limit contact loss due to thermal shrinkage differential it is preferable to use for the collars a material whose integrated thermal expansion coefficient approaches that of low carbon steel. This suggests the use of austenitic stainless steel (see Table 2). However, and as was described in the section on choice of collar material, it is also desirable to limit the cooldown loss of coil pre-compression, which favors the use of aluminum alloy.

### 6.3.3 MECHANICAL DESIGN WITH FULLY MATED YOKE ASSEMBLY

To facilitate assembly, the yoke of dipole magnets is usually split into two halves which are mounted around the collared-coil assembly. The shell, which is also made up of two halves, is then placed around the yoke and welded. If the thermal shrinkage differential between collar and yoke is not too large (as in the case of stainless steel collars), it can be

compensated for by designing and assembling the structure so that the two yoke halves apply a compressive load over selected areas of the collared-coil assembly. This compressive load is obtained by introducing a shrinkage allowance into the geometry of either the collars or the yoke and by welding the shell so as to press radially onto the two yoke halves and as to force them to mate at room temperature. During cooldown, the collared-coil assembly shrinks away from the two yoke halves which remain fully mated. This results in a progressive decrease of the compressive load exerted by the yoke but a suitable contact can be maintained over the designated areas of the collared-coil assembly.

In practice, the compressive load provided by the yoke is directed along a given axis. The choice of the axis drives the choice of yoke split orientation. The SSC dipole magnet prototypes built at BNL use a horizontally-split yoke with a yoke/collar compressive load directed along the vertical $y$-axis as shown in Fig. 15(a), while the SSC dipole magnet prototypes built at FNAL use a vertically-split yoke with a yoke/collar compressive load directed along the horizontal $x$-axis as shown in Fig. 15(b) [20]. Both types of magnets performed very well.

### 6.3.4 Mechanical Design with Yoke Midplane Gap at Room Temperature

For large thermal shrinkage differentials (as in the case of aluminum collars), the yoke/collar compressive load required at room temperature for a full compensation would overstress the collared-coil assembly and a more sophisticated mechanical design must be used. The twin-aperture LHC dipole magnet prototypes with aluminum collars rely on a two-piece, vertically-split yoke with an open gap at room temperature and a welded outer shell made of a material (stainless steel or aluminum) that shrinks more during cooldown than the low carbon steel yoke [117].

In these magnets, the yoke is designed so that, when placed around the collared-coil assembly at room temperature with no pressure applied to it, there remains an opening between the two yoke halves of the order of the expected thermal shrinkage differential. The yoke midplane gap is then closed in two stages: (1) during shell welding, as a result of the compressive load arising from weld shrinkage and (2) during cooldown, as a result of the compressive load arising from thermal shrinkage differential between yoke and shell. The initial gap closure during shell welding is limited to avoid overstressing the collared-coil assembly. The closure is completed during cooldown thanks to the radial pressure exerted by the shell which forces the two yoke halves to follow the shrinkage of the collared-coil assembly and to maintain a contact along the horizontal $x$-axis. The yoke midplane gap must be fully

closed at the end of cooldown to ensure that the structure is very rigid and to avoid any risk of oscillation during energization.

A crucial issue in such a design is the ability of performing the shell welding operation in a reproducible way during mass production while achieving the desired yoke midplane gap value at room temperature and keeping a tight tolerance on this value (of the order of 0.1 mm). As we have seen, a gap too close may result in coil overstressing at room temperature whereas a gap too open may result in contact loss during cooldown.

In some LHC prototypes, the yoke midplane gap is controlled by means of aluminum spacers located between the two yoke halves [118]. The spacers are dimensioned to have a spring rate similar to that of the collared-coil assembly and they prevent the gap from closing at room temperature. During cooldown, however, they shrink more than the yoke and cease to be effective. The concept of aluminum control gap spacer was first thought of at SSC [119] and was first tried on a short dipole magnet model (using NbTi cables) built at LBNL. The LBNL model reached 10.06 T at 1.8 K [120].

### 6.3.5 RHIC MAGNETS

In RHIC magnets, collar and yoke designs are altogether simplified by replacing the collars by reinforced plastic spacers and by using directly the yoke to pre-compress the one-layer coils [29]. It remains to be seen if this structure could be scaled-up to higher field magnets.

## 6.4 END SUPPORT

As described above, the axial component of the Lorentz force tends to stretch the coil outwardly along the $z$-axis. In magnets where the yoke is not needed to support the collared-coil assembly, a clearance can be left between the two. If the axial stresses resulting from the Lorentz force do not exceed the yield stress of the coil, it is possible to let the collared-coil expand freely within the iron yoke. This is the case of the quadrupole magnets designed at CEA/Saclay for HERA, SSC and LHC [36]. However, in magnets where there is contact between collar and yoke, it is essential to prevent stick/slip motions of the laminated collars against the laminated yoke and to provide a stiff support against the axial component of the Lorentz force [114,121]. The ends of SSC and LHC dipole magnet coils are contained by thick stainless steel end plates welded to the shell.

# 7 MAGNET COOLING

## 7.1 SUPERCONDUCTOR CRITICAL TEMPERATURE

The superconducting state only exists at temperatures below the so-called *critical temperature*, $T_C$. For NbTi, $T_C$ can be estimated as a function of applied magnetic flux density, $B$, using [69]

$$T_C(B) = T_{C0}\left(1 - \frac{B}{B_{C20}}\right)^{1.7} \tag{40}$$

where $T_{C0}$ is the critical temperature at zero field (about 9.2 K) and $B_{C20}$ is the upper critical magnetic flux density at zero temperature (about 14.5 T).

## 7.2 MAGNET CRITICAL TEMPERATURE AT A GIVEN CURRENT

Let us consider a magnet coil initially in the superconducting state at an uniform temperature, $T_0$, and carrying a constant transport current, $I$, such that

$$I < I_{qm}(T_0) \tag{41}$$

where $I_{qm}$ is the maximum quench current at $T_0$ defined in the section on operating current margin.

Let us further assume that the magnet temperature is raised uniformly from $T_0$ to $(T_0 + \Delta T)$. The temperature increase results in a decrease of the superconductor critical current density and in a reduction of $I_{qm}$. The magnet coil remains in the superconducting state as long as

$$I \leq I_{qm}(T_0 + \Delta T) \tag{42}$$

It follows that, for a given value of $I$, the minimum temperature increase, $\Delta T_{qm}$, that is likely to initiate a quench is determined by

$$I = I_{qm}(T_0 + \Delta T_{qm}) \tag{43}$$

The magnet *critical temperature at current I*, $T_{CI}$, is defined as

$$T_{CI}(I) = T_0 + \Delta T_{qm}(I) \tag{44}$$

Replacing $I_{qm}$ by its definition shows that $T_{CI}$ is the solution of the implicit equation

$$I = I_C(T_{CI}, B_p(I)) \tag{45}$$

where $I_C(T,B)$ is the supposedly known parametrization of the cable critical current as a function of temperature, $T$, and magnetic flux density, and $B_p(I)$ is the computed peak magnetic flux density on the magnet coil. Note that, unlike $T_C$, which is an intrinsic characteristic of the superconducting material, $T_{CI}$ depends on cable and magnet designs.

## 7.3 TEMPERATURE MARGIN AND ENTHALPY MARGIN

Let us now consider a magnet that is designed to be operated at a current, $I_{op}$. To reach the superconducting state, the magnet coil must of course be cooled down to a temperature, $T_0$, that is lower than the critical temperature at $I_{op}$, $T_{CI}(I_{op})$.

The operating temperature margin, $\Delta T_{op}$, is defined as

$$\Delta T_{op} = T_{CI}(I_{op}) - T_0 = \Delta T_{qm}(I_{op}) \tag{46}$$

and the operating enthalpy margin, $\Delta H_{op}$, is defined as

$$\Delta H_{op} = \int_{T_0}^{T_{CI}(I_{op})} dT\, C(T) \tag{47}$$

Here $C$ is the specific heat per unit volume of conductor (in J/m$^3$).

In the section on magnetic design, we have seen that to ensure suitable quench performance, the operating current margin should be set to at least 10%. In practice, however, most unwanted quenches occur because of energy depositions which result in local temperature increases (see section on quench performance). Hence, it is more suitable to set a specification on temperature margin. Of course, the larger the temperature margin, the larger the enthalpy margin, and the more stable the magnet operation against thermal disturbances. The SSC dipole magnets were designed to operate at 4.35 K with a temperature margin of about 0.6 K while the LHC dipole magnets are designed to operate at 1.9 K with a temperature margin of about 1.4 K. Assuming that the cables have similar copper-to-superconductor ratios, it can be verified that, due to the fact that the specific heat per unit volume of conductor is a strongly decreasing function of temperature, these two temperature margins correspond to enthalpy margins of the same magnitude.

## 7.4 BOILING AND SUPERCRITICAL HELIUM COOLING

Among the cryogenic fluids, liquid helium, which has a boiling temperature of 4.2 K at 1 atmosphere (1 atmosphere $\approx$ 0.1 MPa), is the most adapted for cooling down superconducting magnets made from NbTi or $Nb_3Sn$ conductors [122]. In the case of accelerator magnets, the coils are fully immersed into liquid helium and the superconducting cable is directly in contact with the coolant which, thereby, participates to the stability against thermal disturbances. The pressure-temperature phase diagram of helium is presented in Fig. 16 [123].

Small superconducting magnet systems usually rely on boiling helium at 1 atmosphere [123]. Boiling helium offers the advantage that, as long as the two phases are present, the temperature is well determined. However, in large scale applications, such as superconducting particle accelerators, the fluid is forced to flow through numerous magnet cryostats and long cryogenic lines, where heat leaks are unavoidable. The heat leaks result in increases in vapor contents and create a risk of gas pocket formation that may block circulation.

The aforementioned difficulty can be circumvented by taking advantage of the fact that helium exhibits a critical point at a temperature of 5.2 K and a pressure of 0.226 MPa (see Fig. 16). For temperatures and pressures beyond the critical point, the liquid and vapor phases become indistinguishable. The single-phase fluid, which is called *supercritical*, can be handled in a large system without risk of forming gas pockets. However, its temperature, unlike that of boiling helium, is not constant and may fluctuate as the fluid circulates and is subjected to heat losses.

The cryogenic systems of Tevatron, HERA, and RHIC, and that designed for SSC, combine single-phase and two-phase helium [123]. In the case of Tevatron and HERA, the inside of the magnet cold masses are cooled by a forced flow of supercritical helium whereas two-phase helium is circulated in a pipe running at the cold mass periphery (around the collared-coil assembly for Tevatron magnets [124,125], in a bypass hole in the iron yoke for HERA magnets [126]). In the case of SSC, it was planned to only circulate supercritical helium through the magnet cold masses, while so-called *re-coolers*, consisting of heat exchangers using two-phase helium as primary fluid, would have been implemented at regular intervals along the cryogenic lines [127,128]. The cryogenic system used for RHIC is inspired from that of SSC. In all these schemes the boiling liquid is used to limit temperature rises in the single-phase fluid.

## 7.5 SUPERFLUID HELIUM COOLING

A particularity of helium is the occurrence of *superfluidity* [122,129]. When cooling down boiling helium at 1 atmosphere, it stays liquid until a temperature of the order of 2.17 K, where there appears a phase transition. For temperatures below 2.17 K (at 1 atmosphere) helium loses its viscosity and becomes a superconductor of heat. This property, unique to helium, is called superfluidity. Superfluidity is very similar to superconductivity, except that, instead of electrical conductibility, it is the thermal conductibility that becomes infinite. The transition temperature between liquid and superfluid phases is referred to as *lambda-temperature*, $T_\lambda$, and depends on pressure.

The LHC magnets are cooled by superfluid helium and their operating temperature is set at 1.9 K [130]. Decreasing the temperature improves the current carrying capability of NbTi dramatically and allows higher fields to be reached. (As we noted in the section on NbTi wires, the curve "critical current density as a function of field" of NbTi is shifted by about +3 T when lowering the temperature from 4.2 K to 1.9 K.) Superfluid helium was first used in a large scale application for Tore Supra, a superconducting tokamak built at CEA/Cadarache (Commissariat à l'Energie Atomique at Cadarache near Aix en Provence in the South of France) and operating reliably since 1988 [131].

## 7.6 MAGNET CRYOSTAT

To maintain magnet cold masses at low temperature it is necessary to limit heat losses. There are three main mechanisms of heat transfer [132]: (1) convection, (2) radiation and (3) conduction. The convection losses are eliminated by mounting the cold masses into cryostats which are evacuated [123,133]. The radiation losses, which scale in proportion with the effective emissivities of the surfaces facing each other and with the fourth power of their temperatures, are reduced by surrounding the cold masses with blankets of multilayer insulation and thermal shields at intermediate temperatures. The main sources of conduction losses are the support posts, the power leads and the cryogenic feedthroughs which are designed to offer large thermal resistances.

# 8 QUENCH PERFORMANCE

## 8.1 WHAT IS A QUENCH?

As we have seen, for a given material, the boundary between the superconducting state and the normal resistive state can be represented by a three-dimensional surface which depends on operating temperature, applied magnetic flux density and transport current density. A magnet is normally operated at conditions corresponding to a volume located beneath the critical surface, where the entire coil is superconducting.

Starting from the operating conditions, let us ramp up the current supplied to a superconducting magnet, or let us assume that, somewhere in the magnet coil, there is an energy deposition which results in a local temperature rise. In ramping up the current (and thus, the magnetic field) or in raising the temperature, we get closer and closer to the critical surface, and soon, we cross it. Crossing the critical surface means that, somewhere in the coil, a small volume of conductor switches to the normal resistive state. When switching to the normal resistive state, the small volume of conductor starts dissipating power by the Joule effect. The dissipated power overheats the small volume, and, by thermal diffusion along the conductor (or by any other mechanism of heat transfer), the region surrounding the small volume. If the Joule heating is large enough (and if the cooling is not too strong), the surrounding region can, in turn, reach the transition temperature, switch to the normal resistive state, and start dissipating power. And so on. Under certain conditions, a self-maintained process can be established — from transition, to power dissipation, to thermal diffusion and then again to transition — in which the *normal zone*, *i.e.*, the zone where the conductors have switched to the normal resistive state, grows irreversibly and *propagates* through the entire coil. This process is called a *quench*.

## 8.2 MAGNET TRAINING AND QUENCH PLATEAU

As explained in the section on operating current margin, the current limit of a superconducting magnet at a given operating temperature is determined by the critical current of its cable and the peak magnetic flux density on the magnet coil. We referred to this limit as the maximum quench current, $I_{qm}$. However, as it is usually estimated from critical current values directly measured on a short sample of cable cut from the cable batch used in winding the magnet coil, it is also referred to as *short sample current limit*, $I_{ss}$. For a given magnet, the values of $I_{qm}$ or $I_{ss}$ can only be raised by decreasing the operating temperature.

When cooling down and energizing a superconducting magnet for the first time, the first quenches usually occur at currents below $I_{qm}$ or $I_{ss}$ [chapter 5 of Reference 60]. In most cases, however, it appears that, upon successive energizations, the quench currents gradually increase. This gradual improvement is called the magnet's *training*. The training often leads to a stable *plateau* corresponding more or less to the expected maximum quench current at the given temperature.

As an illustration, Fig. 17(a) presents a plot of current at quench versus quench number for an early 4-cm aperture, 17-m long SSC dipole prototype (magnet DD0017) [134]. The magnet was first cooled down to a nominal temperature of 4.35 K and ramped up several times to quench. A *ramp to quench* consists of ramping up the magnet current until a quench occurs; the power supply is then switched off and the magnet is discharged. Following the quench, the magnet is cooled down again to 4.35 K, and the test is repeated. In the case of DD0017, the magnet was ramped to quench seven times and then warmed up to room temperature for several days. After this *thermal cycle* to room temperature, it was cooled down again to 4.35 K, and ramped to quench six more times.

The data of Fig. 17(a) shows that, after the first cooldown to 4.4 K, magnet DD0017 exhibited two training quenches and reached a plateau on the third quench (as explained in a later section, the lower currents observed for quenches 6 and 7 are due to slight increases in magnet temperature). It appears also in Fig. 17(a), that, after the second cooldown to 4.4 K, it took again two training quenches to reach the level of plateau quench current previously achieved. This means that, during the thermal cycle to room temperature, magnet DD0017 lost the memory of its initial training and required *re-training*.

## 8.3 ACCURACY OF SHORT SAMPLE CURRENT LIMIT ESTIMATIONS

One question that arises is how reliable are the short sample current limit estimations. As we have seen, these estimations are usually based on critical current measurements on a well cooled short sample which may or may not be representative of the full length of cable in the magnet coil environment. Furthermore, and as explained in the section on transition of multifilamentary wires, the critical current is defined by relying on empirical criterions which may be suited for some applications but may turn out to be inadequate for some other. One way of answering this question is to compare short sample current limit estimations with actual plateau quench currents achieved in real magnets.

Figure 18 presents a summary plot of the highest plateau quench currents reached on selected 5-cm-aperture, 15-m-long SSC dipole magnet prototypes as a function of the estimated

short sample current limits at the given temperatures. (The magnets were usually tested at three nominal temperatures: 4.35 K, 3.8 K and 3.5 K, at which they all reached a quench plateau very little training [20].) Although most of the data points lie slightly below the first diagonal, the agreement is relatively good. This indicates that the short sample estimations are quite reliable.

## 8.4 QUENCH ORIGINS

Quenches originate because of a crossing of the superconductor critical surface somewhere in the magnet coil. This crossing occurs either along the "peak magnetic flux density versus transport current density" line or along the temperature axis.

The maximum quench current at a given temperature is estimated using a parametrization of the superconductor critical surface such as the one given by Eq. (12) and assuming an average value of $J_C$ at 4.2 K and 5 T over the magnet coil. The average $J_C$ is usually determined from measurements on a cable short sample. Nevertheless, it can happen that the crossing of the critical surface along the peak field line occur at an overall cable current that is below the expected $I_{qm}$ or $I_{ss}$. Such quenches have at least two origins: (1) a local cable degradation, which results in a local decrease of the critical current and of the critical current density and (2) a large imbalance in the current distribution among the cable strands, which results in a strand carrying much more current than average and hitting the critical surface ahead of the others. Quenches of the first kind are of the same nature as quenches occurring at the short-sample limit and they can all be identified as *conductor-limited* quenches. Quenches of the second kind are more likely to occur at high ramp rates and are discussed in the section on quench performance versus ramp rate.

The temperature rises which initiate quenches result from energy depositions on the magnet coil. These energy depositions have at least three origins: (1) mechanical disturbances such as stress relief or frictional motion under the Lorentz force, (2) synchrotron radiation or beam losses and (3) power dissipation from interstrand coupling currents. Quenches of the first origin are referred to as *mechanically-induced* quenches and reveal flaws in the mechanical design or in the assembly procedures which must be analyzed and corrected. The effects of synchrotron radiation can be reduced by implementing an intercepting screen within the beam tube. Coupling losses are only of concern for fast current cycles.

## 8.5 DISCRIMINATING BETWEEN CONDUCTOR-LIMITED AND MECHANICALLY-INDUCED QUENCHES

Conductor-limited quenches correspond to a crossing of the critical surface along the peak magnetic flux density line. When changing the operating temperature from $T_0$ to ($T_0$ + $\Delta T_0$), the quench current should follow the superconductor critical surface and vary from $I_q(T_0)$ to $I_q(T_0+\Delta T_0)$. Hence, the currents of conductor-limited quenches are expected to exhibit a strong correlation with temperature. Conversely, the energy depositions resulting from mechanical disturbances should mainly depend on the Lorentz force level and should be relatively insensitive to small temperature variations. Hence the currents of mechanically-induced quenches are not expected to be strongly related to magnet temperature. Thus a practical method for discriminating between conductor-limited quenches and mechanically-induced quenches is to vary the operating temperature of the magnet slightly — for example, to increase it and then decrease it by 50 mK — and to see if the quench current follows the change or not.

Figure 17(b) shows a plot of current at quench versus temperature at quench for the quench data of SSC dipole magnet prototype DD0017 presented in Fig. 17(a). (The temperature is measured by carbon resistors located in the helium interconnect region at both extremities of the horizontal magnet test stand). Quenches 3 to 7 and 10 to 13 exhibit a clear correlation between quench current and temperature, while quenches 1 and 2, and 8 and 9 (the first two training quenches of each test cycle) are scattered. Hence, quenches 1, 2, 8, and 9 are likely to be mechanically-induced quenches, while all the others are conductor-limited quenches. Note that for quenches 6 and 7, on one hand, and quenches 12 and 13, on the other hand, the temperature was deliberately raised from its nominal 4.35 K value to check if the quench current decreased accordingly.

## 8.6 MECHANICAL TRAINING

Among the various quench origins considered above, only the mechanical disturbances are likely to be affected by successive ramps to quench and lead to the kind of improvement in magnet performance referred to as training. A phenomenological explanation of magnet training is as follows.

When energizing a magnet, strong Lorentz forces are applied to the conductor strands which are transmitted to the coil support system through the insulation. In a geometry as complex as that of a dipole or a quadrupole coil assembly, there are many interfaces where the Lorentz forces have tangential components which are counteracted by friction. As the current is

ramped up and the Lorentz forces increase, it can happen that, somewhere in the coil, a static-friction coefficient is exceeded. Sliding then occurs, which results in heat dissipation and a local temperature rise. If the local temperature rise is large enough, a quench is initiated.

In the case of a quench caused by a so-called *stick-slip motion* in the magnet assembly, the motion responsible for the quench and/or the thermal stresses developed in the magnet coil during the quench can improve the mechanical stability of the troubled interface. As a result, upon subsequent energizations, the Lorentz forces are better supported and the same current level can be achieved without exceeding the local static-friction coefficient. Then, the current can be further ramped up until, somewhere else in the coil, another static-friction coefficient is exceeded, which, in turn, provokes a frictional motion large enough to initiate a quench — and so on. Quench after quench, the current can be ramped up to higher levels until it is reaches the maximum quench current.

It goes without saying that if the mechanical flaws at the origins of the disturbances are too large, the magnet cannot be trained and keeps quenching erratically.

## 8.7 QUENCH PERFORMANCE AS A FUNCTION OF RAMP RATE

Let us consider an accelerator magnet which has been trained to a stable plateau. When subsequently performing ramps to quench at increasing ramp rates, at least two mechanisms are in competition to degrade the quench performance: (1) the generation of interstrand coupling currents, which are superimposed to the transport current and dissipate power when crossing the interstrand resistances and (2) the possible modification of the transport-current distribution among the cable strands which can result in the apparition of large current imbalances. The interstrand coupling currents, which have been described in a specific section, are expected to increase as a function of ramp rate, leading to a monotonic decrease of the quench current. Determining how the distribution of transport current among the cable strands (briefly evoked in the section on longitudinal periodicity) is influenced by the ramp rate requires additional background informations.

As we have seen, the Rutherford-type conductor used in superconducting particle accelerator magnets consists of a few tens of strands, twisted together, and shaped into a flat, two-layer, slightly keystoned cable. Each cable strand is characterized by a voltage-current curve and a self-inductance. Each strand pair is characterized by a mutual inductance. Also, all the strands are coupled through the interstrand resistances and the splice resistances at the coil ends. During energization, the current distributes itself among the cable strands according to this intricate network of resistances and inductances. At low ramp rate, the current distribution

is mainly determined by the resistive elements of the circuit, but as the ramp rate is increased, the inductive elements start to play a role, and end up being the dominant elements at large ramp rate. If the strands are identical and interchangeable, they all carry the same current, and changing the ramp rate is not expected to have any influence. However, if for one reason or another, the strands are not identical or are not interchangeable, the static and dynamic current distributions can be different. Then, as the ramp rate is increased, the current distribution changes from one to the other, resulting in a quench current evolving between two asymptotic values: (1) one for ramp rates tending towards zero and (2) one for large ramp rates. This implies in particular that, unlike in the case of interstrand coupling currents, the quench current degradation arising from transport current imbalances is expected to flatten out at large ramp rates.

Illustrations of the different ramp rate behaviors that can be encountered are given in Figs. 19(a) and 19(b) which display summary plots of quench current versus ramp rate for selected 5-cm-aperture, 15-m-long SSC dipole magnet prototypes [20,27,92]. (The magnets are grouped according to the manufacturer and the production batch of their inner cable strands.) It appears that, for the magnets of Fig. 19(a), the quench current remains roughly constant for ramp rates up to 25 A/s, above which it starts to decrease linearly as a function of ramp rate. The worst case is magnet DCA312, which, at 200 A/s, quenches at 2180 A, corresponding to about 30% of its initial quench current. In comparison, for the magnets in Fig. 19(b), the quench current starts by dropping significantly at low ramp rates, while the degradation is much milder at large ramp rates. The worst case is magnet DCA319, for which the quench current decreases from 7334 A at 1 A/s to 6156 A/s at 25 A/s, but is still of the order of 5000 A at 250 A/s.

The behavior of the magnets in Fig.19(a) is referred to as *type-A* and is believed to be dominated by interstrand coupling currents arising from low and non-uniform interstrand resistances in the Rutherford-type cables [92]. The behavior of the magnets of Fig. 19(b) is referred to as *type-B* and is believed to be dominated by imbalances in the transport-current distribution. The exact origin of these imbalances has not been identified.

## 8.8 SPECIFICATION ON QUENCH PERFORMANCE

The possibility of training superconducting magnets is rather encouraging for it leaves the hope that, even if the first quenches are below the expected maximum quench current, the performance may improve and the magnet may finally reach the design current. Nevertheless, it is not reasonable to build an accelerator with several hundred or several thousand magnets that need to be trained each time they are put into operation (or at least, each time they are

warmed up to room temperature). If the magnet prototypes exhibit some training, the origin of this training has to be understood, and the design of the magnet has to be modified so as to eliminate, or at least to limit, the training quenches to levels which are well above the operating current of the accelerator.

In any case, it is indispensable to carry out systematic tests before installing the magnets into the tunnel to ensure that their quench performance is adequate and does not degrade upon extended current and thermal cycling [135].

# 9 QUENCH PROTECTION

## 9.1 THE EFFECTS OF A QUENCH

### 9.1.1 CONDUCTOR HEATING

Although most R&D programs have been successful in developing magnet designs that can be mass-produced and meet accelerator requirements, quenches do occur in accelerator operations. These quenches must be handled in order to avoid any damage of the quenching magnet, to ensure the safety of the installation and to minimize down time.

As we have seen in the section on what is a quench, once a small volume of conductor has switched to the normal resistive state, it dissipates power by the Joule effect. A fraction of this dissipated power is transferred to the surroundings of the initial volume of transition (either along the conductor, or, transversely, to the conductor insulation or the helium), but the main part is consumed locally in overheating the conductor. In a very short time (a few tenths of a second in the case of a dipole or quadrupole magnet) the conductor temperature, initially that of the helium, reaches room temperature, and, if the magnet is not discharged, keeps on increasing.

### 9.1.2 MAXIMUM TEMPERATURE REQUIREMENT

The temperature rise consecutive to a quench must be limited for at least three reasons: (1) to restrict the thermal stresses induced in the quenching coil, (2) to prevent degradation of superconductor properties, and (3) to avoid insulation damage.

For most materials, thermal expansion starts to be significant for temperatures above 100 K. The critical current density of NbTi is affected by exposure to temperatures above 250 °C. The degradation amplitude depends on the temperature level and on the duration of the exposure: at 250 °C, it takes of the order of 1 hour to get a significant degradation, while it may take less than a minute at 400–450 °C [136]. This degradation results from a growth of the $\beta$-phase grains in the NbTi alloy microstructure, which affects the distribution of $\alpha$-Ti precipitates and alters pinning. (The $\alpha$-Ti precipitates get dissolved for temperatures above 600 °C). Finally, the polyimide materials used to insulate NbTi cables lose most of their mechanical properties for temperatures above 500 °C.

It follows that an upper limit for conductor heating consecutively to a quench is 400 °C. Most magnets are designed not to exceed 300 to 400 K, and whenever possible, the limit should be set to 100 K.

### 9.1.3 PROTECTING A QUENCHING MAGNET

The source of conductor heating in a quenching magnet is power dissipation by the Joule effect. Power keeps being dissipated as long as there is current in the magnet coil. To eliminate the heat source and limit the temperature rise, it is thus necessary to ramp the current down.

To discharge a quenching magnet, all its stored magnetic energy must be converted into resistive power. If the quench propagates very slowly, and the zone where the conductor has switched to the normal state remains confined to a small volume, there is a risk that a large fraction of the stored energy be dissipated in this volume. In the case of a string of magnets connected electrically in series, it may even happen that the energy of the whole string be dissipated in the quenching magnet. Hence, to prevent burnout, it is desirable to maximize the volume in which the energy is dissipated by ensuring that the normal resistive zone spreads rapidly throughout the quenching coil. This can be done by means of heaters, implemented near the magnet coils and fired as soon as a quench is detected. These heaters are referred to as *quench protection heaters.*

In comparison to other superconducting magnets, most accelerator magnets do require an active quench protection system because of the rapidity of the temperature rise resulting from the high current density and the low fraction of stabilizing copper in the cable strands. One notable exception are the RHIC dipole magnets, whose one-layer coil assemblies are wound from a cable with a high copper-to-superconductor ratio (2.25 to 1), and which do not rely on quench protection heaters.

## 9.2 HOT SPOT TEMPERATURE

### 9.2.1 ESTIMATING HOT SPOT TEMPERATURE

The volume of conductor that heats up the most significantly during a quench is the spot where the quench first originated. It is called the *hot spot.* An upper limit of the hot spot temperature, $T_{max}$, can be determined by assuming that, near the hot spot, all the power dissipated by the Joule effect is used to heat up the conductor. Then, near the hot sport, the heat balance equation reduces to

$$C(T)\,\frac{dT}{dt} = \rho(T)\left[\frac{I(t)}{S}\right]^2 \tag{48}$$

where $C$ is the overall specific heat per unit volume of conductor, $\rho$ is the overall conductor resistivity in the normal state, $S$ is the conductor cross-sectional area and $I(t)$ is the current at time $t$.

Eq. (48) can be integrated under the form

$$S^2 \int_{T_0}^{T_{max}} dT\,\frac{C(T)}{\rho(T)} = \int_{t_0}^{+\infty} dt\; I(t)^2 \tag{49}$$

where $t_0$ is the time of quench start and $T_0$ is the coil temperature at $t_0$.

The left member of Eq. (49) depends only on conductor properties whereas the right member depends only on the characteristics of current decay. The right-hand side integral, divided by $10^6$, is called the *MIIT integral* (Mega I times I versus Time integral) and its value is referred to as *number of MIITs.* The maximum temperatures computed from the numbers of MIITs have been shown to be in fairly good agreement with actual measurements of hot spot temperatures on quenching magnets [137].

### 9.2.2 LIMITING HOT SPOT TEMPERATURE

The hot spot temperature can be limited by acting on either member of Eq. (49). Regarding the left member, the only conceivable action is to reduce the overall conductor resistivity by increasing the copper-to-superconductor ratio. However, and as explained in the conductor section, the copper-to-superconductor ratio must also be optimized to ensure a high overall critical current. Regarding the right member, the MIIT integral can be minimized by: (1) detecting the quench as soon as possible, (2) turning off the power supply (case of a single magnet) or forcing the current to bypass the quenching magnet (case of a magnet string), (3) firing the quench protection heaters and (4) discharging the quenching magnet or the magnet string.

## 9.3 QUENCH DETECTION

The magnets are connected to quench detection systems which monitor the occurrence of a resistive voltage in the coil windings or the coils leads. The resistive voltage has to be discriminated from inductive voltages arising from magnet ramping. The inductive components

are cancelled out by considering voltage differences across two identical coil assemblies or two identical parts of a given coil assembly (*e.g.*, the upper and lower half coils in a dipole magnet). When the resistive voltage exceeds a preset threshold over a time exceeding a preset duration, the detection system generates a trigger which signals the occurrence of a quench.

## 9.4 PROTECTION OF A SINGLE MAGNET

### 9.4.1 CURRENT DISCHARGE

Let us first consider the case of a single magnet and let us assume that, once a quench is detected, the power supply is turned off and the magnet is switched to an external dump resistor, $R_{ext}$. The current decay is determined by

$$L_m \frac{dI}{dt} + [R_q(t)+R_{ext}]\, I = 0 \tag{50}$$

where $L_m$ is the magnet inductance and $R_q(t)$ is the developing resistance in the quenching coils. Furthermore, the total voltage across the magnet, $V_m$, is given by

$$V_m = R_{ext}\ I(t) \tag{51}$$

To limit the number of MIITs, it is desirable to have a fast current decay. Eq. (50) shows that fast decay rates are obtained either by means of a large $R_{ext}$ or by ensuring that $R_q(t)$ increases rapidly. For some magnets, an external resistor can be used to extract a significant fraction of the stored magnetic energy. However, it is also required to keep $V_m$ to a reasonable level (typically: less than 1 kV) to avoid insulation breakdown. Given the order of magnitude of $I$ (up to 15 kA), this imposes a small $R_{ext}$ (typically: a few hundredth of ohms) which, during a quench, is soon overcome by $R_q(t)$. Hence, for accelerator magnets, the current decay is largely dominated by the resistance development in the quenching coils and the decay rate can be increased only by speeding up $R_q(t)$.

### 9.4.2 MAXIMUM VOLTAGE TO GROUND

The developing resistance in the quenching coil separates the coil impedance into several parts [p. 137 of Reference 4]: un-quenched parts across which the voltage is mainly inductive and quenched parts across which the voltage is mainly resistive. The resistive and inductive voltages compensate each other partially so that their sum equals $V_m$. The voltage distribution with respect to ground depends on the respective sizes and locations of these various parts.

The more uniform the quench development, the lower the maximum voltage to ground. As an illustration, Fig. 20 shows the voltage distribution in a quenching magnet. Here, $V_m$ is assumed to be nil and $R_q$ is assumed to be concentrated near two thirds of the magnet length.

### 9.4.3 QUENCH PROTECTION HEATERS

As described earlier, to speed up and uniformize quench development, most accelerator magnets rely on quench protection heaters which are fired as soon as a quench is detected. The heaters are usually made of stainless steel strips, which are copper clad at regular intervals along their lengths and which are placed on the outer surface of the coil assemblies. Note, however, that the heater firing unit relies on a capacitor bank and that it takes some time for the energy to be released. Note also that the heaters have to be electrically insulated from the coil and that this electrical insulation introduces a thermal barrier. As a result, there is a non negligible delay between the firing of the heaters and their effect on the coils, during which, we must rely on natural quench propagation [138]. The heaters and their implementations in the magnet assembly are optimized to reduce this delay.

## 9.5 PROTECTION OF A MAGNET STRING

In an accelerator, the magnet ring is divided into several sectors made up of series-connected magnets. The sectors are powered independently and are electrically independent. Once a quench is detected in a magnet, the power supply of the sector to which the magnet belongs is turned off and the sector is discharged over a dump resistor.

Unlike in the case of a single magnet, the current decay rate in the sector must be limited for at least two reasons: (1) to prevent the induction of large coupling currents in the magnet coils (which may quench the remaining magnets in the sector, resulting in general warming and significant helium venting), and (2) to avoid the occurrence of unacceptable voltages to ground (because of the large overall inductance of the sector). A too slow decay rate, however, creates the risk that a significant fraction of the total energy stored in the sector be dissipated in the quenching magnet, resulting in destructive overheating.

These contradictory considerations can be reconciled by forcing the current to bypass the quenching magnet and by ramping the current down at the desired rate in the remaining un-quenched magnets. The bypass elements consist of diodes (or thyristors) connected in parallel to individual or small groups of magnets, as shown in Fig. 21. As long as the magnets are superconducting, the current flows through the magnets. Once a magnet has quenched and starts to develop a resistive voltage, the main current is bypassed through the diode connected

in parallel and the quenching magnet is discharged over the diode circuit. The current decay is determined by an equation similar to Eq. (50), except that $R_{ext}$ has to be replaced by the resistance associated with the bypass element, $R_b$.

HERA, RHIC and LHC rely on silicon diodes which are mounted inside the helium cryostats and operate at cryogenic temperatures. The main requirements for these cold diodes are [139]: (1) small forward voltage and low dynamic resistance (to limit power dissipation in the diodes), (2) good radiation hardness and (3) large backward voltage. In the case of the Tevatron, which has a short current ramp time resulting in large inductive voltages across the bypass elements, the diodes are replaced by thyristors operating as fast switches [140]. The thyristors are located outside the magnet cryostats and require additional power leads and cryogenic feedthroughs.

The protection system of the magnet ring must be carefully designed and thoroughly tested before starting up the machine. The system tests are usually carried out on a cell or a half-cell representative of the magnet lattice and all failure modes are investigated [141–143].

## 10 BRIEF SUMMARY

As of today, two large accelerator main rings, Tevatron and HERA, have been built and are reliably operating, and work is under way on two other superconducting colliders: RHIC and LHC. The construction of RHIC is near completion and the industrial contracts for the mass production of LHC magnets will be awarded in 1999.

Since the time of the Tevatron (late 1970's), a factor of about two has been gained on the critical current density of NbTi at 4.2 K and 5 T and a dipole field of 10.5 T has been reached on a short magnet model relying on NbTi cables at 1.8 K. In recent years, encouraging results have been obtained on a couple of short dipole magnet models relying on $Nb_3Sn$ cables, which may open the range 10 to 15 T.

## ACKNOWLEDGMENTS

The author wishes to thank L. Bottura, H. Desportes, M. Peyrot, J.M. Rifflet and F. Simon for their comments on the manuscript and C.E. Bruzek for many fruitful discussions.

## BIBLIOGRAPHY


[1] D.A. Edwards and M.J. Syphers, *An Introduction to the Physics of High Energy Particle Accelerators*, New York: John Wiley & Sons, 1993.

[2] H. Padamsee, Superconducting RF. In M. Month and M. Dienes (eds.), *The Pysics of Particle Accelerators*, AIP Conference Proceedings **249**(2): 1402–1482, 1992.

[3] H. Padamsee and J. Knobloch, Issues in superconducting RF technology. In S.I. Kurokawa, M. Month and S. Turner (eds.), *Frontiers of Accelerator Technology*, Singapore: World Scientific, 101–183, 1996.

[4] K.-H. Mess, P. Schmüser and S. Wolf, *Superconducting Accelerator Magnets*, Singapore: World Scientific, 1996.

[5] H.T. Edwards, The Tevatron energy doubler: a superconducting accelerator, *Ann. Rev. Nucl. Part. Sci.*, **35**: 605–660 (1985).

[6] A.V. Tollestrup, Superconducting magnets. In R.A. Carrigan, F.R. Huson and M. Month (eds.), *Physics of High Energy Accelerators*, AIP Conference Proceedings. **87**: 699–804, 1982.

[7] K. Koepke, G. Kalbfleisch, W. Hanson, A. Tollestrup, J. O'Meara and J. Saarivirta, Fermilab doubler magnet design and fabrication techniques, *IEEE Trans. Magn.*, **MAG-15**(1): 658–661, 1979.

[8] F. Turkot, W.E. Cooper, R. Hanft and A. McInturff, Maximum field capabilities of energy saver superconducting magnets, *IEEE Trans. Nucl. Sci.*, **NS–30**(4): 3387–3389 (1983).

[9] R. Hanft, B.C. Brown, W.E. Cooper, D.A. Gross, L. Michelotti, E.E. Schmidt and F. Turkot, Magnetic field properties of Fermilab energy saver dipoles, *IEEE Trans. Nucl. Sci.*, **NS–30**(4): 3381–3383, 1983.

[10] E.E. Schmidt, B.C. Brown, W.E. Cooper, H.E. Fisk, D.A. Gross, R. Hanft, S. Ohnuma and F.T. Turkot, Magnetic field data on Fermilab energy saver quadrupoles, *IEEE Trans. Nucl. Sci.*, **NS–30**(4): 3384–3386, 1983.

[11] B.H. Wiik, The status of HERA, *Conference Record of the 1991 IEEE Particle Accelerator Conference*, IEEE catalogue **91CH3038–7**: 2905–2909, 1991.

[12] S. Wolff, Superconducting HERA magnets, *IEEE Trans. Magn.*, **24**(2): 719–722, 1988.

[13] P. Schmüser, Field quality issues in superconducting magnets, *Conference Record of the 1991 IEEE Particle Accelerator Conference*, IEEE catalogue **91CH3038–7**: 37–41, 1989.

[14] R. Meinke, Superconducting magnet system for HERA, *IEEE Trans. Magn.*, **27**(2): 1728–1734, 1991.

[15] R. Auzolle, A. Patoux, J. Perot and J.M. Rifflet, Construction and test of superconducting quadrupole prototypes for HERA," *Journal de Physique*, **45**(Colloque C1, supplément au No. 1): 263–270, 1984.

[16] R. Auzolle, J. Pérot, J.M. Rifflet, A. Fokken, O. Peters, and S. Wolff, First industry made superconducting quadrupoles for HERA, *IEEE Trans. Magn.*, **25**(2): 1660–1662, 1989.

[17] V.I. Balbekov and G.G. Gurov, IHEP accelerating and storage complex: status and possibility of B–factory, *Nuclear Instruments and Methods in Physics Research*, **A 333**: 189–195, 1993.

[18] A.V. Zlobin, UNK superconducting magnets development, *Nuclear Instruments and Methods in Physics Research*, **A 333**: 196–203, 1993.

[19] R.F. Schwitters, Future hadron collider: the SSC. In J.R. Sanford (ed.), *Proceedings of the 26th International Conference on High Energy Physics*, AIP Conference Proceedings **272**: 306–320 (1993).

[20] A. Devred, T. Bush, R. Coombes, J. DiMarco, C. Goodzeit, J. Kuzminski, W. Nah, T. Ogitsu, M. Puglisi, P. Radusewicz, P. Sanger, R. Schermer, R. Stiening, G. Spigo, J. Tompkins, J. Turner, Y. Yu, Y. Zhao, H. Zheng, M. Anerella, J. Cottingham, G. Ganetis, M. Garber, A. Ghosh, A. Greene, R Gupta, A. Jain, S. Kahn, E. Kelly, G. Morgan, J. Muratore, A. Prodell, M. Rehak, E.P. Rohrer, W. Sampson, R. Shutt, R. Thomas, P. Thompson, P. Wanderer, E. Willen, M. Bleadon, R. Bossert, J. Carson, S. Delchamps, S. Gourlay, R. Hanft, W. Koska, M. Kuchnir, M. Lamm, P. Mantsch, P.O. Mazur, D. Orris, J. Ozelis, T. Peterson, J. Strait, M. Wake, J. Royet, R. Scanlan and C. Taylor, Review of SSC dipole magnet mechanics and quench performance. In J. Nonte (ed.), *Supercollider 4*, New York: Plenum Press, 113–136, 1992.

[21] P. Wanderer, M. Anerella, J. Cottingham, G. Ganetis, M. Garber, A. Ghosh, A. Greene, R Gupta, A. Jain, S. Kahn, E. Kelly, G. Morgan, J. Muratore, A. Prodell, M. Rehak, E.P. Rohrer, W. Sampson, R. Shutt, R. Thomas, P. Thompson, E. Willen, A. Devred, T. Bush, R. Coombes, J. DiMarco, C. Goodzeit, J. Kuzminski, W. Nah, T. Ogitsu, M. Puglisi, P. Radusewicz, P. Sanger, R. Schermer, J. Tompkins, J. Turner, Y. Yu, Y. Zhao, H. Zheng, M. Bleadon, R. Bossert, J. Carson, S. Delchamps, S. Gourlay, R. Hanft, W. Koska, M. Kuchnir, M. Lamm, P. Mantsch, P.O. Mazur, D. Orris, J. Ozelis, T. Peterson, J. Strait, M. Wake, J. Royet, R. Scanlan and C. Taylor, A summary of SSC dipole magnet field quality measurements. In J. Nonte (ed.), *Supercollider 4*, New York: Plenum Press, 137–149, 1992.

[22] W. Nah, A. Akhmetov, M. Anerella, R. Bossert, T. Bush, D.W. Capone II, J. Carson, R. Coombes, J. Cottingham, S.W. Delchamps, A. Devred, J. DiMarco, G. Ganetis, M. Garber, C. Goodzeit, A. Ghosh, S. Gourlay, A. Greene, R. Gupta, R. Hanft, A. Jain, S. Kahn, E. Kelly, W. Koska, M. Kuchnir, J. Kuzminski, M.J. Lamm, P. Mantsch, P.O. Mazur, G. Morgan, J. Muratore, T. Ogitsu, D. Orris, J. Ozelis, T. Peterson, E.G. Pewitt, A. Prodell, M. Puglisi, P. Radusewicz, M. Rehak, E.P. Rohrer, J. Royet, W. Sampson, P. Sanger, R. Scanlan, R. Schermer, R. Shutt, R. Stiening, J. Strait, C. Taylor, R. Thomas, P. Thompson, J.C. Tompkins, J. Turner, M. Wake, P. Wanderer, E. Willen, Y. Yu, J. Zbasnik, Y. Zhao and H. Zheng, Quench characteristics of 5-cm aperture, 15-m Long SSC dipole magnet prototypes, *IEEE Trans. Applied Superconductivity*, **3**(1): 658–661, 1993.

[23] Y. Zhao, A. Akhmetov, M. Anerella, R. Bossert, T. Bush, D.W. Capone II, J. Carson, R. Coombes, J. Cottingham, S.W. Delchamps, A. Devred, J. DiMarco, G. Ganetis, M. Garber, C. Goodzeit, A. Ghosh, S. Gourlay, A. Greene, R. Gupta, R. Hanft, A. Jain, S. Kahn, E. Kelly, W. Koska, M. Kuchnir, J. Kuzminski, M.J. Lamm, P. Mantsch, P.O. Mazur, G. Morgan, J. Muratore, W. Nah, T. Ogitsu, D. Orris, J. Ozelis, T. Peterson, E.G. Pewitt, A. Prodell, M. Puglisi, P. Radusewicz, M. Rehak, E.P. Rohrer, J. Royet, W. Sampson, P. Sanger, R. Scanlan, R. Schermer, R. Shutt, R. Stiening, J. Strait, C. Taylor, R. Thomas, P. Thompson, J.C. Tompkins, J. Turner, M. Wake, P. Wanderer, E. Willen, Y. Yu, J. Zbasnik and H. Zheng, Current dependence of harmonic field coefficients of 5-cm aperture, 15-m Long SSC dipole magnet prototypes, *IEEE Trans. Applied Superconductivity*, **3**(1): 674–677, 1993.

[24] T. Ogitsu, A. Akhmetov, M. Anerella, R. Bossert, T. Bush, D.W. Capone II, J. Carson, R. Coombes, J. Cottingham, S.W. Delchamps, A. Devred, J. DiMarco, G. Ganetis, M. Garber, C. Goodzeit, A. Ghosh, S. Gourlay, A. Greene, R. Gupta, R. Hanft, A. Jain, S. Kahn, E. Kelly, W. Koska, M. Kuchnir, J. Kuzminski, M.J. Lamm, P. Mantsch, P.O. Mazur, G. Morgan, J. Muratore, W. Nah, D. Orris, J. Ozelis, T. Peterson, E.G. Pewitt, A. Prodell, M. Puglisi, P. Radusewicz, M. Rehak, E.P. Rohrer, J. Royet, W. Sampson, P. Sanger, R. Scanlan, R. Schermer, R. Shutt, R. Stiening, J. Strait, C. Taylor, R. Thomas, P. Thompson, J.C. Tompkins, J. Turner, M. Wake, P. Wanderer, E. Willen, Y. Yu, J. Zbasnik, Y. Zhao and H. Zheng, Mechanical performance of 5-cm aperture, 15-m long SSC dipole magnet prototypes, *IEEE Trans. Applied Superconductivity*, **3**(1): 686–691, 1993.

[25] P. Wanderer, M. Anerella, J. Cottingham, G. Ganetis, M. Garber, A. Ghosh, A. Greene, R Gupta, A. Jain, S. Kahn, E. Kelly, G. Morgan, J. Muratore, A. Prodell, M. Rehak, E.P. Rohrer, W. Sampson, R. Shutt, R. Thomas, P. Thompson, E. Willen, C. Goodzeit and P. Radusewicz, Magnetic design and field quality measurements of full length 50-mm aperture SSC model dipoles built at BNL, *Int. J. Mod. Phys. A*, Proc. Suppl. **2B**: pp. 641–643, 1993.

[26] J. Strait, R. Bossert, J. Carson, S.W. Delchamps, S. Gourlay, R. Hanft, W. Koska, M. Kuchnir, M.J. Lamm, P.O. Mazur, A. Mokhtarani, D. Orris, J. Ozelis, M. Wake, A. Devred, J. DiMarco, J. Kuzminski, M. Puglisi, J.C. Tompkins, Y. Yu, Y. Zhao, H. Zheng and T. Ogitsu, Magnetic field measurements of full length 50-mm aperture SSC dipole magnets at Fermilab," *Int. J. Mod. Phys. A*, Proc. Suppl. **2B**: 656–658, 1993.

[27] R.I. Schermer, Status of superconducting magnets for the superconducting super collider, *IEEE Trans. Magn.*, **30**(2): 1587–1594, 1994.

[28] H. Foelsche, H. Hahn, M. Harrison, S. Ozaki and M.J. Rhoades-Brown, The relativistic heavy ion collider, RHIC. In H. Schopper (ed.), *Advances of Accelerator Physics and Technologies*, Advanced Series on Directions in High Energy Physics **12**, Singapore: World Scientific, 104–131, 1993.

[29] P. Wanderer, J. Muratore, M. Anerella, G. Ganetis, A. Ghosh, A. Greene, R. Gupta, A. Jain, S. Kahn, E. Kelly, G. Morgan, A. Prodell, M. Rehak, W. Sampson, R. Thomas, P. Thompson and E. Willen, Construction and testing of arc dipoles and quadrupoles for the relativistic heavy ion collider (RHIC) at BNL, *Proceedings of the 1995 Particle Accelerator Conference*, IEEE catalogue **95CH35843**: 1293–1297, 1995.

[30] A. Greene, M. Anerella, J. Cozzolino, J. Escallier, D. Fisher, G. Ganetis, A. Ghosh, R. Gupta, A. Jain, S. Kahn, E. Kelly, R. Lebel, G. Morgan, A. Morgillo, S. Mulhall, J. Muratore, S. Plate, A. Prodell, M. Rehak, W. Sampson, R. Thomas, P. Thompson, P. Wanderer and E. Willen, The magnet system of the relativistic heavy ion collider (RHIC), *IEEE Trans. Mag.*, **32**(4): 2041–2046, 1996.

[31] M. Anerella, D.H. Fisher, E. Sheedy and T. McGuire, Industrial production of RHIC magnets, *IEEE Trans. Mag.*, **32**(4): 2059–2064, 1996.

[32] L.R. Evans, The large hadron collider project. In T. Haruyama, T. Mitsui and K. Yamafuji (eds.), *Proceedings of the 16th International Cryogenic Engineering Conference/International Cryogenic Materials Conference*, London: Elsevier, 45–52, 1997.

[33] The LHC Magnet Team, reported by R. Perin, Status of the Large Hadron Collider magnet development, *IEEE Trans. Mag.*, **30**(4), pp. 1579–1586, 1994.

[34] R. Perin, Status of LHC programme and magnet development, *IEEE Trans. Appl. Supercond.*, **5**(2): 189–195, 1995.

[35] N. Siegel, Status of the Large Hadron Collider and magnet program, *IEEE Trans. Appl. Supercond.*, **7**(2): 252–257, 1997.

[36] J.M. Baze, D. Cacaut, M. Chapman, J.P. Jacquemin, C. Lyraud, C. Michez, Y. Pabot, J. Perot, J.M. Rifflet, J.C. Toussaint, P. Védrine, R. Perin, N. Siegel and T. Tortschanoff, Design and fabrication of the prototype superconducting quadrupole for the CERN LHC project, *IEEE Trans. Magn.*, **28**(1): 335–337, 1992.

[37] J.M. Rifflet, J. Cortella, J. Deregel, P. Genevey, J. Pérot, P. Vedrine, K.H. Henrichsen, F. Rodriguez–Mateos, N. Siegel and T. Tortschanoff, Cryogenic and mechanical measurements of the first two LHC lattice quadrupole prototypes. In V. Suller and Ch. Petit-Jean-Genaz (eds.), *Proc. of Fourth European Part. Acc. Conf.*, Singapore: World Scientific, 2265–2267, 1994.

[38] A. Devred, J. Belorgey, J. Deregel, B. Gallet, P. Genevey, J.M. Rifflet, J.Cl. Sellier, P. Védrine and J. Billan, Field quality of LHC/Saclay arc quadrupole magnet prototype, In S. Myers, A. Pacheco, R. Pascual, Ch. Petit-Jean-Genaz and J. Poole (eds.), *Proc. of Fifh European Part. Acc. Conf.*, Bristol: Institute of Physics Publishing, 2225–2227, 1996.

[39] M.N. Wilson, Superconducting magnets for accelerators: a review, *IEEE Trans. Appl. Supercond.*, **7**(2): 727–732, 1997.

[40] A. den Ouden, S. Wessel, E. Krooshoop, R. Dubbeldam and H.H.J. ten Kate, An experimental 11.5 T $Nb_3Sn$ LHC type of dipole magnet, *IEEE Trans. Magn.*, **30**(4), 2320–2323, 1994.

[41] A. den Ouden, S. Wessel, E. Krooshoop and H ten Kate, Application of $Nb_3Sn$ superconductors to high-field accelerator magnets, *IEEE Trans. Appl. Supercond.*, **7**(2): 733–738, 1997.

[42] D. Dell'Orco, R.M. Scanlan and C.E. Taylor, Design of the $Nb_3Sn$ dipole D20," *IEEE Trans. Appl. Supercond.*, **3**(1): 82–86, 1993.

[43] A.D. McInturff, R. Benjegerdes, P. Bish, S. Capsi, K. Chow, D. Dell'Orco, D. Dietderich, R. Hannaford, W. Harnden, H. Higley, A. Lietzke, L. Morrison, R. Scnalan, J. Smithwick, C. Taylor and J.M. van Oort, Test results for a high field (13T) $Nb_3Sn$ dipole, Presented at the 1997 Particle Accelerator Conference, Vancouver, Canada, 12–16 May, 1997.

[44] E. Gregory, Conventional wire and cable technology. In M. Month and M. Dienes (eds.), *The Pysics of Particle Accelerators*, AIP Conference Proceedings, **249**(2): 1198–1229, 1992.

[45] P.J. Lee, D.C. Larbalestier, K. Togano, K. Tachikawa, M. Suzuki, K. Hamasaki, K. Noto and K. Watanabe, Chapter 5: Fabrications Methods. In K. Osamura (ed.), *Composite Superconductors*, New York: Marcel Dekker, Inc., 237–321, 1994.

[46] M.N. Wilson, Superconducting materials for magnets. In S. Turner (ed.), *Proceedings of the CERN Accelerator School on Superconductivity in Particle Acclerators*, CERN **96–03**: 47–69, 1996.

[47] E.W. Collings, *Applied Superconductivity, Metallurgy and Physics of Titanium Alloys, Volume 1: Fundamentals*, New York: Plenum Press, 1986.

[48] E.W. Collings, *Applied Superconductivity, Metallurgy and Physics of Titanium Alloys, Volume 2: Applications*, New York: Plenum Press, 1986.

[49] P.J. Lee and D.C. Larbalestier, Development of nanometer scale structures in composites of Nb–Ti and their effect on the superconducting critical current densities, *Acta Metall.*, **35**(10): 2523–2356, 1987.

[50] C. Meingast and D.C. Larbalestier, Quantitative description of a very high critical current density NbTi superconductor during its final optimization strain. II. Flux pinning mechanisms, *J. Appl. Phys.*, **66**(12), 5971-5983, 1989.

[51] D.G. Hawksworth and D.C. Larbalestier, Enhanced value of $H_{C2}$ in Nb–Ti ternary and quaternary alloys, *Adances in Cryogenic Engineering (Materials)*, **26**: 479–486, 1980.

[52] P.J. Lee and D.C. Larbalestier, Determination of the flux pinning force of α–Ti ribbons in Nb46.5wt% Ti produces by heat treatments of varying temperature, duration and frequency, *Journal of Materials Science*, **23**, 3951–3957, 1988.

[53] P.J. Lee, J.C. McKinnel and D.C. Larbalestier, Restricted, novel heat treatments for obtaining high $J_C$ in Nb46.5wt%Ti, *Adances in Cryogenic Engineering (Materials)*, **36**: 287–294, 1990.

[54] P.J. Lee, D.C. Larbalestier, J.C. McKinnell and A.D. McInturff, Microstructure property relationship in Nb–Ti–Ta, *IEEE Trans. Appl. Supercond.*, **3**(1), 1354–1357, 1993.

[55] J. Ahlbäck, D. Leroy, L. Oberly, D. Perini, J. Salminen, M. Savelainen, J. Soini and G. Spigo, Construction of a 56 mm aperture high-field twin-aperture superconducting dipole magnet, *IEEE Trans. Magn.*, **32**(4), 2097–2100, 1996.

[56] D. Leroy, L. Oberly, D. Perini, A. Siemko and G. Spigo, Design features and performance of a 10 T twin aperture model dipole for LHC, Presented at the 15th International Conference on Magnet Technology (MT15), Beijing, China, 20–24 October 1997.

[57] J.W. Ekin, Strain effects in superconducting compounds, *Adances in Cryogenic Engineering (Materials)*, **30**: 823–836, 1984.

[58] J.W. Ekin, Effect of transverse compressive stress on the critical current and upper critical field of $Nb_3Sn$, *J. Appl. Phys.*, **62**(12): 4929–4834, 1987.

[59] D.C. Larbalestier, The road to conductors of high temperature superconductors: 10 years do make a difference!, *IEEE Trans. Appl. Supercond.*, **7**(2): 90–97, 1997.

[60] M.N. Wilson, *Superconducting Magnets*, Oxford: Clarendon Press, 1983.

[61] D.P. Hampshire and H. Jones, A detailed investigation of the *E–J* characteristic and the role of defect motion within the flux-line lattice for high-current-density, high-field superconducting compounds with particular reference to data on $Nb_3Sn$ throughout its entire field–temperature phase space, *J. Phys. C: Solid State Phys.*, **20**: 3533–3552, 1987.

[62] W.H. Warnes and D.C. Larbalestier, Critical current distributions in supercondcuting composites, *Cryogenics*, **26**, 643–653, 1986.

[63] J.W. Ekin, Irregularities in Nb–Ti filament area and electric field versus current characteristics, *Cryogenics*, **27**, 603–607, 1987.

[64] C.E. Bruzek, GEC Alsthom, 3 avenue des 3 chênes, F-90018 BELFORT CEDEX, FRANCE, private communication, 1997.

[65] M. Garber, M. Suenaga, W.B. Sampson and R.L. Sabatini, Effect of $Cu_4Ti$ compound formation on the characteristics of NbTi accelerator magnet wire, *IEEE Trans. Nucl. Sci.*, **NS–32**(5): 3681–3683, 1985.

[66] A.K. Ghosh, W.B. Sampson, E. Gregory and T.S. Kreilick, Anomalous low field magnetization in fine filament NbTi conductors, *IEEE Trans. Magn.*, **MAG–23**, 1724–1727, 1987.

[67] E.W. Collings, K.R. Marken Jr., M.D. Sumption, E. Gregory and T.S. Kreilick, Magnetic studies of proximity-effect coupling in a very closely spaced fine-filament NbTi/CuMn composite superconductor, *Adances in Cryogenic Engineering (Materials)*, **36**: 231–238, 1990.

[68] K.J. Faase, P.J. Lee, J.C. McKinnel and D.C. Larbalestier, Diffusional reaction rates through the Nb wrap in SSC and other advanced multifilamentary Nb 46.5WT%Ti composites, *Adances in Cryogenic Engineering (Materials)*, **38**: 723–730, 1992.

[69] M.S. Lubell, Empirical scaling formulas for critical current and critical fields for commercial NbTi, *IEEE Trans. Magn.*, **MAG-19**(3): 754–757, 1983.

[70] L. Bottura, private communication, 1997.

[71] D.C. Larbalestier and P.J. Lee, New development in niobium titanium superconductors, *Proceedings of the 1995 IEEE Particle Accelerator Conference*, IEEE catalogue **95CH35843**: 1276–1281, 1996.

[72] L.T. Summers, M.W. Guinan, J.R. Miller and P.A. Hahn, A model for the prediction of $Nb_3Sn$ critical current as a function of field, temperature, strain and radiation damage, *IEEE Trans. Magn.*, **27**(2): 2041–2044, 1991.

[73] R. Aymar, Overview of the ITER project. In T. Haruyama, T. Mitsui and K. Yamafuji (eds.), *Proceedings of the 16th International Cryogenic Engineering Conference/ International Cryogenic Materials Conference*, London: Elsevier, 53–59 (1997).

[74] P. Bruzzone, H.H.J. ten Kate, C.R. Walters and M. Spadoni, Testing of industrial $Nb_3Sn$ strands for high field fusion magnets, *IEEE Trans. Magn.*, **30**(4): 1986–1989, 1994.

[75] J.M. Royet and R.M. Scanlan, Manufacture of keystoned flat superconducting cables for use in SSC dipoles, *IEEE Trans. Magn.*, **MAG-23**(2): 480–483, 1987.

[76] M.N. Wilson and R. Wolf, Calculation of minimum quench energies in Rutherford-type cables, *IEEE Trans. Appl. Supercond.*, **7**(2): 950–953, 1997.

[77] A.K. Ghosh, W.B. Sampson and M.N. Wilson, Minimum quench energies of Rutherford cables and single wires, *IEEE Trans. Appl. Supercond.*, **7**(2): 954–957, 1997.

[78] T. Shintomi, A. Terashima, H. Hirabayshi, M. Ikeda and H Ii, Development of large keystone angle cable for dipole magnet with ideal arch structure, *Advances in Cryogenic Engineering (Materials)*, **36**(A): 323–328, 1990.

[79] R.M. Scanlan and J.M. Royet, Recent improvements in superconducting cable for accelerator dipole magnets, *Conference Record of the 1991 IEEE Particle Accelerator Conference*, IEEE catalogue **91CH3038–7**: 2155–2157, 1991.

[80] D. Richter, J.D. Adam, J.M. Depond, D. Leroy and L.R. Oberly, DC measurements of electrical contacts between strands in superconducting cables for the LHC magnets, *IEEE Trans. Appl. Supercond.*, **7**(2): 786–792, 1997

[81] J.M. Depond, D. Leroy, L.R. Oberly and D. Richter, Examination of contacts between strands by electrical measurement and topographical analysis, *IEEE Trans. Appl. Supercond.*, **7**(2): 793–796, 1997

[82] J.D. Adam, D. Leroy, L.R. Oberly, D. Richter, M.N. Wilson, R. Wolf, H. Higley, A.D. McInturff, R.M. Scanlan, A. Nijhuis, H.H.J. ten Kate and S. Wessel, Rutherford cables with anisotropic transverse resistance, *IEEE Trans. Appl. Supercond.*, **7**(2): 958–961, 1997.

[83] M. Garber, W.B. Sampson and M.J. Tannenbaum, Critical current measurements on superconducting cables, *IEEE Trans. Mag.*, **MAG–19**(3): 720–723, 1983.

[84] H. Boschman, A.P. Verweij, S. Wessel, H.H.J. ten Kate and L.J.M. van de Klundert, The effect of transverse loads up to 300 MPa on the critical currents of $Nb_3Sn$ cables, *IEEE Trans. Mag.*, **27**(2): 1831–1834, 1990.

[85] H.H.J. ten Kate, H. Weijers and J.M. van Ort, Critical current degradation in $Nb_3Sn$ cables under tansverse pressure, *IEEE Trans. Appl. Supercond.*, **3**(1): 1334–1337, 1993.

[86] R.A. Haarman and K.D. Williamson, Jr., Electrical breakdown and tracking characteristics of pulsed high voltages in cryogenic helium and nitrogen, *Advances in Cryogenic Engineering*, **21**: 102–108, 1975.

[87] P. Védrine, J.M. Rifflet, J. Perot, B. Gallet, C. Lyraud, P. Giovannoni, F. Le Coz, N. Siegel and T. Tortschanoff, Mechanical tests on the prototype LHC lattice quadrupole, *IEEE Trans. Magn.*, **30**(4): 2475–2478, 1994.

[88] M. Anerella, A.K. Ghosh, E. Kelly, J. Schmalzle, E. Willen, J. Fraivillig, J. Ochsner and D.J. Parish, Improved cable insulation for superconducting magnets, *Proceedings of the 1993 Particle Accelerator Conference*, IEEE catalogue **93CH3279–7**: 2790–2792, 1993.

[89] P. Bruzzone, K. Nylund, and W.J. Muster, Electrical insulation system for superconducting magnets according to the wind and react technique, *Adv. Cryog. Eng.*, **36**: 999–1006, 1990.

[90] G.H. Morgan, Shaping of magnetic fields in beam transport magnets. In M. Month and M. Dienes (eds.), *The Physics of Particle Accelerators*, AIP Conference Proceedings **249**(2): 1242–1261, 1992.

[91] R.C. Gupta, S.A. Kahn and G.H. Morgan, SSC 50 mm dipole cross section. In J. Nonte (ed.), *Supercollider 3*, New York: Plenum Press, 587–599, 1991.

[92] A. Devred and T. Ogitsu, Ramp-rate sensitivity of SSC dipole magnet prototypes. In S.I. Kurokawa, M. Month and S. Turner (eds.), *Frontiers of Accelerator Technology*, Singapore: World Scientific, 184–308, 1996.

[93] R.C. Gupta, A common coil design for high field 2-in-1 accelerator magnets, *Conference Record of the 1997 IEEE Particle Accelerator Conference* (to be published by IEEE).

[94] J.M. Cook, Strain energy minimization in SSC magnet winding, *IEEE Trans. Mag.*, **27**(2): 1976–1980, 1991.

[95] J.S. Brandt, N.W. Bartlett, R.C. Bossert, J.A. Carson, J.J. Konc, G.C. Lee, J.M. Cook, S. Caspi, M.A. Gordon and F. Nobrega, Coil end design for the SSC collider dipole magnet, *Conference Record of the 1991 IEEE Particle Accelerator Conference*, IEEE catalogue **91CH3038–7**: 2182–2184, 1991.

[96] T. Garavaglia, K. Kauffmann and R. Stiening, Application of the SSCRTK numerical simulation program to the evaluation of the SSC magnet aperture. In M. MacAshan (ed.), *Supercollider 2*, New York: Plenum Press, 59–76, 1990.

[97] T. Ogitsu and A. Devred, Influence of azimuthal coil size variations on magnetic field harmonics of superconducting particle accelerator magnets, *Rev. Sci. Instrum.*, **65**(6): 1998–2005 (1994).

[98] C.P. Bean, Magnetization of high-field superconductors, *Review of Modern Physics*, **36**(1), pp. 31–39 (1964).

[99] H. Brück, R. Meinke, F. Müller and P. Schmüser, Field distortions from persistent magnetization currents in the superconducting HERA magnets, *Z. Phys. C – Particles and Fields*, **44**: 385–392 (1989).

[100] R.W. Hanft, B.C. Brown, D.A. Herrup, M.J. Lamm, A.D. McInturff and M.J. Syphers, Studies of time dependent field distorsions from magnetization currents in Tevatron superconducting dipole magnets, *IEEE Trans. Magn.*, **25**(2): 1647–1651, 1989.

[101] A. Devred, J. DiMarco, J. Kuzminski, R. Stiening, J. Tompkins, Y. Yu, H. Zheng, T. Ogitsu, R. Hanft, P.O. Mazur, D. Orris and T. Peterson, Time decay measurements of the sextupole component of the magnetic field in a 4-cm aperture, 17-m-long SSC dipole magnet prototype, *Conference Record of the 1991 IEEE Particle Accelerator Conference*, IEEE catalogue **91CH3038–7**: 2480–2482, 1991.

[102] F. Willeke and F. Zimmermann, The impact of persistent current field errors on the stability of the proton beam in the HERA proton ring, *Conference Record of the 1991 IEEE Particle Accelerator Conference*, IEEE catalogue **91CH3038–7**: 2483–2487, 1991.

[103] P. Schmüser, "Properties and Practical Performance of SC Magnets in Accelerators," *Proc. of III-rd European Part. Acc. Conf.*, Berlin, Germany, pp. 284–288 (March 24–28, 1992).

[104] L. Bottura, L. Walckiers and R. Wolf, Field errors decay and "snap-back" in LHC model dipoles, *IEEE Trans. Appl. Supercond.*, **7**(2): 602–605, 1997.

[105] P.W. Anderson, Flux creep in hard superconductors, *Phys. Rev. Letters*, **9**(7): 309–311, 1962.

[106] T. Ogitsu, A. Devred and V. Kovachev, Influence of inter-strand coupling current on field quality of superconducting accelerator magnets, *Particle Accelerators*, **57**: 215–235, 1997.

[107] H. Brück, D. Gall, J. Krzywinski, R. Meinke, H. Preissner, M. Halemeyer, P. Schmüser, C. Stolzenburg, R. Stiening, D. ter Avest, L.J.M. van de Klundert, Observation of a periodic pattern in the persistent-current fields of the superconducting HERA magnets, *Conference Record of the 1991 IEEE Particle Accelerator Conference*, IEEE catalogue **91CH3038–7**: 2149–2151, 1991.

[108] A.K. Ghosh, K.E. Robins and W.B. Sampson, Axial variations in the magnetic field of superconducting dipoles and quadrupoles, *Proceedings of the 1993 Particle Accelerator Conference*, IEEE catalogue **93CH3279–7**: 2742–2743, 1993.

[109] A. Akhmetov, A. Devred, R. Schermer and R. Mints, Current loop decay in Rutherford-type cables. In P. Hale (ed.), *Supercollider 5*, New York: Plenum Press, 443–446 (1994).

[110] L. Krempanski and C. Schmidt, Influence of a longitudinal variation of dB/dt on the magnetic field distribution of superconducting accelerator magnets, *Appl. Phys. Lett.*, **66**(12): 1545–1547, 1995.

[111] A.P. Verweij, Boundary-induced coupling currents in a 1.3 m Rutherford-type cable due to a locally applied field change, *IEEE Trans. Appl. Supercond.*, **7**(2): 270–273, 1997.

[112] L. Bottura, L. Walckiers and Z. Ang, Experimental evidence of boundary induced coupling currents in LHC prototypes, *IEEE Trans. Appl. Supercond.*, **7**(2): 801–804, 1997.

[113] R. Stiening, A possible mechanism for enhanced persistent current sextupole decay in SSC dipoles, 1991 (unpublished).

[114] A. Devred, T. Bush, R. Coombes, J. DiMarco, C. Goodzeit, J. Kuzminski, M. Puglisi, P. Radusewicz, P. Sanger, R. Schermer, G. Spigo, J. Tompkins, J. Turner, Z. Wolf, Y. Yu, H. Zheng, T. Ogitsu, M. Anerella, J. Cottingham, G. Ganetis, M. Garber, A. Ghosh, A. Greene, R. Gupta, J. Herrera, S. Kahn, E. Kelly, A. Meade, G. Morgan, J. Muratore, A. Prodell, M. Rehak, E.P. Rohrer, W. Sampson, R. Shutt, P. Thompson, P. Wanderer, E. Willen, M. Bleadon, R. Hanft, M. Kuchnir, P. Mantsch, P.O. Mazur, D. Orris, T. Peterson, J. Strait, J. Royet, R. Scanlan and C. Taylor, About the mechanics of SSC dipole magnet prototypes. In M. Month and M. Dienes (eds.), *The Pysics of Particle Accelerators*, AIP Conference Proceedings **249**(2): 1309–1374, 1992.

[115] T. Ogitsu, K. Tsuchiya and A. Devred, Investigation of wire motion in superconducting magnets, *IEEE Trans. Magn.*, **27**(2): 2132–2135, 1991.

[116] D. Perini, N. Galante, J. Gilquin, G. Patti and R. Perin, Measurements of the resistance to stress cycling at 4.2 K of LHC dipole collars, *IEEE Trans. Magn.*, **30**(4): 1754–1757, 1994.

[117] D. Leroy, R. Perin, D. Perini and Y. Yamamoto, Structural analysis of the LHC 10 T twin-aperture dipole. In T. Sekiguchi and S. Shimamoto (eds.), *Proceedings of the 11-th International Conference on Magnet Technology*, London: Elsevier Applied Science, 159–164 (1990).

[118] E. Acerbi, M. Bona, D. Leroy, R. Perin and L. Rossi, Development and fabrication of the first 10 m long superconducting dipole prototype for the LHC, *IEEE Trans. Magn.*, **30**(4): 1793–1796, 1994.

[119] G. Spigo, Preliminary assessment of the mechanical strength of a dipole with aluminum collars, vertically split yoke and aluminum bars to control the gap from room to working temperatures, 1990 (unpublished).

[120] D. Dell'Orco, S. Caspi, J. O'Neill, A. Lieztke, R. Scanlan, C.E. Taylor and A. Wandesforde, A 50 mm bore superconducting dipole with a unique iron yoke structure, *IEEE Trans. Appl. Supercond.*, **3**(1): 637–641, 1993.

[121] J. Strait, B.C. Brown, R. Hanft, M. Kuchnir, M. Lamm, R. Lundy, P. Mantsch, P.O. Mazur, A. McInturff, J.R. Orr, J.G. Cottingham, P. Dahl, G. Ganetis, M. Garber, A. Ghosh, C. Goodzeit, A. Greene, J. Herrera, S. Kahn, E. Kelly, G. Morgan, A. Prodell, W. Sampson, W. Schneider, R. Shutt, P. Thompson, P. Wanderer, E. Willen, S. Caspi, W. Gilbert, R. Meuser, C. Peters, J. Rechen, R. Royer, R. Scanlan, C. Taylor, J. Zbasnik, M. Chapman, A. Devred, J. Kaugerts, J. Peoples, J. Tompkins and R. Schermer, Tests of full scale SSC R&D dipole magnets, *IEEE Trans. Magn.*, **25**(2): 1455–1458, 1989.

[122] S.W. Van Sciver, *Helium Cryogenics*, New York: Plenum Press, 1986.

[123] Ph. Lebrun, Cryogenic systems for accelerators. In S.I. Kurokawa, M. Month and S. Turner (eds.), *Frontiers of Accelerator Technology*, Singapore: World Scientific, 681–700, 1996.

[124] C.H. Rode, Tevatron Cryogenic System. In F.T. Cole, R. Donaldson (eds.), *Proceedings of the 12th International Conference on High Energy Accelerators*, Batavia, Illinois: Fermi National Accelerator Laboratory, 529–535, 1983.

[125] T.J. Peterson, The nature of the helium flow in Fermilab's Tevatron magnets, *Cryogenics*, **37**(11), pp. 727–732, 1997.

[126] H.R. Barton Jr., M. Clausen, G. Horlitz, G. Knust and H. Lierl, The refrigeration system for the superconducting proton ring of the electron proton collider HERA, *Advances in Cryogenic Engineering*, **31**: 635–645, 1986.

[127] D.P. Brown, R.I. Loutitt, C. Rode and P.C. VanderArend, The SSC cryogenic system, *Advances in Cryogenic Engineering*, **31**: 57–62, 1986.

[128] M.S. McAshan, SSC refrigeration system design studies. In M. McAshan (ed.), *Supercollider 1*, New York: Plenum Press, 287–300, 1989.

[129] D.R. Tiley and J. Tilley, *Superfluidity and superconductivity*, 3rd ed., Bristol: Adam Hilger, 1990.

[130] Ph. Lebrun, Superfluid helium cryogenics for the large hadron collider project at CERN, *Cryogenics*, **34** ICEC Supplement: 1–8, 1994.

[131] G. Claudet and R. Aymar, Tore supra and He II cooling of superconducting magnets, *Advances in Cryogenic Engineering*, **35**(A): 55–67, 1990.

[132] W. Frost (ed.), *Heat Transfer at Low Temperatures*, New York: Plenum Press, 1975.

[133] T.H. Nicol, Cryostat design for the superconducting super collider. In M. Month and M. Dienes (eds.), *The Physics of Particle Accelerators*, AIP Conference Proceedings **249**(2): 1230–1241, 1992.

[134] J. Strait, M. Bleadon, B.C. Brown, R. Hanft, M. Kuchnir, M. Lamm, P. Mantsch, P.O. Mazur, D. Orris, J. Peoples, G. Tool, J.G. Cottingham, P. Dahl, G. Ganetis, M. Garber, A.K. Ghosh, C. Goodzeit, A. Greene, J. Herrera, S. Kahn, E. Kelly, G. Morgan, J. Muratore, A. Prodell, W. Sampson, R. Shutt, P. Thompson, P. Wanderer, E. Willen, M. Chapman, J. Cortella, A. Desportes, A. Devred, J. Kaugerts, T. Kirk, R. Meuser, K. Mirk, R. Schermer, J. Turner, J.C. Tompkins, S. Caspi, W. Gilbert, C. Peters, J. Rechen, J.M. Royer, R. Scanlan, C. Taylor and J. Zbasnik, Full length SSC R&D dipole magnet test results, *Conference Record of the 1991 IEEE Particle Accelerator Conference*, IEEE catalogue **91CH3038-7**: 530–532, 1989.

[135] P. Wanderer, M. Anerella, G. Ganetis, M. Garber, A.K. Ghosh, A. Greene, R. Gupta, A. Jain, S. Kahn, E. Kelly, G. Morgan, J. Muratore, A. Prodell, M. Rehak, E.P. Rohrer, W. Sampson, R. Shutt, R. Thomas, P. Thompson, E. Willen, A. Akhmetov, T. Bush, W.D. Capone II, R. Coombes, A. Devred, J. DiMarco, C. Goodzeit, J. Krzywinski, J. Kuzminski, W. Nah, T. Ogitsu, P. Radusewicz, R. Schermer, R. Stiening, J.C. Tompkins, M. Wake, J. Zbasnik, Y. Zhao, H. Zheng, Partial lifetime test of an SSC collider dipole, *IEEE Trans. Magn.*, **30**(4): 1738–1741, 1994.

[136] T. Schneider and P. Turowski, Critical current degradation of a NbTi-multifilament conductor due to heat treatment, *IEEE Trans. Magn.*, **30**(4): 2391–2394, 1994.

[137] A. Devred, M. Chapman, J. Cortella, A. Desportes, J. DiMarco, J. Kaugerts, R. Schermer, J.C. Tompkins, J. Turner, J.G. Cottingham, P. Dahl, G. Ganetis, M. Garber, A. Ghosh, C. Goodzeit, A. Greene, J. Herrera, S. Kahn, E. Kelly, G. Morgan, A. Prodell, E.P. Rohrer, W. Sampson, R. Shutt, P. Thompson, P. Wanderer, E. Willen, M. Bleadon, B.C. Brown, R. Hanft, M. Kuchnir, M. Lamm, P. Mantsch, P.O. Mazur, D. Orris, J. Peoples, J. Strait, G. Tool, S. Caspi, W. Gilbert, C. Peters, J. Rechen, J. Royer, R. Scanlan, C. Taylor and J. Zbasnik, Investigation of heater-induced quenches in a full-length SSC R&D dipole. In T. Sekiguchi and S. Shimamoto (eds.), *Proceedings of the 11-th International Conference on Magnet Technology*, London: Elsevier Applied Science, 91–95 (1990).

[138] A. Devred, M. Chapman, J. Cortella, A. Desportes, J. DiMarco, J. Kaugerts, R. Schermer, J.C. Tompkins, J. Turner, J.G. Cottingham, P. Dahl, G. Ganetis, M. Garber, A. Ghosh, C. Goodzeit, A. Greene, J. Herrera, S. Kahn, E. Kelly, G. Morgan, A. Prodell, E.P. Rohrer, W. Sampson, R. Shutt, P. Thompson, P. Wanderer, E. Willen, M. Bleadon, B.C. Brown, R. Hanft, M. Kuchnir, M. Lamm, P. Mantsch, P.O. Mazur, D. Orris, J. Peoples, J. Strait, G. Tool, S. Caspi, W. Gilbert, C. Peters, J. Rechen, J. Royer, R. Scanlan, C. Taylor and J. Zbasnik, Quench characteristics of full-length SSC R&D dipole magnets, *Advances in Cryogenic Engineering*, **35**(A): 599–608, 1990.

[139] L. Coull, D. Hagedorn, V. Remondino and F. Rodriguez-Mateos, LHC magnet quench protection system, *IEEE Trans. Magn.*, **30**(4): 1742–1745, 1994.

[140] R. Stiening, R. Flora, R. Lauckner and G. Tool, A superconducting synchrotron power supply and quench protection scheme, *IEEE Trans. Magn.*, **MAG–15**(1): 670–672, 1979.

[141] K. Koepke, C. Rode, G. Tool, R. Flora, J. Jölstlein, J. Saarivirta and M. Kuchnir, Two cell doubler system test, *IEEE Trans. Magn.*, **MAG–17**(1): 713–715, 1981.

[142] W. Burgett, M. Christianson, R. Coombes, T. Dombeck, J. Gannon, D. Haenni, P. Kraushaar, M. Levin, M. McAshan, A. McInturff, G. Mulholland, D. Murray, W. Robinson, T. Savord, R. Smellie, F. Spinos, G. Tool, J. Weisend II and J. Zatopek, Full-power test of a string of magnets comprising a half-cell of the superconducting super collider, *Part. Accel.*, **43**: 41–75, 1993.

[143] F. Rodriguez-Mateos, L. Coull, K. Dahlerup-Petersen, D. Hagedorn, G. Krainz and A. Rijllart, Electrical performance of a string of magnets representing a half-cell of the LHC machine, *IEEE Trans. Magn.*, **32**(4): 2105–2108, 1996.

## TABLE CAPTIONS

Table 1. Selected parameters of major superconducting particle accelerators.

Table 2. Integrated thermal expansion coefficients between 4.2 K and room temperature ($10^{-3}$ m/m).

Table 1. Selected parameters of major superconducting particle accelerators.

| Laboratory | FNAL | DESY | IHEP | SSCL | BNL | CERN |
|---|---|---|---|---|---|---|
| Name | Tevatron | HERA | UNK | SSC | RHIC | LHC |
| Circumference (km) | 6.3 | 6.3 | 21 | 87 | 3.8 | 27 |
| Particle type | $p\bar{p}$ | ep | pp | pp | heavy ions | pp |
| Energy/beam (TeV) | 0.9 | 0.82 | 3 | 20 | up to 0.1[a)] | 7 |
| Number of dipoles | 774 | 416 | 2168 | 7944 | 264 | 1232[b)] |
| Aperture (mm) | 76.2 | 75 | 70 | 50 | 80 | 56 |
| Magnetic length (m) | 6.1 | 8.8 | 5.8 | 15 | 9.7 | 14.2 |
| Field (T) | 4 | 4.68 | 5.0 | 6.79 | 3.4 | 8.36 |
| Number of quadrupoles | 216 | 256 | 322 | 1696 | 276 | 386[b)] |
| Aperture (mm) | 88.9 | 75 | 70 | 50 | 80 | 56 |
| Magnetic length[c)] (m) | 1.7 | 1.9 | 3.0 | 5.7 | 1.1 | 3.1 |
| GradientT/m) | 76 | 91.2 | 97 | 194 | 71 | 223 |
| Commissioning | 1983 | 1990 | undecided | cancelled | 1999 | 2005 |

a) per unit of atomic mass
b) two-in-one magnets
c) quadrupoles come in several lengths

Table 2. Integrated thermal expansion coefficients between 4.2 K and room temperature ($10^{-3}$ m/m).

| | |
|---|---|
| Low carbon steel | 2.0 |
| Stainless steel (304/316) | 2.9 |
| Copper (OFHC) | 3.1 |
| Aluminum | 4.2 |
| Insulated cable (polyimide/glass) | 5.1[a)] |
| Insulated cable (all-polyimide) | 5.6[a)] |

[a)] transverse direction; SSC inner cable.

## FIGURE CAPTIONS

Figure 1. Cross-sectional views of superconducting dipole magnets for large particle accelerators [39]: (a) Tevatron, (b) HERA, (c) SSC, (d) RHIC and (e) LHC.

Figure 2. Transition from the superconducting to the normal resistive state of a multifilamentary composite wire: (a) voltage-current curve and (b) voltage-current curve replotted in logarithmic scales. Data correspond to a 9-mm long sample of $Nb_3Sn$ wire measured at 4.2 K and 7.5 T.

Figure 3. Cross-sectional views of multifilamentary composite wires: (a) NbTi wire for LHC and (b) unreacted ITER-type $Nb_3Sn$ wire prepared by the internal-tin process [64].

Figure 4. Rutherford-type cable for particle accelerator magnets: (a) perspective view and (b) cross-sectional view.

Figure 5. Representations of a single current-line: (a) in free space and (b) inside a circular iron yoke.

Figure 6. Examples of current-line distributions with selected symmetries: (a) quadruplet of current-lines with an even symmetry about the $x$-axis and an odd symmetry about the $y$-axis and (b) octuplet of current-lines with even symmetries with respect to the $x$- and $y$-axes and odd symmetries with respect to the first and second bisectors.

Figure 7. Examples of cylindrical current shells with selected symmetries: (a) shell with dipole symmetry and (b) shell with quadrupole symmetry.

Figure 8. Mirror image of a cylindrical current shell within a circular iron yoke.

Figure 9. Cylindrical current shell with dipole symmetry and angular wedges.

Figure 10. Conductor and Lorentz force distributions in a quadrant of a 50-mm-aperture SSC dipole magnet coil [91].

Figure 11. Conceptual block design developed at BNL for a high field, twin-aperture dipole magnet [93].

Figure 12. Perspective view of a saddle-shape coil assembly for a dipole magnet.

Figure 13. Measurements of normal sextupole coefficient ($b_3$) as a function of current in the central part of a SSC dipole magnet showing the hysteresis resulting from superconductor magnetization and the distortions at high currents resulting from iron saturation.

Figure 14. Effects of interstrand coupling currents on multipole field coefficients as measured as a function of ramp rate in the central part of a SSC dipole magnet [92]: (a) skew sextupole field coefficient ($A_3$) and (b) normal sextupole field coefficient ($B_3$). The transport-current contribution is subtracted from the data.

Figure 15. SSC dipole magnet cross-sections [20]: (a) BNL-style with horizontally-split yoke and (b) FNAL-style with vertically-split yoke.

Figure 16. Pressure-Temperature phase diagram of helium [123].

Figure 17. Selected testing results from 4-cm-aperture, 17-m-long SSC dipole magnet prototype DD0017: (a) current at quench versus quench number and (b) current at quench versus temperature at quench.

Figure 18. Comparison between quench plateau currents and estimated short sample current limits on selected 5-cm-aperture, 15-m-long SSC dipole magnet prototypes.

Figure 19. Ramp rate sensitivity of selected 5-cm-aperture, 15-m-long SSC dipole magnet prototypes: (a) Type A and (b) Type (b). (The magnets are grouped according to the manufacturer and the production batch of their inner cable strands.)

Figure 20. Voltage distribution in a quenching magnet. The total voltage across the magnet is assumed to be nil and the developing resistance is assumed to be concentrated near two third of the magnet length [4].

Figure 21. Electrical circuit of a quenching magnet in a magnet string [4].

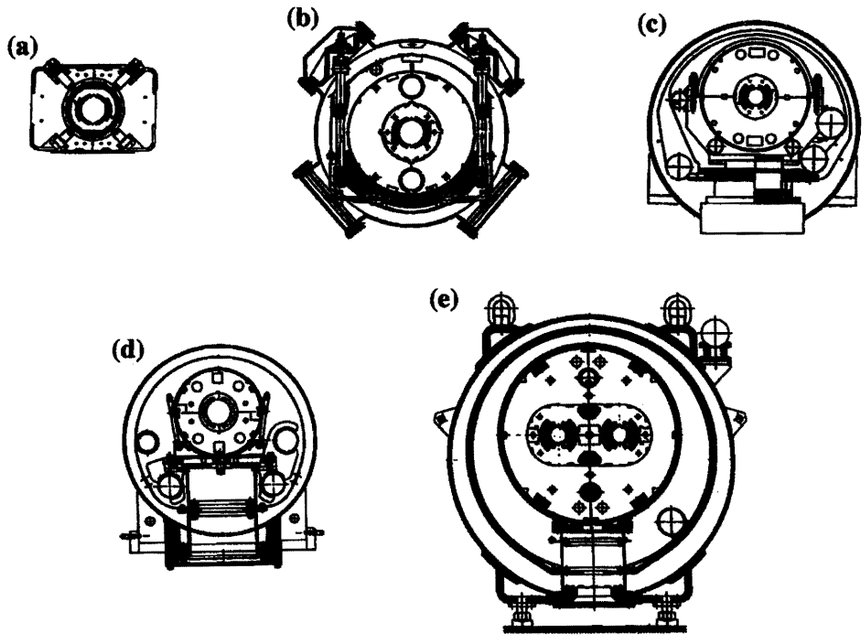


Figure 1. Cross-sectional views of superconducting dipole magnets for large particle accelerators [39]: (a) Tevatron, (b) HERA, (c) SSC, (d) RHIC and (e) LHC.

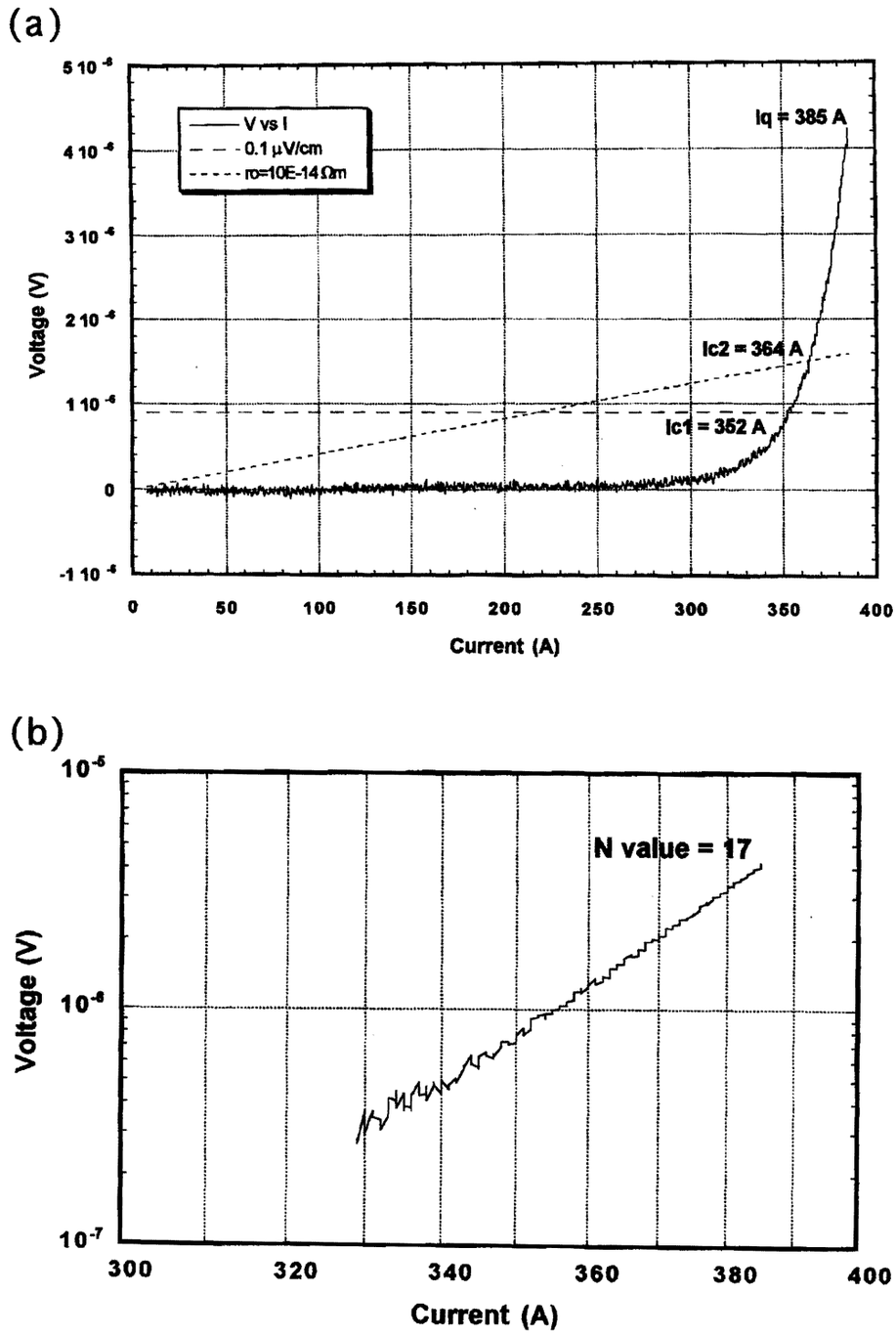


Figure 2. Transition from the superconducting to the normal resistive state of a multifilamentary composite wire: (a) voltage-current curve and (b) voltage-current curve replotted in logarithmic scales. Data correspond to a 9-mm long sample of $Nb_3Sn$ wire measured at 4.2 K and 7.5 T.

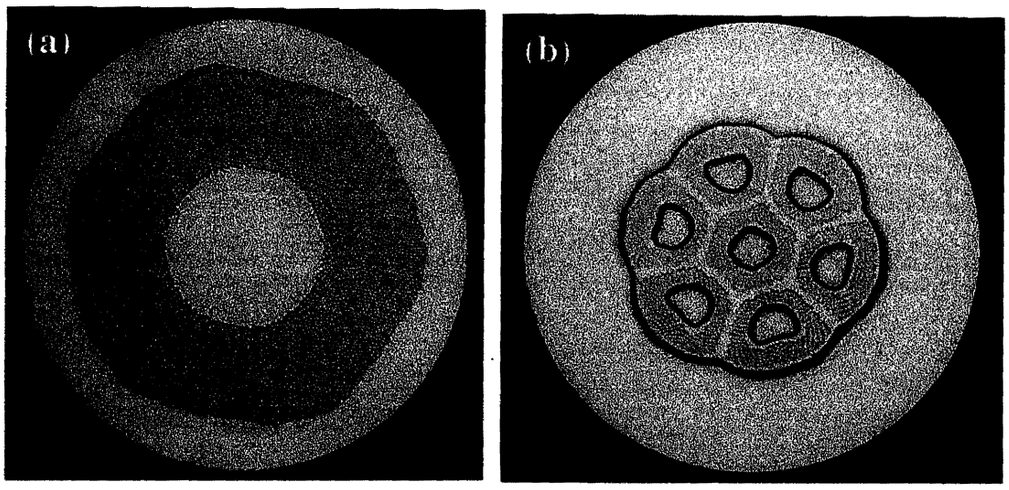


Figure 3. Cross-sectional views of multifilamentary composite wires: (a) NbTi wire for LHC and (b) unreacted ITER-type $Nb_3Sn$ wire prepared by the internal-tin process [64].

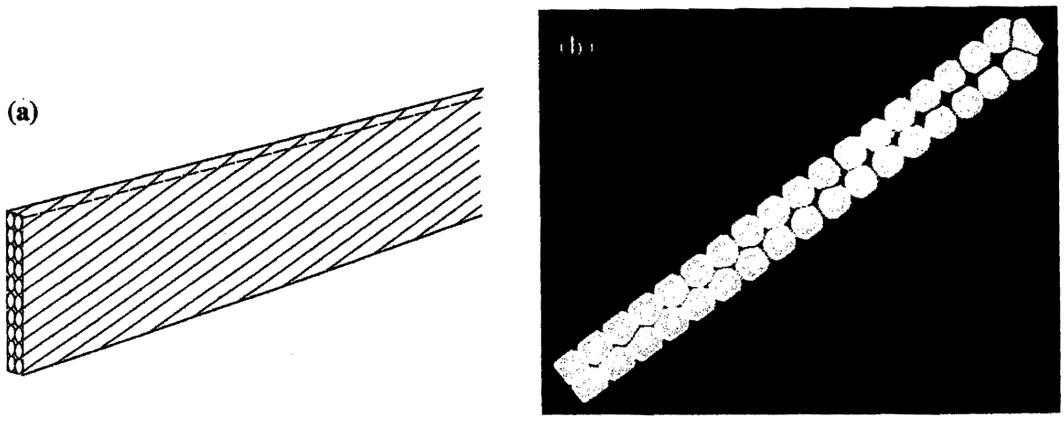


Figure 4. Rutherford-type cable for particle accelerator magnets: (a) perspective view and (b) cross-sectionnal view.

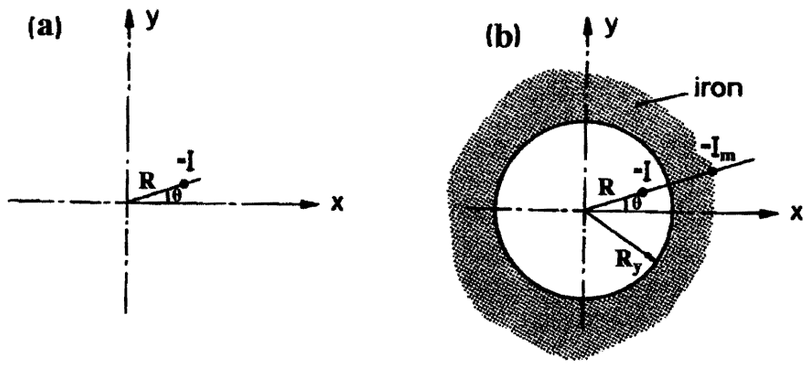


Figure 5. Representations of a single current-line: (a) in a vacuum and (b) inside a circular iron yoke.

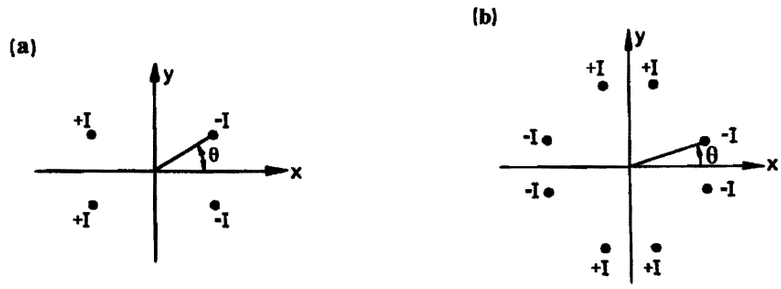


Figure 6. Examples of current-line distributions with selected symmetries (a) quadruplet of current-lines with an even symmetry about the $x$-axis and an odd symmetry about the $y$-axis and (b) octuplet of current-lines with even symmetries with respect to the $x$- and $y$-axes and odd symmetries with respect to the first and second bisectors.

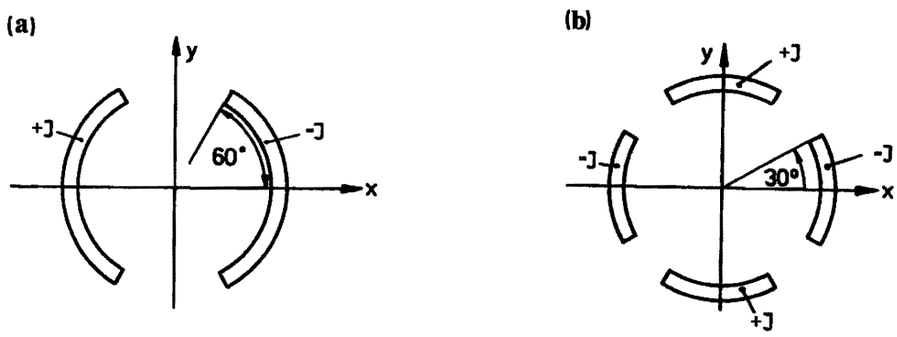


Figure 7. Examples of cylindrical current shells with selected symmetries: (a) shell with dipole symmetry and (b) shell with quadrupole symmetry.

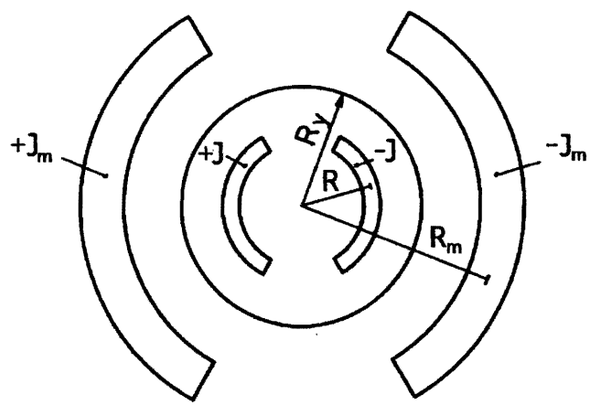


Figure 8. Mirror image of a cylindrical current shell within a circular iron yoke.

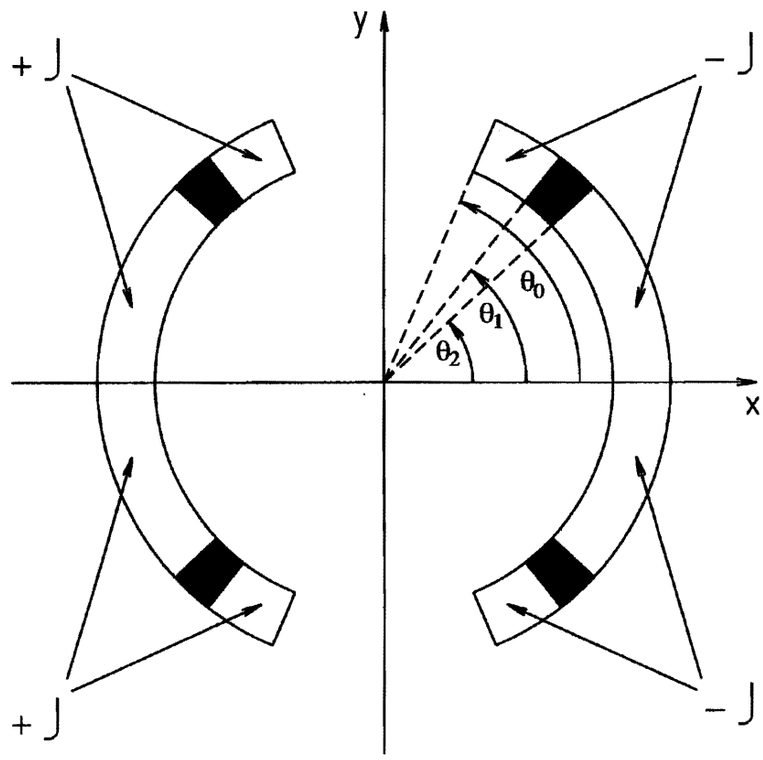


Figure 9. Cylindrical current shell with dipole symmetry and angular wedges.

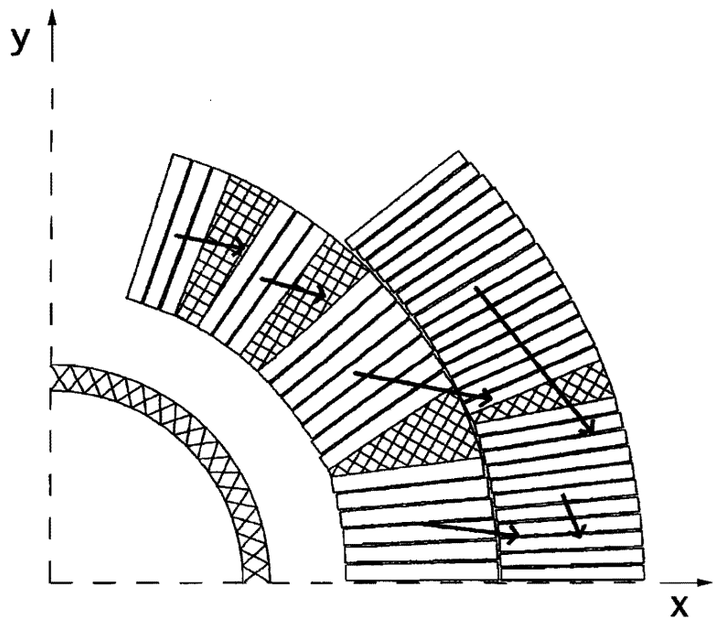


Figure 10. Conductor distribution in a quadrant of a 50-mm-aperture SSC dipole magnet coil [91].

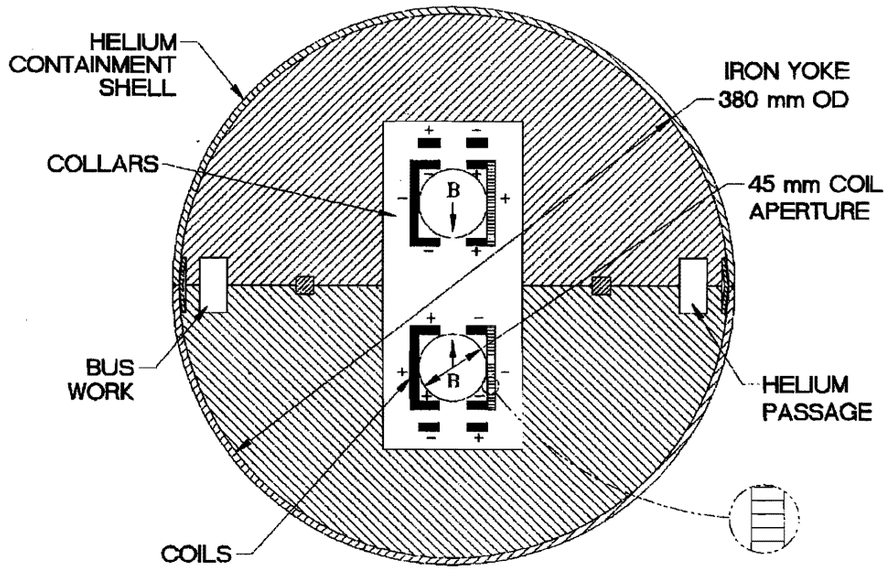


Figure 11. Conceptual block design developed at BNL for a high field, twin-aperture dipole magnet [93].

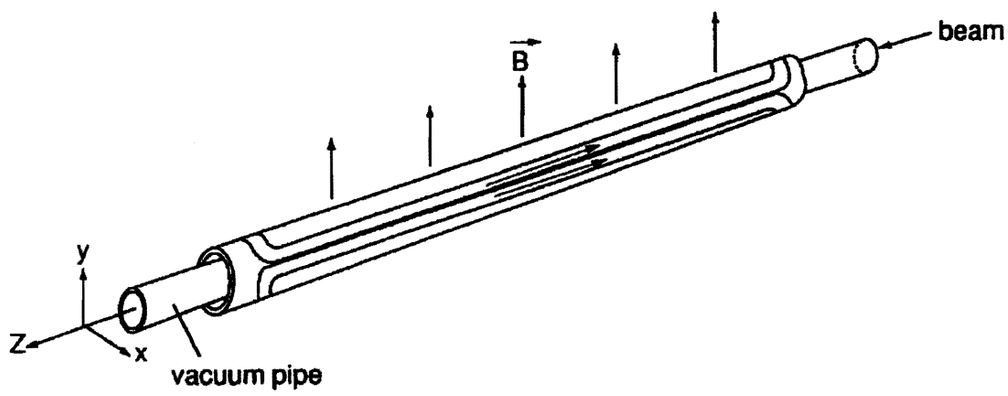


Figure 12. Perspective view of a saddle-shape coil assembly for a dipole magnet.

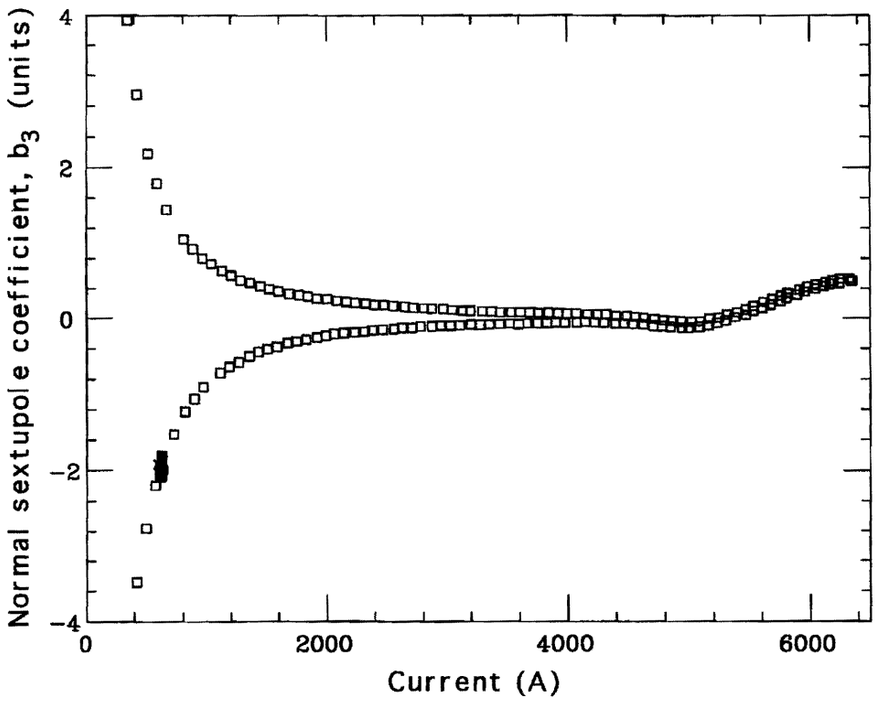


Figure 13. Measurements of normal sextupole coefficient ($b_3$) as a function of current in the central part of a SSC dipole magnet showing the hyteresis resulting from superconductor magnetization and the distorsions at high currents resulting from iron saturation.

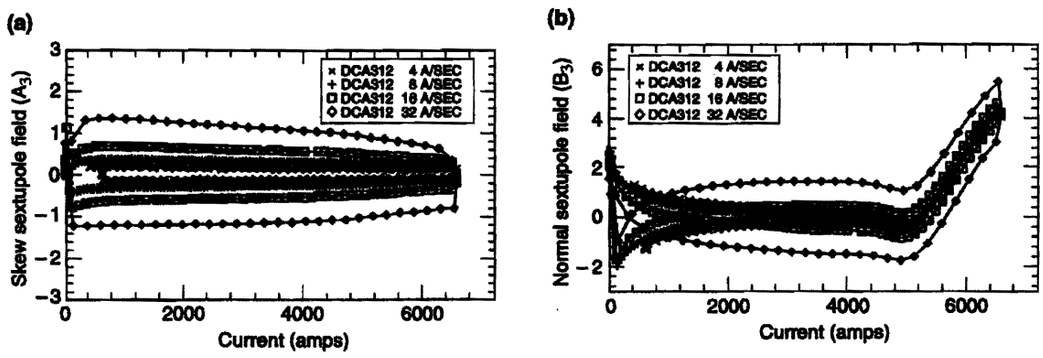


Figure 14. Effects of interstrand coupling currents on multipole field coefficients as measured as a function of ramp rate in the central part of a SSC dipole magnet [92]: (a) skew sextupole field coefficient ($A_3$) and (b) normal sextupole field coefficient ($B_3$). The transport-current contribution is substracted from the data.

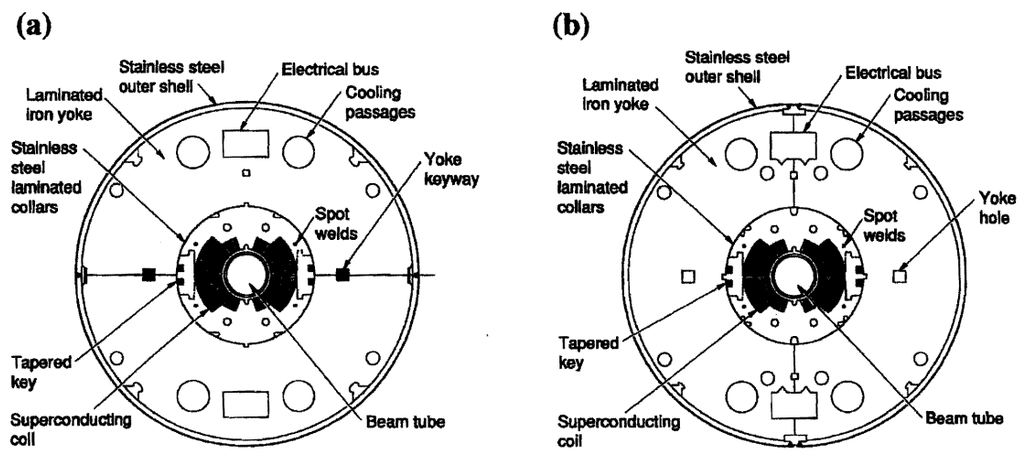


Figure 15. SSC dipole magnet cross-sections [20]: (a) BNL-style with horizontally-split yoke and (b) FNAL-style with vertically-split yoke.

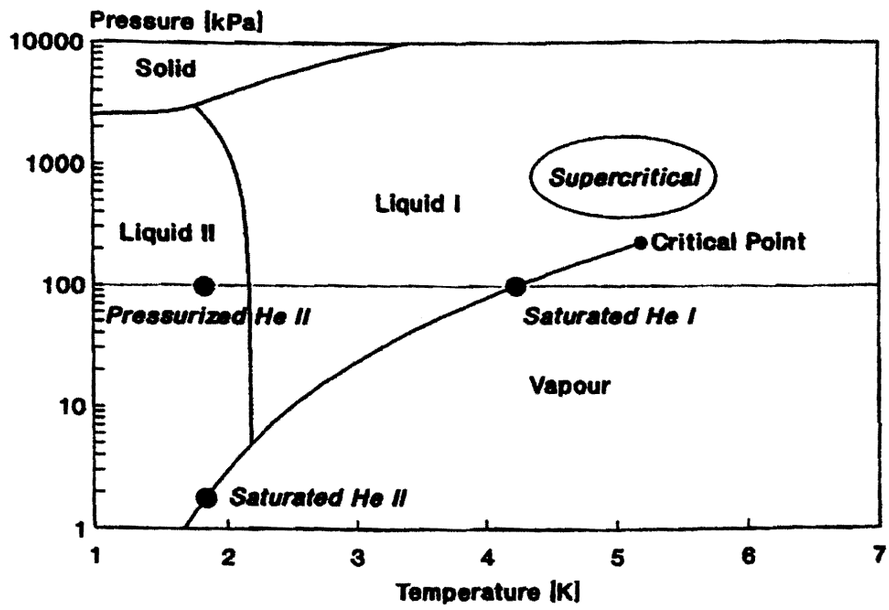


Figure 16. Pressure-Temperature phase diagram of helium [123].

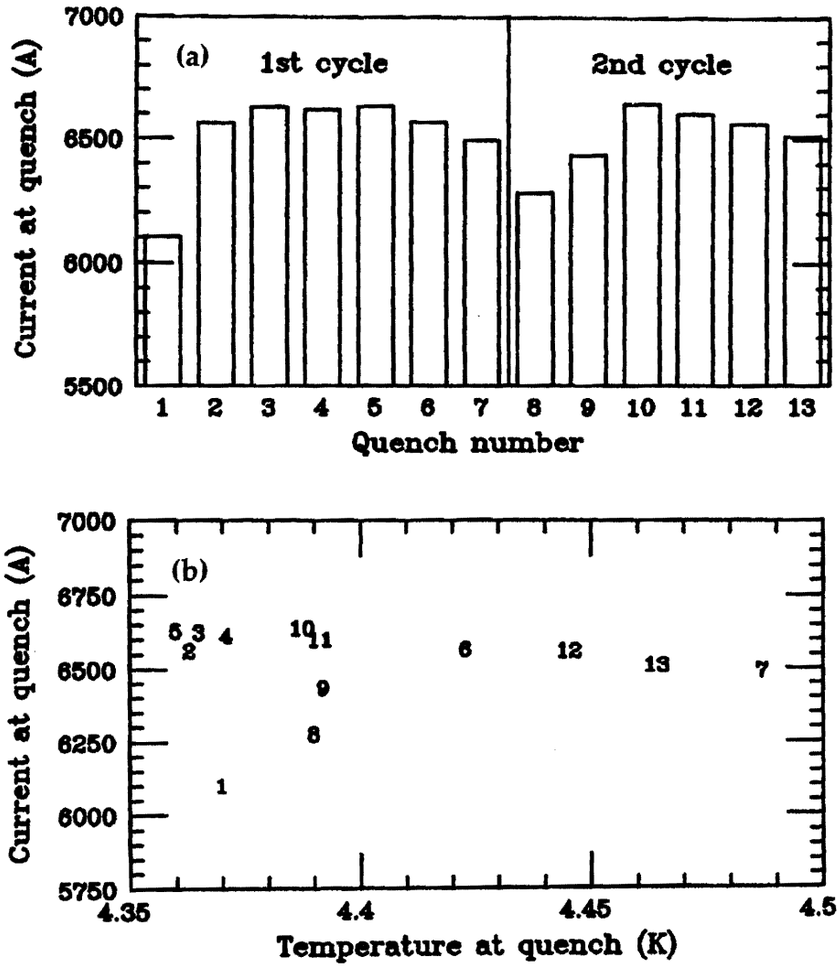


Figure 17. Selected testing results from 4-cm-aperture, 17-m-long SSC dipole magnet prototype DD0017: (a) current at quench versus quench number and (b) current at quench versus temperature at quench.

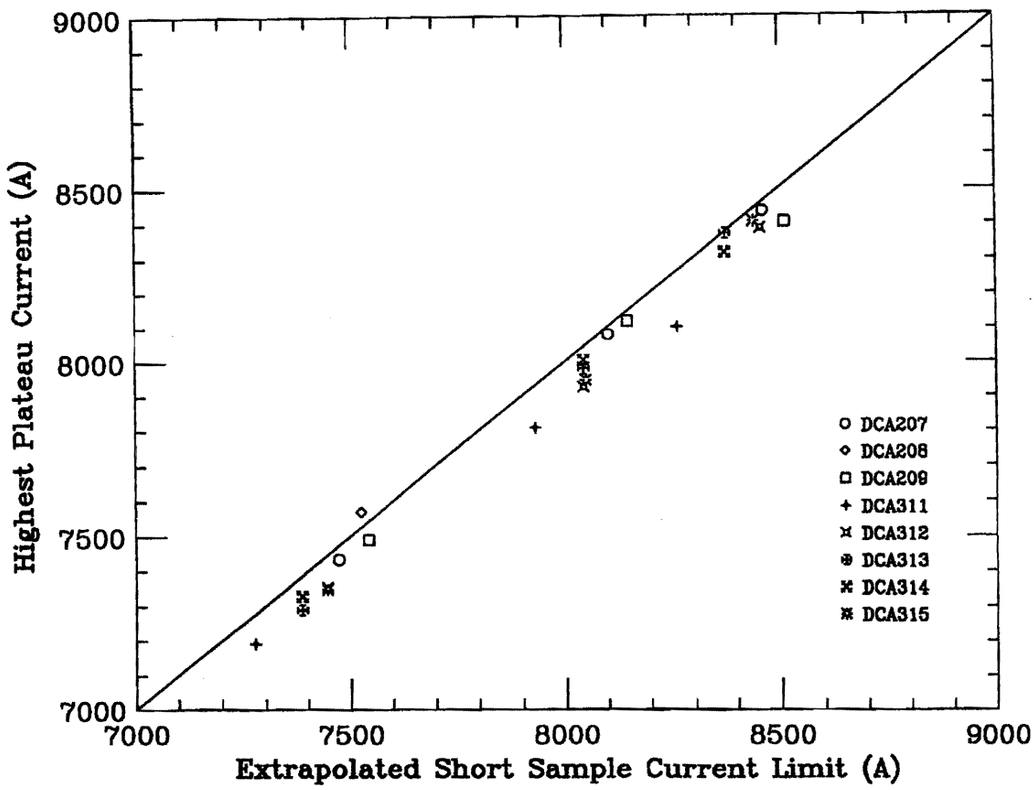


Figure 18. Comparison between quench plateau current and estimated short sample current limit on selected 5-cm-aperture, 15-m-long SSC dipole magnet prototypes.

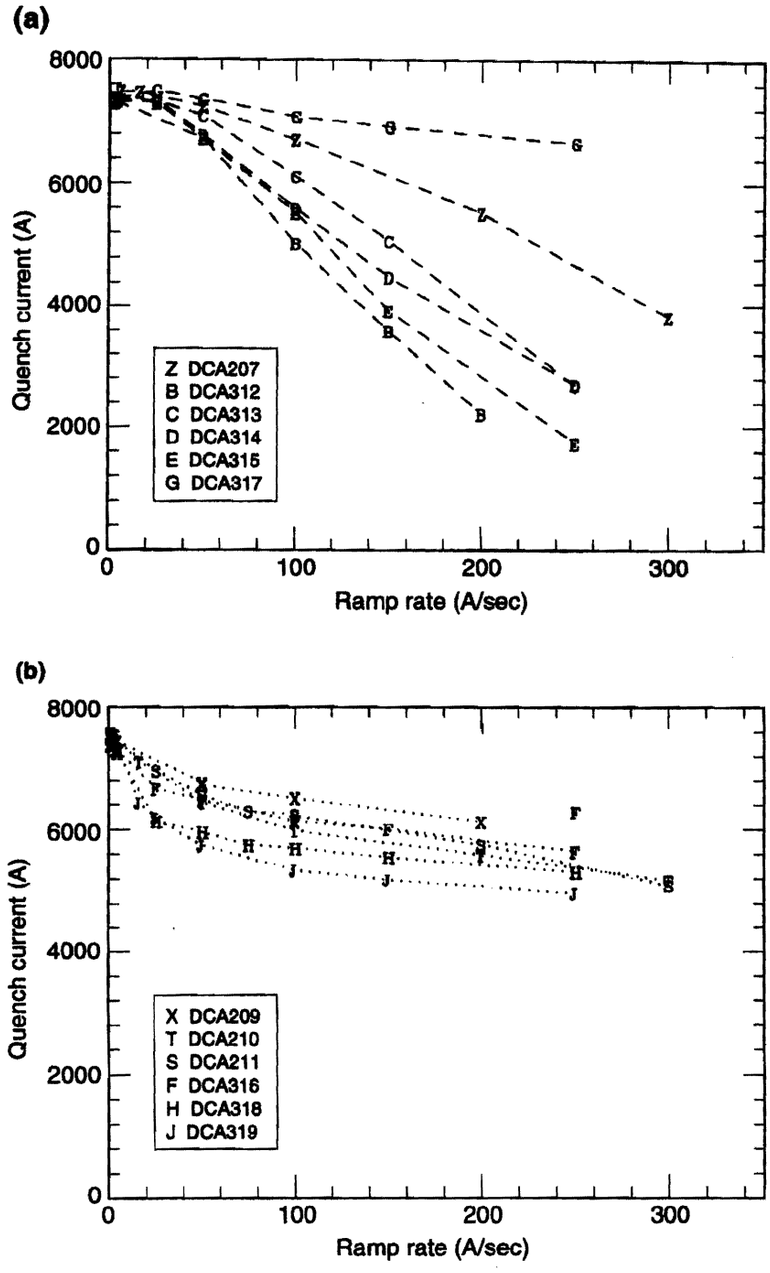


Figure 19. Ramp rate sensitivity of selected 5-cm-aperture, 15-m-long SSC dipole magnet prototypes: (a) Type A and (b) Type B. (The magnets are grouped according to the manufacturer and the production batch of their inner cable strands).

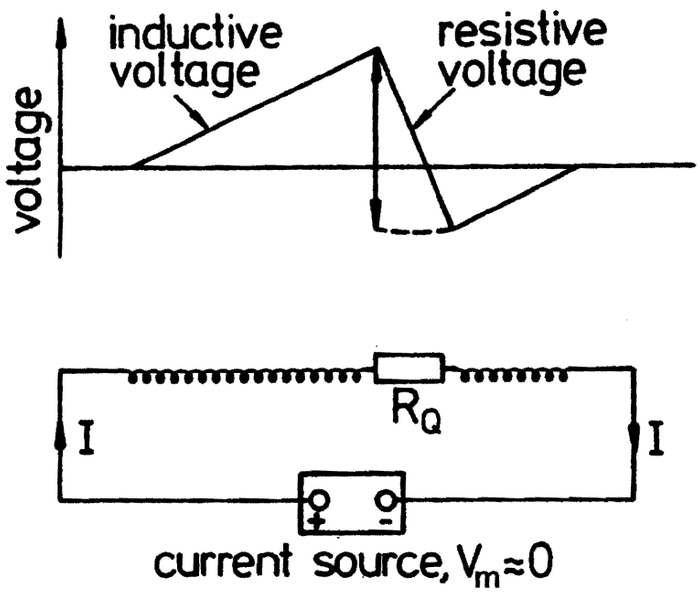


Figure 20. Voltage distribution in a quenching magnet. The total voltage across the magnet is assumed to be nil and the developing resistance is assumed to be concentrated at about two third of the magnet length [4].

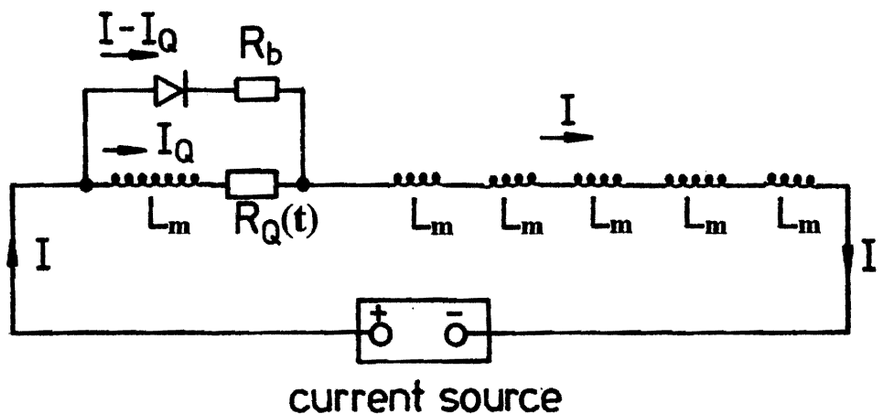


Figure 21. Electrical circuit of a quenching magnet in a magnet string [4].